Titas Gertus

Yb:KGW femtosecond laser material micromachining system and applications

DOCTORAL DISSERTATION

Technology Science for Material Engineering (08T)

Laser Technology (T165)

VILNIUS 2012

Titas Gertus | Yb:KGW femtosecond laser material micromachining system and applications

VILNIUS UNIVERSITY

CENTER FOR PHYSICAL SCIENCES AND TECHNOLOGY

PHYSICS INSTITUTE

Titas Gertus

Yb:KGW FEMTOSECOND LASER MATERIAL MICROMACHINING SYSTEM AND APPLICATIONS

Doctoral dissertation

Technology Science for Material Engineering (08T)

Laser Technology (T165)

Vilnius, 2012

The research described in this thesis was performed in 2009 – 2012 in Vilnius University, Physics faculty, Department of Quantum Electronics, Laser Research Center (Sauletekio Ave. 10, Vilnius, Lithuania) and in *Workshop of Photonics* laboratory (Altechna Co. Ltd., Konsitucijos Ave. 23B, Vilnius, Lithuania).

Scientific supervisor

Prof. Habil. Dr. **Valerijus Smilgevičius** (Vilnius University, Technology Science for Material Engineering – 08T, Laser Technology – T165)

VILNIAUS UNIVERSITETAS

FIZINIŲ IR TECHNOLOGIJOS MOKSLŲ CENTRO

FIZIKOS INSTITUTAS

Titas Gertus

Yb:KGV FEMTOSEKUNDINĖ LAZERINĖ SISTEMA MEDŽIAGŲ MIKROAPDIRBIMUI IR JOS TAIKYMAI

Daktaro disertacija

Technologijos mokslų srities, medžiagų inžinerijos kryptis (08T)

Lazerinė technologija (T165)

Vilnius, 2012

Disertacija rengta 2009 – 2012 m. Vilniaus Universiteto, Fizikos fakulteto, Kvantinės elektronikos katedros, Lazerinių tyrimų centre (Saulėtekio g. 10, Vilnius, Lietuva) ir *Workshop of Photonics* laboratorijoje (UAB „Altechna“, Konstitucijos pr. 23B,Vilnius, Lietuva).

Mokslinis vadovas

Prof. habil. dr. **Valerijus Smilgevičius** (Vilniaus universitetas, technologijos mokslai, medžiagų inžinerija – 08T, lazerinė technologija – T165)

"*The great pleasure in life is doing what people say you cannot do.*."

Walter Bagehot

Table of Contents

Preface

I am involved in femtosecond laser micromachining (FLM) since my Bachelor thesis. It was called “Dimensional microfabrication with femtosecond laser scanner”. Back in 2005 it looked to be a really challenging and, at the same time, very promising topic. New opportunities and fields of applications were rapidly emerging. And in 2012, it is really becoming an enabling technology for various scientific and industrial applications. I was lucky to assist in developing a prototype femtosecond laser micromachining system for a Japanese customer (back in 2006) and I’m thankful to Altechna Ltd. for giving me this opportunity.

My Master thesis topic: “Diffractive optical elements fabrication using femtosecond pulses”. It was concentrated on the interaction of a single femtosecond light pulse with surface and volume of dielectric materials aimed to fabricate various diffractive optical elements (DOE). Fabrication of elements, such as 1D and 2D diffractive gratings, diffractive gratings with a bifurcation for optical vortex generation, computer generated holograms, was demonstrated.

In this thesis I put all my knowledge in femtosecond laser micromachining systems and applications, which I gained during my bachelor, master and graduate studies. In consequence, the main prefixes which will be commonly used in this thesis are **femto**- and **micro-.** Femto- (f) is a prefix of the metric system denoting 10^{-15}. It is derived from the Danish word “femten”, meaning "fifteen". $\tau = 1$ fs is trillion times shorter than a human eye blink[1]. Micro (μ) is a prefix in SI metric system denoting a factor of 10^{-6} (one millionth). Micro- prefix comes from the Greek μικρός (mikrós), meaning "small". 1 μm is 2000 times smaller than needle’s eye.

Ten years at Vilnius University have passed too quickly..

[1] The average duration of a human eye blink is 100-400 milliseconds.

Abstract

This thesis is focused on femtosecond laser material (FLM) processing. FLM is a key enabling technology for various micro-fabrication tasks. An ytterbium doped potassium–gadolinium (Yb:KGW) high repetition rate femtosecond laser source based micromachining system (femtoLAB) was developed and applied for various FLM applications. We demonstrate the fabrication of various unique functional microstructures (computer generated holograms, surface acoustic wave transducers, phononic and photonic crystal devices, radial and azimuth polarization converter) with less than 1 μm accuracy. Functional structures were fabricated by selectively removing thin (200 – 300 nm) metallic layers from dielectric substrates surface or by modifying the bulk of transparent high bandgap materials. The parameters of the fabricated functional structures were measured and their performance was characterized.

Acknowledgments

I am greatly thankful to Vilnius University Laser Research Center staff, especially to my supervisor Prof. Habil. Dr. Valerijus Smilgevičius, for supporting me during my PhD studies. I am also thankful to coauthors of publications:

Prof. Dr. R. Gadonas, Dr. M. Malinauskas, M. Rutkauskas, Dr. M. Peckus (Laser Research Center, Department of Quantum Electronics, Physics Faculty, Vilnius University, Lithuania).

Prof. Dr. K. Staliūnas, L. Maigytė (Departament de Física i Enginyeria, Universitat Politècnica de Catalunya, Spain).

Prof. Dr. S. Juodkazis (Swinburne University of Technology, Hawthorn, Australia).

Prof. Dr. P. Kazansky, M. Beresna, M. Gecevičius (Optoelectronics Research Centre, University of Southampton, United Kingdom).

Prof. Dr. D. Čiplys, Dr. P. Každailis, Dr. R. Rimeika (Department of Radiophysics, Physics Faculty, Vilnius University, Lithuania).

Dr. G. Račiukaitis, E. Stankevičius (Center for Physical Sciences and Technology, Vilnius University, Lithuania).

Finally, I want to thank Altechna staff, especially Dr. G. Šlekys and M. Mikutis.

Introduction

More than 50 years have already passed since the first ruby laser was built by Theodore H. Maiman at Hughes research laboratories (California, United States) [1]. Nowadays, lasers are widely used in different scientific, industrial, military or medical applications [2]. Of course, lasers used in different applications differ. The most advanced type, solid state lasers generating ultra–short light pulses are mostly used in scientific applications such as Raman spectroscopy, laser induced breakdown spectroscopy (LIBS), atmospheric remote sensing, atom trapping, confocal laser scanning microscopy, two–photon excitation microscopy, material processing and many other. In this thesis, **femtosecond laser micromachining (FLM)** is the main topic.

What is FLM? FLM is a process during which material is ablated or its properties are modified in a predefined manner using femtosecond laser radiation. Focused femtosecond pulses can easily reach intensities of $I = 10^{15}\ \mathrm{W/cm^2}$. Such high intensity is more than enough for local ionization of any solid material, be it metal, polymer or glass. At such illumination intensities, even optically transparent wide bandgap dielectric materials, such as calcium fluoride (CaF_2), sapphire or quartz, get opaque for the incident radiation. Essentially, the absorption process becomes independent of the material [3]. Tightly focused femtosecond pulses can induce permanent localized material structure changes. Spatial confinement combined with laser-beam scanning or sample translation, makes it possible to fabricate geometrically complex structures in three dimensions. Femtosecond laser micromachining was first demonstrated in 1994 by G. Mourou et al. They demonstrated ablation of micrometer sized features on silica and silver surfaces [4]. In less than ten years, nanometer resolution of FLM was demonstrated [5]. A key advantage of using femtosecond pulses, as opposed to longer pulses, for direct writing is that they can rapidly and precisely transfer energy in materials [6].

Titanium–doped sapphire (Ti:Sapphire) is the most common gain medium for femtosecond solid state lasers. It generates light pulses with $\lambda = 800$ nm center wavelength, $\tau = 5$ fs [7] pulse duration, $E_{\mathrm{P}} = 5$ mJ energy light pulses at a repetition rate of $f = 1$ kHz [8]. But high throughput micromachining applications require higher repetition rate. Alternatively, ytterbium doped potassium-gadolinium tungstate (Yb:KGW) femtosecond solid state lasers can generate $\lambda = 1030$ nm wavelength, $\tau < 200$ fs pulse duration, $f = 200$ kHz repetition rate and up to $P = 15$ W average power radiation and pulse energy of $E_{\mathrm{P}} = 0{,}2$ mJ. In this thesis, Yb:KGW femtosecond laser PHAROS produced by the Lithuanian company *Šviesos konversija* (known as *Light Conversion* on international market) was used.

Thesis objectives

- To develop a femtosecond micromachining system capable of performing femtosecond fabrication tasks on various solid materials surface and transparent materials bulk.
- Perform research of selective removal of thin metal films from dielectric substrates. Fabricate various functional structures: holograms, interdigital transducers and phononic crystals.
- Perform research of femtosecond pulse interaction with the bulk of dielectric transparent materials. Fabricate functional devices: polarization converters and photonic crystal for spatial light filtering.

Innovation and relevance

Femtosecond micromachining is an emerging technology[2]. It's a key technology for various micro-fabrication tasks. The unique femtoLAB femtosecond micromachining system, implementing Yb:KGW femtosecond laser PHAROS, second, third and fourth harmonic generator HIRO, polarization rotators, beam scanning and shaping, sample positioning and recognition, was developed. System control algorithms enabling the fabrication of unique functional structures (holograms, interdigital transducers, phononic crystals, photonic crystals and micro-tubes) were composed.

For the first time, three-dimensional photonic crystals, which were used to demonstrate the effect of spatial filtering of light beams, were fabricated by FLM. Also, other unique functional structures such as surface acoustic wave transducers, phononic crystals were fabricated. For the first time, a femtosecond vortex beam was showed to be able to modify the bulk of transparent materials and to form micro-tubes structures in photosensitive polymer.

Together with the group of Prof. P. Kazansky from the Southampton University the unique S-waveplate radial and azimuthal polarization converter based on self-assembled nanogratings induced in quartz glass bulk was developed, fabricated and introduced in to the market.

[2] Emerging technologies are contemporary advances and innovation in various fields of technology.

Prepositions to defend

1. Unique femtosecond micromachining system and fabrication algorithms were developed that enable precise performance of various micro-fabrication tasks.
2. Selective ablation of thin metallic films from the transparent substrates using femtosecond light pulses enables fabrication of binary holograms, interdigital transducers and phononic crystals for acoustic wave filtering.
3. Transparent dielectric materials refractive index permanent modulation using femtosecond light pulses enables the fabrication of photonic crystals suitable for spatial light filtering.
4. Self-assembled nanogratings induced inside the bulk of transparent materials using femtosecond light pulses enables the fabrication of radial and azimuthal polarization converter.
5. Femtosecond optical vortex beams enable fabrication of micro-tube hollow structures using multi-photon polymerization technique.

Approbation

The results of research described in this thesis are published in 6 publications in scientific journals, 5 of which are included in ISI journal list included. These results were presented at 14 conferences (listed below), 8 of which were personally presented by the author.

Publications

[P1] L. Maigytė, **T. Gertus**, M. Peckus, J. Trull, C. Cojocaru, V. Sirutkaitis and K. Staliunas "Signatures of light beam spatial filtering in three-dimensional photonic crystal", Phys. Rev. A **82**, 043819 (2010).

[P2] T. Gertus, P. Každailis, R. Rimeika, D. Čiplys, V. Smilgevičius, "Surface acoustic wave transducers fabricated by femtosecond laser ablation", Electron. Lett. **46** (17), 1175–1176 (2010).

[P3] M. Beresna, M. Gecevičius, P. G. Kazansky, **T. Gertus**, "Radially polarized optical vortex converter created by femtosecond laser nanostructuring of glass", Appl. Phys. Let. **98** (20), 201101–201103 (2011).

[P4] T. Gertus, M. Mikutis, V. Smilgevičius, **"**Dielectric materials volume and surface processing using femtosecond vortex beam**",** LiM2011, Phys. Proc. **12** (2), 94–98 (2011).

[P5] T. Gertus, M. Mikutis, P. Každailis, R. Rimeika, D. Čiplys, and V. Smilgevičius, "Surface-acoustic-wave phononic crystal device fabricated by femtosecond laser ablation**"**, Microw. Opt. Tech. Lett., **54** (5), 1286–1287 (2012).

[P6] E. Stankevičius, **T. Gertus**, M. Rutkauskas, G. Račiukaitis, R. Gadonas, V. Smilgevičius and M. Malinauskas, "Fabrication of micro-tubes array in photopolymer SZ2080 by using three different methods of multi-photon polymerization technique**",** J. Micromech. Microeng. **22**, 065022 (2012).

Author contributions

The author contributed in writing the text of all above mentioned publications and the fabrication of experimental structures described therein. In [P1] author fabricated three-dimensional photonic crystals which were used to demonstrate light beam spatial filtering. Fabrication of surface acoustic wave transducers [P2] and surface acoustic wave phononic crystal devices [P5] as well as micro-tubes using femtosecond vortex beam [P6] was carried by the author. Author also contributed to the writing fabrication algorithms which enabled fabrication of polarization converter described in [P3]. Author carried all the research described in [P4]. Different measurements on the fabricated functional structures and the characterization of their performance were done by the coauthors.

Other publications:

1. M. Beresna, **T. Gertus**, R. Tomašiūnas, H. Misawa and S. Juodkazis, "Three-dimensional modeling of the heat-affected zone in laser machining applications", Laser Chem., 976205 (2008).

2. K. Juodkazis, J. Juodkazytė, P. Kalinauskas, **T. Gertus**, E. Jelmakas, H. Misawa and S. Juodkazis, "Influence of laser microfabrication on silicon electrochemical behavior in HF solution", J. Solid State Electr. **14** (5), 797–802, (2008).

3. M. Malinauskas, V. Purlys, A. Žukauskas, G. Bičkauskaitė, **T. Gertus**, P. Danilevičius, D. Paipulas, M. Rutkauskas, H. Gilbergs, D. Baltriukienė, L. Bukelskis, R. Širmenis, V. Bukelskienė, R. Gadonas, V. Sirvydis,

A. Piskarskas, “Laser two-photon polymerization micro- and nanostructuring over a large area on various substrates”, Proc. Spie, **7715**, 77151F (2010).

4. M. Malinauskas, P. Danilevičius, A. Žukauskas, G. Bickauskaitė, V. Purlys, M. Rutkauskas, **T. Gertus**, D. Paipulas, J. Matukaitė and D. Baltriukienė, “Laser 3D micro/ nanofabrication of polymers for tissue engineering applications”, Latvian J. Phys. Tech. Sci., **48** (2), 32–43 (2011).

Conferences

1. **T. Gertus**, P. Každailis, R. Rimeika, D. Čiplys, V. Smilgevičius, “**Paviršinių akustinių bangų keitiklio gamyba lazerinio plazminio garinimo būdu”**, LNFK38, Vilnius, Lithuania, 2009.

2. **T.Gertus,** G. Šlekys, “**Femtosecond micromachining Activities and Applications**”, LON2009, Vilnius, Lithuania, 2009.

3. **T. Gertus**, R. Razgaitis, “**Laser-induced backside wet etching using femtosecond laser pulses**”, Open Readings, Vilnius, Lithuania, 2010.

4. L. Maigyte, **T. Gertus**, M. Peckus, V. **S**irutkaitis and K. Staliūnas “**Experimental evidences of light beam filtering by three-dimensional photonic crystal”,** ICTON, Munich, Germany, 2010.

5. L. Maigytė**, T. Gertus**, M. Peckus, J. Trull, C. Cojocaru, V. Sirutkaitis and K.Staliūnas, **“Signatures of Light Beam Spatial Filtering in Three**

Dimensional Photonic Crystal", Alexander von Humboldt Forum, Vilnius, Lithuania, 2010.

6. M. Malinauskas, A. Žukauskas, G. Bičkauskaitė, M. Rutkauskas, K. Belazaras, H. Gilbergs, P. Danilevičius, V. Purlys, D. Paipulas, **T. Gertus**, R. Gadonas, A. Piskarskas, D. Baltriukienė, V. Bukelskienė and A. Gaidukevičiūtė, **"Fabrication of Three-Dimensional Nanostructures by Laser Polymerization Technique"**, Proc. CYSENI, Kaunas, Lithuania, 2010.

7. P. Stanislovaitis, **T. Gertus**, V. Smilgevičius, "**Control of Optical Vortex Dislocations Using Optical Methods"**, Open Readings, Vilnius, Lithuania, 2011.

8. **T.Gertus**, M. Mikutis, V. Smilgevičius, "**Dielectric materials volume and surface processing using femtosecond vortex beam"**, LiM2011, Munich, Germany, 2011.

9. L. Maigyte, J. Trull, V. Mizeikis, M. Malinauskas, S. Juodkazis, C. Cojocaru, M. Rutkauskas, M. Peckus, V. Sirutkaitis, **T. Gertus**, K. Staliunas, "**Collimated beams by woodpile photonic crystals"**, CLEO, Munich, Germany, 2011.

10. **T. Gertus**, M. Mikutis, P. Každailis, R. Rimeika, D. Čiplys, V. Smilgevičius, "**Phononic crystal for surface acoustic wave filtering fabrication using femtosecond laser ablation",** LNFK39, Vilnius, Lithuania, 2011.

11. **T. Gertus**, M. Rutkauskas, M. Malinauskas, R. Gadonas, V. Smilgevičius, "**Micro tube fabrication using optical vortex beam with laser polymerization technique"**, LNFK39, Vilnius, Lithuania, 2011.

12. T. Jankauskas, **T. Gertus**, V. Smilgevičius, M. Beresna, M. Gecevičius, "**Radial polarization beams in femtosecond micromachining"**, LNFK39, Vilnius, Lithuania, 2011.

13. T. Jankauskas, **T. Gertus**, M. Beresna, M. Gecevičius**, "Comparison of radial, azimuthal, linear and circular polarization in laser micromachining under normal focusing conditions",** Open Readings, Vilnius, Lithuania, 2012.

14. **T. Gertus**, „**Radial/azimuth polarization converter manufacturing using femtosecond laser system**", Forum Lasers in Action, LASYS 2012, Stuttgart, Germany, 2012.

List of Acronyms

1D – one dimensional

2D – two dimensional

3D – three dimensional (usually XYZ)

AF – autofocus

AFM – atomic force microscopy

CCD – charge-coupled device

CPA – chirped pulse amplification

COG – chromium on glass

CV – cylindrical vector

CGH – computer generated hologram

DOE – diffractive optical elements

DLW – direct laser writing

DT – damage threshold

HAZ – heat affected zones

HEX – hexagonal

HL – holographic

IR – infrared

IDT – interdigital transducers

FLM – femtosecond laser micromachining

E_g – bandgap

fs – femtosecond (10^{-15} s)

LA – laser ablation

MPP – multi-photon polymerization

MEMS – micro electromechanical system

MPI – multi photon ionization

MV – machine vision

NA – numerical aperture

OV – optical vortex

PC – photonic or phononic crystal

P_{D} – pulse density (pulses/mm)

P_{dis} – pulse distance (μm)

SAW – surface acoustic wave

SE – selective ablation

μm – micrometer (10^{-6} m)

$2w_0$ – beam waist diameter at focus

z_{R} – Rayleigh length

λ – light wavelength

ν – light frequency

τ – light pulse duration

Yb: KGW – ytterbium doped potassium gadolinium tungstate

UV – ultraviolet

1. Femtosecond laser material processing: background

1.1. Advantages of femtosecond laser micromachining

Femtosecond laser micromachining (FLM) has many advantages compared to other fabrication techniques. FLM is a direct, contactless, non-thermal, highly flexible, and localized material processing technology.

Direct. Direct writing means that fabrication is a single step process not requiring additional pre- or post- treatment. Examples are direct photomask fabrication [9], waveguides fabrication [10] etc.

Contactless. In FLM, there is no direct contact between the tool and the sample. Due to nonlinear processes it also enables processing the bulk of transparent solid materials [11].

Non-thermal. Short (hundreds of femtoseconds) pulse equals short matter – light interaction time. Energy transfer time is short, compared to the electron-phonon relaxation time. This ensures minimal heat affected zone (HAZ) during processing.

Highly flexible. FLM fabrication parameters are easily adjustable; the parameters include pulse density, pulse energy, focusing conditions and etc. The scanning trajectory is not limited to 2D. Tightly focused laser radiation has very high energy density ($\phi \geq 7\ \mathrm{kJ/cm^2}$) at the focus spot. At such intensities, even wide bandgap transparent materials start absorbing light through nonlinear absorption. Therefore, any solid material can be fabricated using FLM.

Localized. Laser radiation can be focused to a waist $\approx \lambda$. Moreover, material modifications can occur even in the smaller region than waist diameter – it is possible to ablate sub diffraction-limited targeted regions [12,13]. Short matter – light interaction time means optical excitation ends before the surrounding lattice is perturbed, what results in highly localized modification without collateral material damage [14].

1.2. Femtosecond laser micromachining applications

Femtosecond laser micromachining (FLM) applications can be used in many real-world applications in various fields. High aspect ratio micro-hole drilling (diameter from several microns to several millimeters) applicable to fuel injection or ink jet printer nozzles, detectors, pin holes for spatial light filtering, micro-electronics, microfluidics and etc. Figure 1 a) shows electron microscope image of $d = 2$ μm diameter micro-hole drilling performed using percussion technique in thin aluminum foil. Figure 1 b) shows an optical microscope image of micro-holes (diameter from 10 μm to 20 μm) drilled through optical fiber using water assisted helical drilling. Micro-structures in an optical fiber created by femtosecond laser micromachining can function as the sensing elements [15].

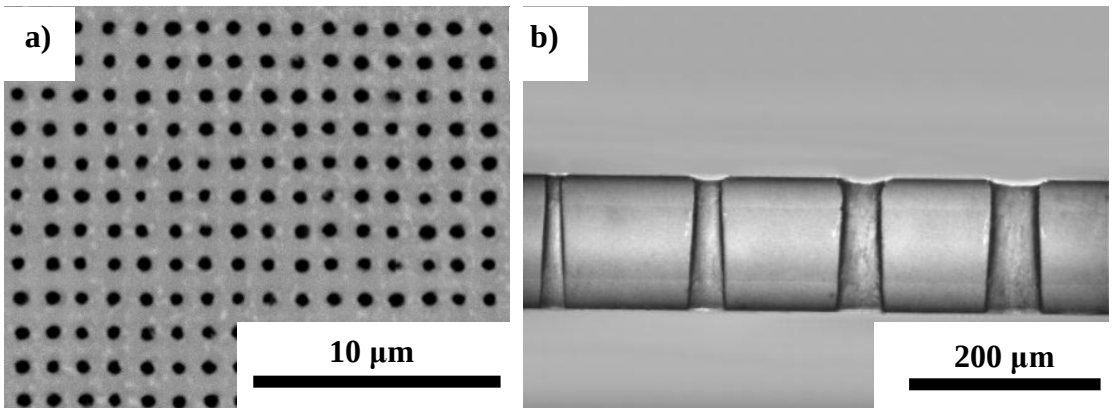

Figure 1 a) electron microscope photo of 2 μm diameter holes array drilling performed using FLM in thin aluminum foil. b) Holes (from 10 μm to 20 μm diameter) drilled through optical fiber using water assisted helical drilling. Courtesy of Altechna (Lithuania)

The ability to pattern various material surfaces enables the modification of surface properties such as reflectivity, resistance to liquids, color, roughness, absorption or other. For example, FLM allows black silicon fabrication [16], which enables new functionalities in microsystems [17]. Ripples (with $\sim$190 nm period) formation on large surface area of SiC substrate enables the fabrication of surface-enhanced Raman scattering (SERS) sensors [18].

Selective ablation (SE) enables removing thin metallic or dielectric layers without damaging the substrate itself. In crystalline silicon (cSi) photovoltaic manufacturing it can be used to selective remove dielectric silicon nitride or silicon dioxide passivation layers. SE also enables laser cleaning - removal of surface contaminants without damaging the substrate (Figure 2). SE can be used for photomask repairing to remove faulty or unnecessary metal path [19] or even fabricate a complete photomask in a single step [92]. SE of conducting indium tin oxide (ITO) layer [20] enables fabricating various transparent electronic components such as mobile phone touch screens.

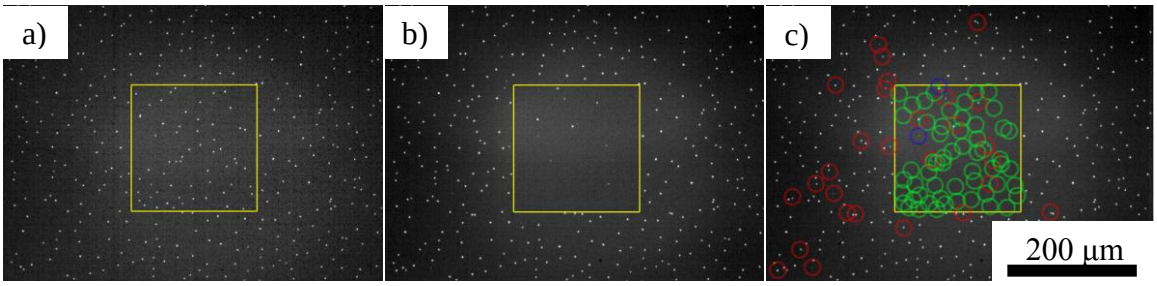

Figure 2 a) optical microscope dark field photo of fused silica substrate contaminated with micrometer size particles. b) Surface photo after scanning with femtosecond pulses (λ = 1030 nm), c) removed particle analysis: green circles indicate particles removed from scanned area, blue - particles that were not removed, red – particles that have appeared after the scanning. Scanned area size (shown in yellow square) is 200 µm x 200 µm

Laser ablation (LA) allows fabrication of 2D micro electro-mechanical systems (MEMS) [21]. LA enables nickel titanium (also known as nitinol) [22] cardiovascular stent manufacturing. Figure 3 shows an optical microscope photo of a cardiovascular implant stent fabricated from nitinol (courtesy of Raydiance Inc., USA [23]).

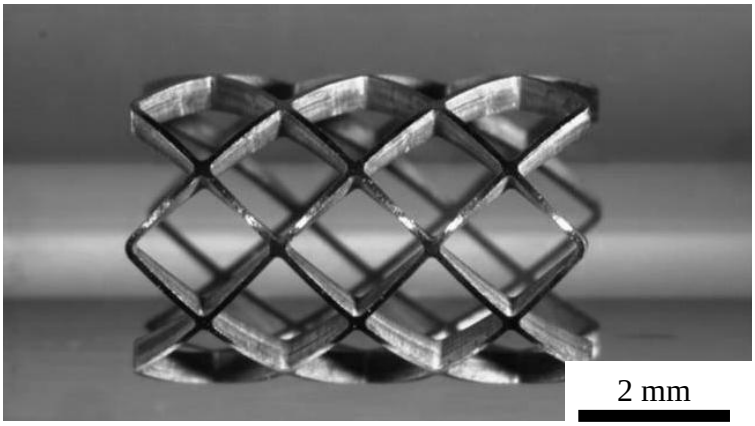

Figure 3 Cardiovascular stent implant cut from nitinol (wall thickness 460 μm). Courtesy of Raydiance Inc., USA [23]

The ability to modify the bulk of transparent dielectric materials allows fabricating various photonic devices: straight and curved waveguides [24,25,26], splitters [27], directional couplers [28], Bragg gratings inside optical fibers [29, 30], waveguide amplifiers [31], micro-resonators [32]. It also enables the fabrication of five-dimensional (5D) optical data storage media [33] and photonic band gap structures [34].

Laser direct writing (multi-photon photopolymerization) allows to fabricate complex 3D transparent structures such as optical biochips [35], lab-on-chip [36] or even micro-electro-optical-mechanical systems (MEOMS) [37]. Integrated micro-optics (micro-lenses, micro-prisms, micro-phase plates, photonics crystals and other) can also be fabricated [38]. The fabrication of high aspect ratio micro-fluidic channels and tunnels [39] fabrication allows 3D microfluidic devices fabrication [40].

Biomedical applications are the most important field where FLM is used. For example, eye surgery called laser-assisted in situ keratomileusis (LASIK) operations can be performed using a single femtosecond laser using fundamental and high harmonic wavelength [41]. Moreover, scaffolds for cells growing can be fabricated from biocompatible and biodegradable polymers [42]. Bio-photonic chips [43] and micro-mechanical valves for glaucoma implants [44] can be fabricated.

1.3. Interaction of femtosecond laser pulses with matter: the basics

Light interaction with material can be described using Maxwell's equations [45]. To understand the basics we only need the equation for the electric field (similar ones can be written for the magnetic field) equation that describes the nonlinear polarization response of matter to the incident electric field induced:

$$\boldsymbol{P = \epsilon_0 \chi^{(1)} \cdot E + \epsilon_0 \chi^{(2)} \cdot EE + \epsilon_0 \chi^{3} \cdot EEE} + .. \quad \textbf{(1)}$$

here $\varepsilon_0 = 8{,}853 \cdot 10^{-12}\mathrm{A \cdot s/V}$ is the vacuum permeability. $\chi^{(n)}$ $n > 1$ order dielectric susceptibility tensors describe nonlinear perturbation occurring when the incident electromagnetic field is higher than the electric field ($10^9\ \mathrm{V/m}$) that binds valence electrons in atoms [3]. When the intensity of incident electromagnetic field is high ($I_{\mathrm{peak}} < 10^{13}\ \mathrm{W/cm^2}$) and $\chi^{(2)}$ is a scalar, nonlinear processes can occur: second harmonics generation, sum and difference frequency mixing, two photon absorption, four-wave mixing and nonlinear refractive index induction.

In dielectric materials, *nonlinear excitation* takes place when the incident electromagnetic field intensity reaches $I_{\mathrm{peak}} \approx 10^{13}\ \mathrm{W/cm^2}$. It then becomes high enough to promote electrons from the valence band to the conduction band [46]. Multiple photons must be absorbed simultaneously in order to satisfy $mh\nu > E_g$, here E_g is a bandgap. *Multi-photon ionization* (Figure 4 a) is the dominant mechanism at "low" laser intensities and high frequencies. At high laser intensity and low frequency, *nonlinear excitation* proceeds via tunneling process, as shown in Figure 4 b. The strong field distorts the band structure and reduces the potential barrier between the valence and conduction bands. Direct band to band transitions may then proceed by quantum tunneling of the electron from the valence to conduction band [47].

The transition between the processes is described by the Keldysh parameter [48]:

$$\gamma = \frac{\omega}{e}\sqrt{\frac{m_e c n \epsilon_0 E_g}{I}} \tag{2}$$

here ω is the laser frequency, I is the laser intensity at the focus, m_e is the effective electron mass, e is the fundamental electron charge, c is the speed of light, n is the linear refractive index and ϵ_0 is the permittivity of free space, E_g is the bandgap energy. If $\gamma < 1{,}5$, then tunneling (multiphoton) ionization dominates. For $\gamma \approx 1{,}5$, photoionization is a combination of tunneling and multi-photon ionization. For example, waveguide fabrication in transparent dielectrics results in $\gamma \approx 1$, so that nonlinear ionization is a combination of both processes [49].

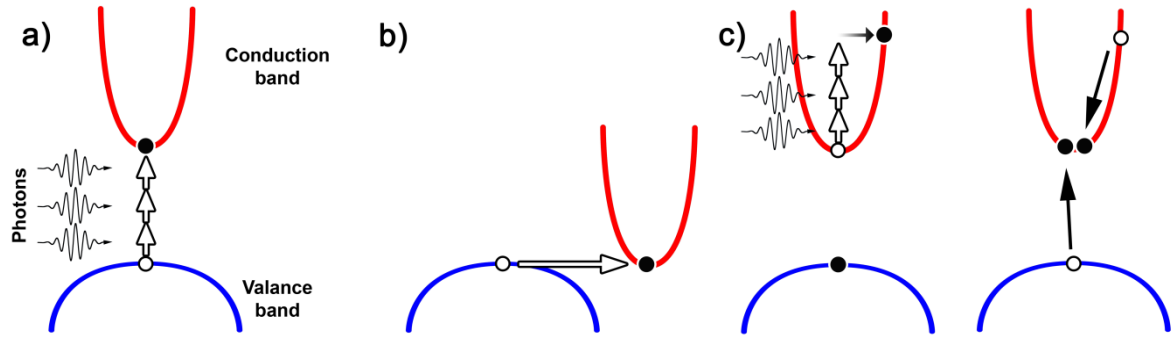

Figure 4 Nonlinear excitation processes underlying femtosecond laser machining: a) multi-photon ionization, b) tunneling ionization and c) avalanche ionization – free carrier absorption followed by impact ionization [50].

Electrons in the conduction band may also absorb laser light by free carrier absorption (Figure 4 c). After sequential linear absorption of several photons, a conduction band electron's energy may exceed the conduction band minimum by more than the band gap energy and the hot electron can then impact ionize a bound electron in the valence band, resulting in two excited electrons at the

conduction band minimum. These two electrons can undergo free carrier absorption and further impact ionization, and the process can repeat itself as long as the laser field is present and strong enough, giving rise to an electron avalanche. Avalanche ionization requires that sufficient seed electrons are initially present in the conduction band. These seed electrons may be provided by thermally excited impurity or defect states, or direct multiphoton or tunneling ionization [47]. The contribution of avalanche ionization is greater at longer pulse durations and is important for materials with greater band gap energies such as fused silica and sapphire [51].

In dielectric transparent materials self-focusing results from the intensity dependence of the refractive index described by the equation:

$$n = n_0 + n_2 I \tag{3}$$

here I is the laser intensity:

$$I = \frac{1}{2}\varepsilon_0 c n_0 |E|^2 \tag{4}$$

So the nonlinear refractive index n_2 is:

$$n_2 = \frac{3\chi^{(3)}}{4\varepsilon_0 c n_0^2} \tag{5}$$

This nonlinear refractive index gives rise to self-focusing, self-phase modulation, self-steepening, white light continuum generation and explains many of the features of the propagation of loosely-focused short laser pulses in transparent materials [52,67].

At radiation intensities $I_{\text{peak}} > 10^{13}\ \text{W/cm}^2$ virtually any material, whether metallic or dielectric, transparent or absorbing, can be fully locally ionized. After the ionization, the laser energy is absorbed by the free electrons due to inverse Bremsstrahlung and resonance absorption mechanisms and does not depend on the initial state of the target [53]. *Optical breakdown* occurs when the

critical density of free electrons is reached. In solids, electrons transfer energy to the lattice and permanent structural modifications occur [54]. If the incident radiation intensity is higher than optical breakdown threshold, the laser ablation process takes place. With femtosecond pulses, the optical breakdown due to multiphoton absorption within the ambient gas in front of the target enhances the thermal energy coupling to the substrate [55]. *Laser ablation* (LA) is the process of removing material from a solid (or occasionally liquid) surface by irradiating it with a laser beam [56]. The LA threshold is defined as the minimum laser energy density that can ablate the material. The LA threshold depends strongly on the duration of the incident pulse [57]. When femtosecond pulses are used, no vapor/plasma plume can develop during the pulse, and the ablation takes place only after the pulse [11]. Due to the shortness of time scales involved in the ablation by femtosecond laser pulses, the ablation process can be considered as a direct solid-vapor (or solid-plasma) transition [58].

1.4. Main laser machining parameters

The type of material modification (cold ablation, thermal evaporation, refractive index change, color change and etc.) that eventually takes place depends on many parameters of the FLM process: light pulse duration τ, wavelength λ, pulse repetition rate f, pulse energy E_{P}, pulse peak power P_{P}, fluence ϕ, intensity I, light polarization, pulse density P_D, pulse overlapping and focusing conditions.

Pulse duration τ (s) is the duration of light pulses emitted by laser source. Different modern techniques allow building lasers which can generate radiation from continuous wave (CW) to few-cycle (5 fs) optical pulses [7]. Pulse duration is usually expressed as its full width at half-maximum (FWHM) of the optical power versus time. Pulse duration determines the interaction time between the light and the matter, which is the key to material processing quality [58]. Moreover, the damage threshold of the material is greatly depend strongly on the incident pulse duration [59]. In advanced FLM systems, pulse duration change is an automated process. It is not always the case that the shorter the pulse the better the FLM result. As an example, see fabrication of the polarization converter described in chapter 3.6 (Figure 47).

Wavelength λ (nm) is a spatial period of the electromagnetic wave. Lasers with different lasing medium emit different wavelength radiation. For example carbon dioxide gas laser generates λ = 10,6 μm, neodymium doped YAG solid-state laser – λ = 1,064 μm, erbium doped YAG solid-state laser λ = 2,94 μm, InGaAsP semiconductor laser can generate from λ = 1 μm to λ = 2,1 μm wavelength. In order to shift the fundamental wavelength to the desired part of the spectrum – second, third, fourth or higher harmonics can be generated.

The wavelength of light determines the minimum spot size, to which light can be focused. It also determines the type of light–mater interaction that occurs.

Whether a certain wavelength is absorbed or not, depends on the properties of processed matter and/or incident light intensity. Photon energy is a function of wavelength:

$$E_{h\nu} = \frac{hc}{\lambda} \tag{6}$$

here $h = 6{,}626 \cdot 10^{-34}$ Js - Planck's constant, $c = 2{,}998 \cdot 10^{8}$ m/s – speed of light. For example, $\lambda = 1030$ nm wavelength photons have $E_{h\nu} = 1{,}2$ eV energy, which is less than the fused silica bandgap (3,5 eV). Therefore, at least three photons must be absorbed simultaneously through nonlinear absorption to excite fused silica sample. UV wavelength photons carry the highest energy.

Pulse repetition rate (f) is a frequency at which a laser generates light pulses or, simply, the number of emitted pulses per second. The repetition rates of currently available laser sources vary from $f = 1$ Hz to $f = 100$ MHz. Figure 5 shows a comparison of a) low repetition rate $f = 1$ kHz and b) high repetition rate $f = 25$ MHz laser energy deposition into focal volume. At low repetition rate, the time between pulses is $t = 1$ ms, the energy deposited by each laser pulse diffuses out of the focal volume before the next pulse arrives. At high repetition rate, with time between pulses $t = 40$ ns, the energy accumulates in the focal volume, making it possible to achieve very high temperatures around the focal volume with pulse energies of just a few nJ [46].

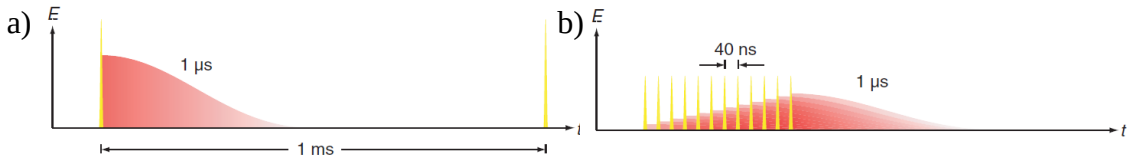

Figure 5 Comparison of laser energy deposition into focal volume using a) low repetition rate laser $f = 1$ kHz and b) high repetition $f = 25$ MHz [46]

Pulse energy E_{P} (J) is the total optical energy carried by the pulse. Typically, it varies from several nJ to several mJ. To calculate the pulse energy, we need to divide the average radiation power by the pulse repetition rate:

$$E_{\mathrm{P}} = \frac{P}{f} \tag{7}$$

here P – average power.

Peak power P_{P} (W) is a maximum optical power of a pulse. Peak power can be calculated using:

$$P_{\mathrm{P}} = 0{,}94 \cdot \frac{E_{\mathrm{P}}}{\tau} \tag{8}$$

here E_{P} – pulse energy, τ – pulse duration. For soliton pulses (with a sech^2 shape) the constant factor is 0,88 instead of 0,94. Peak power of a femtosecond pulse can be very high, for example with $\tau = 300$ fs, $E_{\mathrm{P}} = 150$ μJ the pulse peak power is $P_{\mathrm{P}} = 470$ MW, which is equal to the Fukushima Daiichi nuclear power plant block number 1 (Fukushima I – 1) power. The difference is that the power in light pulses is concentrated in very short periods of time (only $\tau = 300$ fs in this case).

Fluence Φ ($\mathrm{J/cm^2}$) or energy density is an areal density of radiant energy incident on a surface. It depends on the beam area. The smallest beam area (highest fluence) is achieved at the waist of the beam. For example, for $\lambda = 1030$ nm, $2w_0 = 4$ μm , $E_{\mathrm{P}} = 1$ μJ the fluence in waist is $\Phi_{\max} = 16\ \mathrm{J/cm^2}$.

Dependence of fluence ϕ and beam waist diameter $2w_0$ (black solid line) on the focal length f of the focusing lens is shown in Figure 6. Parameters in Figure 6: wavelength $\lambda = 1030$ nm, frequency $f = 200$ kHz, beam diameter before lens $2w = 6$ mm, beam quality $\mathrm{M^2} = 1{,}2$. Black dashed line indicates fused silica front surface damage threshold $\phi_{\mathrm{DT}} = 4\,\frac{\mathrm{J}}{\mathrm{cm^2}}$ ($\lambda = 800$ nm, $\tau = 300$ fs, $f = 1$ Hz [57]).

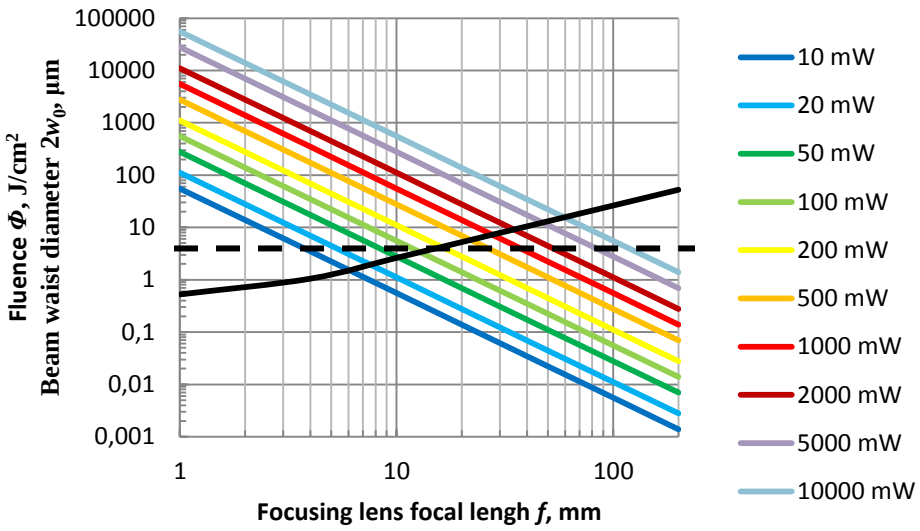

Figure 6 Fluence ϕ and beam waist diameter $2w_0$ dependence on focal length f of focusing lens. Wavelength $\lambda = 1030$ nm, frequency $f = 200$ kHz, beam diameter before lens $2w = 6$ mm, beam quality $M^2 = 1,2$

Peak Intensity I_P (W/cm^2) is the peak power P_P per unit area. For a beam with the peak power P_P and Gaussian beam radius w, the peak intensity (on the beam axis) is:

$$I_P = \frac{2P_P}{\pi w^2} \tag{9}$$

Polarization is a property of light describing the orientation of the electromagnetic field oscillations. When the oscillations of the electric field vector are in particular order, the light is said to be polarized. Laser radiation polarization can be linear, elliptical, circular, radial, azimuth or mixed. In most common FLM applications linear polarization is used. Linear polarization can be rotated using a λ/2 waveplate or converted into circular using a λ/4 waveplate. Radial or azimuth polarization can be achieved using conical Brewster prism [60], liquid crystal gel [61,62], photonic crystal segmented half-wave-plate [63] or in special type laser resonator configurations [64] such as an image-rotating resonator [65].

Polarization state is important for various aspects (quality, processing speed and other) of ultra-short pulse micromachining [66].

Pulse density (P_{D}) shows how many pulses per 1 mm is delivered to the sample. It depends on pulse repetition rate and the translation speed of the sample or the beam. Pulse density can be evaluated from:

$$P_{\mathrm{D}} = \frac{f}{v} \tag{10}$$

here f – pulse repetition rate (Hz), v - sample or beam translation speed (mm/s). The distance between pulses or pulse pitch (P_{dis}) can be evaluated from:

$$P_{\mathrm{dis}} = \frac{1}{P_{\mathrm{D}}} \tag{11}$$

The dependence of the pulse density (P_{D}) and pulse pitch (P_{dis}) on the laser repetition rate f and beam waist positioning speed v are shown in Figure 7.

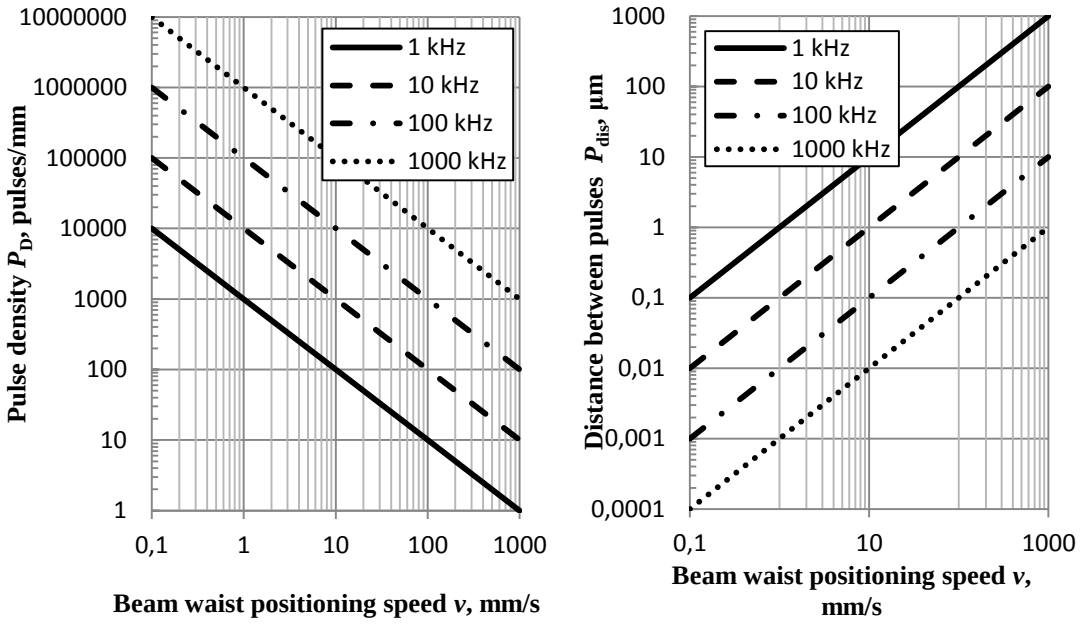

Figure 7 Pulse density (P_{D}) and pulse pitch (P_{dis}) dependence on laser repetition rate f and beam waist positioning speed

Beam waist ($2w_0$) or focus spot size depends on several laser beam parameters: wavelength, beam diameter, divergence, beam quality and focusing optics: lens focal length, numerical aperture. Focused beam size can be calculated using the formula:

$$2w_0 = \frac{2f\lambda}{\pi w} M^2 \tag{12}$$

here f is the focal length of the focusing lens, λ – wavelength, w – beam diameter at the lens entrance, M^2 – beam quality parameter. Linearly polarized laser beam can be focused into a spot size not smaller than diffraction limit. Diffraction limit was first described by Ernst Abbe in 1873. He discovered that light with the wavelength λ, traveling in a medium with refractive index n and converging to a spot with angle θ will make a spot with radius d:

$$d = \frac{\lambda}{2(n \cdot \sin\theta)} \tag{13}$$

The denominator $n \cdot \sin\theta$ is called the **numerical aperture** (NA). NA of objectives lenses can be $< 1{,}4$. Only oil immersion lenses have NA > 1. Hence the Abbe limit is roughly $d = \lambda/2$. Besides the numerical aperture, considering the focusing of a laser beam, we also have to take into account beam quality M^2. Laser beam quality M^2 is usually in the range from $M^2 = 1{,}2$ to $M^2 = 5$, which leads to a smallest beam waist size not less than λ. Numerical aperture (NA), or strength of the focusing is a critical parameter in controlling the interaction between short pulses and transparent materials [67].

Confocal parameter or depth of focus ($b = 2z_R$), here z_R is the Rayleigh length (distance along the propagation direction of a beam from the waist to the place where the area of the cross section is doubled [68]). Rayleigh length can be evaluated using the formula:

$$z_\mathrm{R} = \frac{\pi w_0^2}{\lambda} \tag{14}$$

Pulse overlap factor shows how much laser pulses overlap during laser machining. Consecutive pulses overlap if the pulse pitch is smaller than the diameter of the beam waist.

Hatch H is the distance between two parallel fabrication lines. Hatching lines overlap if H is less than fabricated line width l.

In order to build a FLM system and to perform FLM tasks all above mentioned parameters must be taken into account.

1.5. Femtosecond laser material processing techniques

Most common FLM techniques are: direct laser ablation (DLA), direct laser writing (DLW), laser induced back side wet etching (LIBWE), laser induced back side dry etching (LIBDE), laser-induced forward transfer (LIFT) and laser induced solid etching (LISE).

Direct laser ablation (DLA) is the most common technique in FLM (Figure 8 a). DLA is the process of removing material from a solid (or occasionally liquid) surface by irradiating it with a focused laser beam [69]. LA is a removal of material by laser plasma vaporization. Material ablation by irradiation of high intensity femtosecond laser pulses has been studied worldwide in various fundamental and applied researches [56]. A femtosecond laser can easily achieve high peak powers enough for full ionization of any material. This makes the femtosecond LA deterministic and reproducible. The ablation depth of the femtosecond laser is on the order of 0,01 ~ 1 mm per pulse [70] and selective thin (hundreds of nm) metal or dielectric layer removal is possible. DLA can be used to process the back side of a transparent substrate (Figure 8 b) as well.

Direct laser writing (DLW) is a 3D laser material processing technique which usually refers to nonlinear optical lithography or multi-photon polymerization (MPP). MPP technique allows fabricating 3D millimeter size structures with nanometer resolution. MPP is possible due to specific materials - photopolymers that are normally liquid or gel phase (positive photopolymers case) and become solid when exposed to appropriate light. In MPP, a small drop of photopolymer is placed on back side of glass coverslip (Figure 8 c). Two or more photons are needed to excite photo-initiator [71]. Due to nonlinearity of absorption, the photoresist is sufficiently exposed only within the focal volume. This tiny volume element is often referred to as the “voxel” in analogy to the pixel (picture element). By scanning this voxel with respect to the photoresist, essentially arbitrary three dimensional objects can be fabricated [72]. MPP allows

fabricating any 3D shape, including the shapes required for optical components: lenses, gratings, prisms or photonics crystals.

Fabrication of the bulk of transparent materials by FLM is also related to DLW, as it is a one-step direct laser material processing technique. It enables writing 3D waveguides [73], optical memory [74] or other functional devices in transparent solid materials bulk or surface.

Laser induced back side wet etching (LIBWE) is an indirect etching technique. Historically, LIBWE technique was developed for processing dielectric materials (such as fused silica or barium fluoride (BaF_2)) using nanosecond UV radiation [75]. LIBWE technique uses poisonous organic solvents such as pyrene and toluene, mercury, gallium as etching solution [76]. LIBWE using near infrared femtosecond pulses was recently demonstrated by R. Bohme et al. [77]. It was shown that femtosecond pulses enable water-assisted LIBWE [78]. Successful, water-assisted femtosecond laser backside etching of optical fibers was demonstrated by Ik-Bu Sohn at al. [79]. Drilling of straight and three-dimensional micro-channels in glass was shown by D. J. Hwang et al. [80]. The principle of LIBWE scheme is shown in Figure 8 d. The main idea is that the back side of sample is in touch with liquid absorbing laser radiation. LIBWE process can be described in three steps: a) strong absorption of intense UV light by an organic solution in contact with the UV transparent material, b) non-radiative decay of excited organic molecules creating a high temperature jump (> 2000 K) at the substrate-liquid interface, c) fast thermal evaporation of the solution, resulting in the generation of a shock wave and boiling of the solution. The expanding shock wave and the growth/collapse of the bubble generate a pressure jump, which removes the molten material from the surface [81].

Laser induced back side dry etching (LIBDE) technique is rather similar to LIBWE. LIBDE was developed by B. Hopp at al. [82]. Instead of the liquid etching solution LIBDE uses a solid thin film as an absorber (Figure 8 e). LIBDE relies on explosive boiling of the thin solid film to etch the transparent material.

Laser-induced forward transfer (LIFT) is a technique used to transfer small amounts of material from one surface to another on a pixel by pixel basis. LIFT process has been demonstrated for selective micro-deposition of metals, oxides, dielectrics and semiconductors [83,84]. In LIFT technique, donor layer is placed on back side of support substrate. Distance between donor layer and acceptor substrate L varies from 0 μm to 500 μm [83]. LIFT technique scheme is shown in Figure 8 f. Features as small as 300 nm can be deposited using LIFT technique [85]. Historically, LIFT was proposed as a quick and simple method of repairing damaged photomask. The potential to micro-deposit virtually any material that could be prepared in thin film form was quickly recognized. Unfortunately, an inherent limitation of the technique is that the material to be patterned is required to act as its own propellant, for transfer, which in practice limits the range materials that can be transferred. Multi-photon absorption is the key advantage for femtosecond pulses LIFT of transparent donors. In addition, femtosecond studies have already reported smaller feature sizes than those in the nanosecond regime [86]; transfer of intact biomaterial has been demonstrated [87], as well as transfer in solid phase [88], and a reduction in the spreading out of material [89].

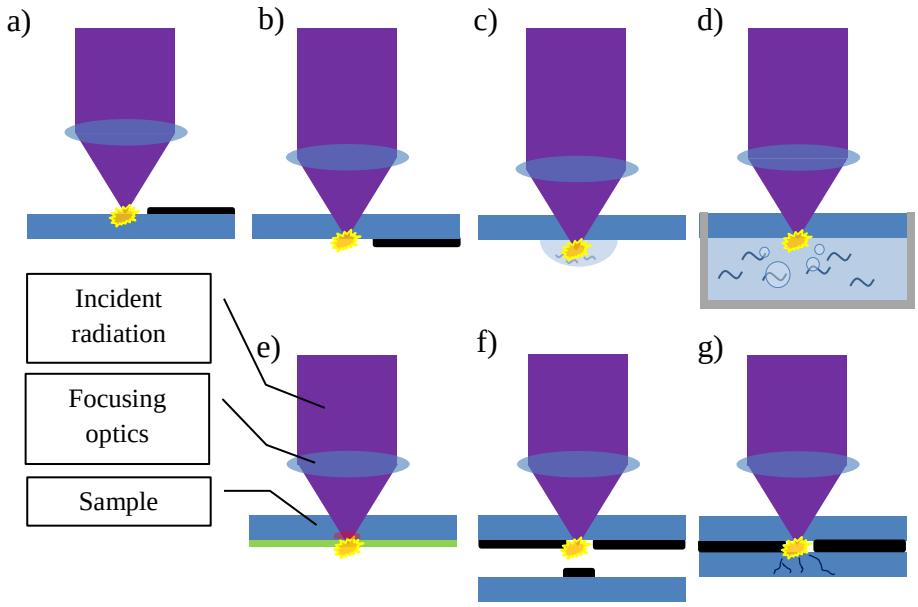

Figure 8 a) DLA, b) DLA back surface of transparent substrate, c) MPP, d) LIBWE, e) LIBDE, f) LIFT and g) LISE techniques principal schemes

Laser induced solid etching (LISE) is a case of the LIFT technique, where the distance between donor layer and acceptor substrate is equal $L = 0$. Thus, the LISE techniques result is different from LIFT. LISE results in a micro-crack formation in the acceptor substrate due to high pressure shock generation in the donor layer [90]. LISE utilizes the absorption of femtosecond duration laser pulses in a constrained metal film between two bulk substrates, at least one of which is transparent for the laser wavelength used. Very rapid pressure increase in the metal film following irradiation is believed to initiate crack-propagation in one or the other of the bulk substrates. By spatially shaping the laser beam, the cracking process can be controlled to etch solid chunks of material from the substrates. A unique feature of LISE is that the material etched from the bulk substrate is removed as a single solid piece and is not shattered, melted, or vaporized by the process. Hence, the etched material can be collected on the other bulk substrate used in the process [91].

All the techniques mentioned above (except DLW) are 1D, 2D or 2.5D. 1D and 2D fabrication is done on flat surface by moving the sample or scanning the laser beam in XY plane. 2.5D is a technique used to fabricate 3D objects layer by layer. Usually fabrication goes from the bottom layer up to the top layer. The Z coordinate is changed only when a certain XY layer is finished. In pure 3D techniques, the sample is moved in XYZ simultaneously during the fabrication process. It's applicable only for DLW fabrication of transparent materials bulk.

In this thesis, only DLA and DLW were used to perform the micromachining of surfaces and bulk of transparent materials.

1.5.1. Surface processing

FLM is widely used to process the surface of samples using different techniques [2,16, 17, 18 and etc.]. In this thesis, cases of selective thin metallic film ablation and formation of surface nano-ripples will be discussed.

1.5.1.1. Selective thin film ablation

DLA allows selectively ablate thin metal films deposited on the surface of dielectric substrates [92]. To avoid damage to the glass substrate, incident radiation energy and pulse density must be adjusted precisely. The ablation threshold of thin film metal layers is lower than the dielectric substrates damage threshold (DT). Thin film metal coatings on substrates are commonly produced using vacuum thermal evaporation deposition process.

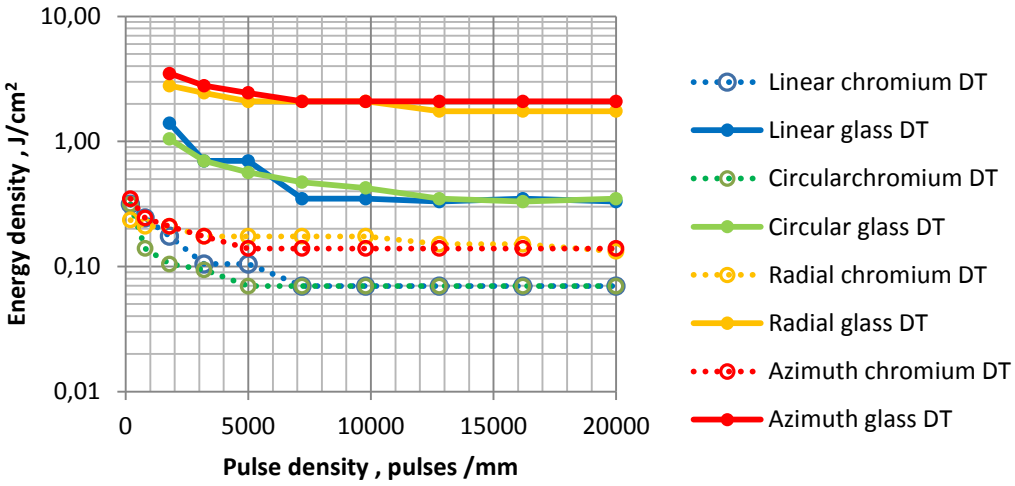

Figure 9 Thin (~200 nm thickness) chromium layer and glass substrate damage threshold dependence on incident pulse density and polarization state

Figure 9 shows the measured damage threshold for thin (~200 nm thickness) chromium layers and glass substrates as a function of incident pulse density and polarization state. Wavelength $\lambda = 1030$ nm, pulse duration $\tau = 300$ fs radiation was focused using an aspheric lens (focal length $f = 6{,}24$ mm, numerical aperture $NA = 0{,}4$) to a $2w_0 = 3$ μm spot. In this experiment, the incident radiation polarization states were linear, circular, radial and azimuth.

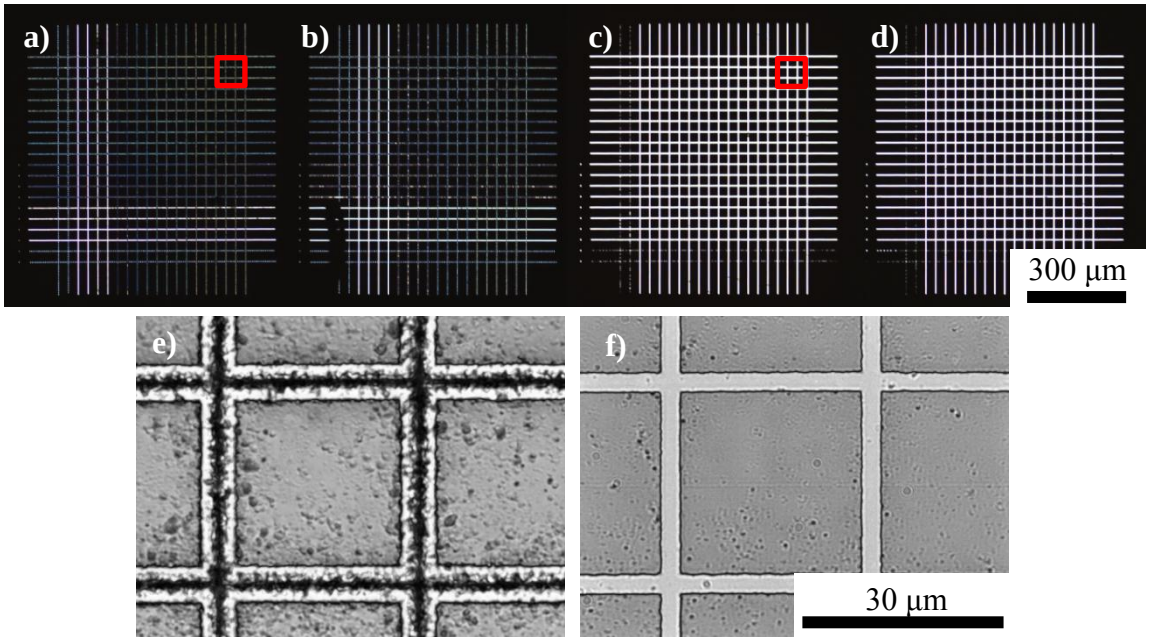

Figure 10 Optical microscope photo (transmitted light illumination) of structures ablated in a thin chromium layer with $\lambda = 1030$ nm, $\tau = 300$ fs, $\phi = 1$ J/cm^2 radiation with different polarization states: a) and e) linear, b) circular, c) and f) radial, d) azimuth polarization. Energy density was the same in all cases $\phi = 1$ J/cm^2. e) and f) are magnified a) and c) samples (areas shown with red square) photos made with transmitted and reflected illumination

The energy density needed to remove chromium layer does not depend strongly on the polarization state of the incident radiation and is around $\phi_{\mathrm{crDT}} = 0{,}1$ J/cm^2. Glass DT, however, does depend on the polarization state: $\phi_{\mathrm{glassDT}} = 0{,}4$ J/cm^2 for linear and circular polarizations, and $\phi_{\mathrm{glassDT}} = 2$ J/cm^2 for radial and azimuth polarizations. Clearly, there is a

regime, for all polarization states, in which thin metallic layers can be selectively ablated from dielectric substrates without damaging the substrate. Radial or azimuth polarizations should be used for selective metal layer ablation as the DT for chromium and glass is more than 6,6 times higher than using linear or circular polarization. For example, at $\phi = 1\,\mathrm{J/cm^2}$ thin chromium layers can be selectively ablated without damaging the glass substrate surface using radial or azimuth polarizations. At this energy density, the glass would be damaged using linear or circular polarization (Figure 10).

Selective laser ablation of thin metal films enables fabricating photonic devices, for example, amplitude holograms (described in chapter 3.1), as well as electroacoustic devices, for example – surface acoustic wave interdigital transducers (described in chapter 3.3) or phononic structures (described in chapter 3.4).

1.5.1.2. Formation of surface nano-ripples

In DLA applications self-organized surface nano-ripples are commonly observed occurring in a wide range of materials, such as titanium dioxide (TiO_2) [93], zinc selenide (ZnSe) [94], Zinc oxide (ZnO) [95], gallium phosphide (GaP) [96], soda-lime glass [97], dense flint (ZF_6) glass [98, 99] and other. The period of induced nanogratings is $\Lambda = \lambda/2n$, here n is sample refractive index and λ - laser wavelength. The mechanism responsible for the formation of fine nano-ripples on the surface on dielectrics and semiconductors is currently under discussion in [100, 101, 102]. Recently it was shown that the sphere-to-plane transformation of nano-plasma bubbles responsible for the in-bulk ripples [103] can explain ripples on the surface [104]. On the other hand, surface plasmon polaritons excited in the surface layer are said to be responsible for the formation of these nanostructures [105].

The formation of self-assembled nano-ripples on surfaces has applications in optoelectronic nanodevices [106], metal surface color marking [107], solar cells [108], polarization sensitive micro-optics [109] or other applications. Self-organized surface nano-ripples are not the subject of this thesis. Here we investigate bulk nano-ripples (described in chapter 1.5.2.2) that are used for the fabrication of radial and azimuthal polarization converter (described in chapter 3.6).

1.5.2. Bulk processing

The interaction of ultra-short laser pulses with the bulk of transparent dielectric materials results in three types of modifications: refractive index change [110], self-organized nanogratings [111] or void formation [112]. Self-focusing [113] and refractive-index mismatch induced spherical aberrations [114] occur during the fabrication of the bulk of dielectric transparent materials.

Localized modification of the bulk transparent material is a key advantage of FLM enabling the fabrication of new type 3D structures.

1.5.2.1. Refractive index modification

Under a wide range of writing conditions the refractive index modification in multicomponent glasses can be positive, negative, or non-uniform, and exhibits a strong dependence on the glass composition [110]. Induced refractive index change can be evaluated by applying Kogelnik's coupled mode theory to the measured diffraction efficiencies of the higher order diffracted beams from Bragg gratings fabricated by FLM [115].

Refractive index modulation is used in the fabrication of photonic crystals that are suitable for spatial light filtering (describe in chapter 3.5).

1.5.2.2. Formation of self-organized bulk nanogratings

Laser induced bulk self-ordered nanogratings can be formed in sapphire [116], fused silica, germanium-doped silica, sol-gel silica [117], tellurium dioxide crystals [118] and borosilicate glass [119]. Sphere-to-plane transformation of nano-plasma bubbles is responsible for the in-bulk nanograting formation [103]. Orientation of the nanogratings is perpendicular to the polarization direction of incident light [117]. By rotating the incident laser beam polarization during fabrication, one can control the orientation of induced nanogratings. Induced nanogratings consist of a periodic density change. The main reason for the density change is oxygen concentration differences induced by laser irradiation [111]. The properties of induced self-ordered nanogratings depend on the incident light pulse duration, repetition rate, focusing conditions, pulse energy and density. Nanogratings can be formed by using pulse durations ranging from 40 fs to 500 fs [120]. Recently, nanogratings formation at repetition rates as high as 9.4 MHz was demonstrated [121]. Period of induced nanograting varies from 140 nm to 320 nm [117].

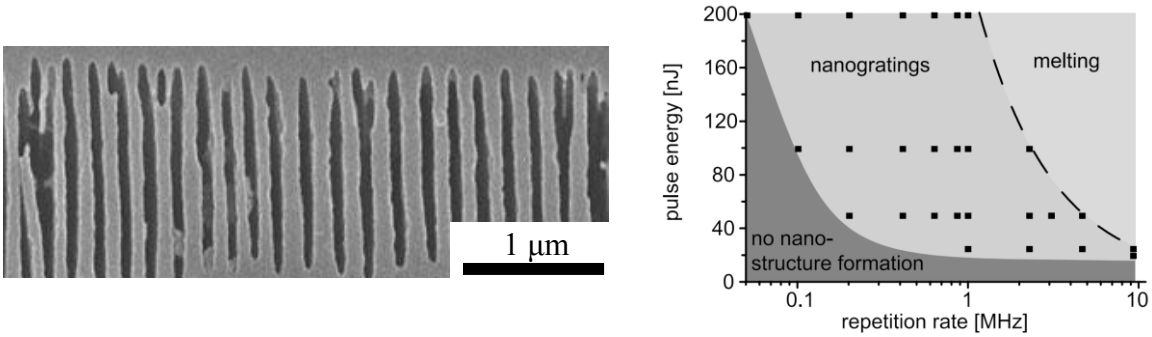

Figure 11 a) SEM image of self-ordered Λ = 200 nm period nanograting formed in fused silica using femtosecond (τ = 450 fs) second harmonic (λ = 515 nm) laser radiation. To gain access to the induced nanograting – the sample was polished and etched with hydrofluoric acid. b) Nanograting formation dependence on pulse energy and repetition rate [121]

When the period of the grating structure is smaller than the wavelengths of the incident light, the structure is considered to be an optically anisotropic medium [122]. *Birefringence* is a double refraction which refers to the phenomenon of light traveling with different velocities in crystalline materials depending on the propagation direction and the orientation of the light polarization relative to the crystalline axes. Birefringence is present naturally in anisotropic materials, such as calcite, tourmaline, quartz or sodium nitrate uniaxial crystals [123]. The effect can also occur in certain plastics, magnetic materials, various non-crystalline materials and liquid crystals [124]. B*irefringence* allows fabricating polarization sensitive elements, such as Fresnel zone plates, polarization diffraction grating, polarization converters [125] and polarization selective computer-generated holograms (PSCGH) [126]. The angle of slow axis in birefringent material depends on the orientation of induced nanograting.

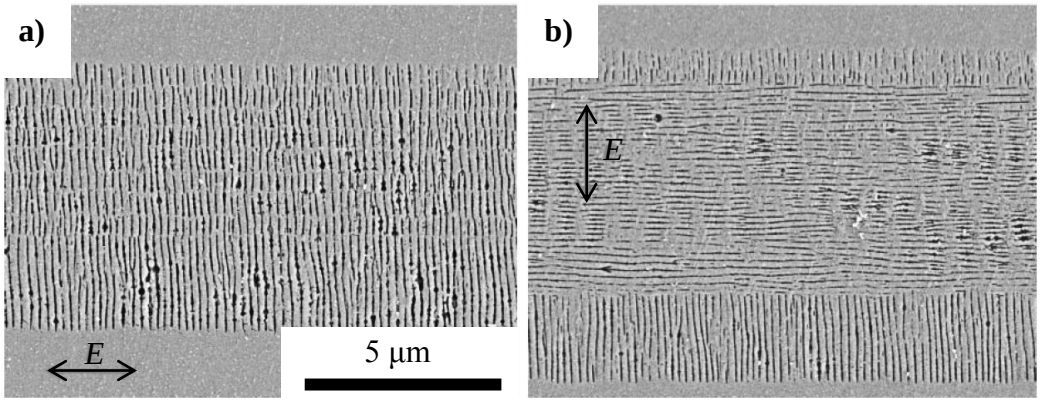

Figure 12 a) SEM image of nanogratings written with E polarization – parallel to writing direction. b) SEM image of the nanogratings after overwriting [127]

Bulk nanogratings are rewritable. If the polarization direction of the femtosecond light is changed, the existing nanogratings are erased and simultaneously replaced with the new ones, the orientation of which is solely determined by the polarization of the applied laser beam. Writing and rewriting large arrays of continuous gratings are shown in Figure 12 a) a SEM image of nanogratings written with E polarization – parallel to writing direction and b) a

SEM image of the nanogratings after overwriting. The central portion of the nanograting was rewritten with the electromagnetic field perpendicular to writing direction. The non-overwritten regions (top and bottom) show the original nanogratings [127].

The fabrication of micro-channels followed by chemical etching of bulk induced nanostructures is becoming a more and more widespread for bulk self-ordered nanogratings [128]. It allows fabricating 3D bio-photonic chips devices [129].

1.5.2.3. Micro-void formation

At peak intensities greater than 10^{14} W/cm^2, pressures exceeding the value of Young's modulus of the medium are generated in the focal volume, creating a shockwave after the electrons have transferred their energy to the ions. The shockwave leaves a less dense or hollow core (void) behind, depending on the laser and material properties [112]. The dynamics of femtosecond void formation in a-SiO_2 was investigated by time-resolved phase-contrast microscopy [130].

Micro-voids can be used to fabricate woodpile-type photonic crystal structures [131].

2. FemtoLAB femtosecond laser material micromachining system

FemtoLAB is a custom build, laboratory type, femtosecond class4 laser micromachining system. The femtoLAB system was designed and built by combining most advanced high-tech solutions. FemtoLAB integrates an Yb:KGW femtosecond laser, second, third and fourth harmonics generators, four motorized attenuators, four motorized polarization rotators, galvanometer scanners, power meter, spatial light modulator, machine vision, autofocus and precise 3 axis object positioning system. The main system components are described in chapters 2.1, 2.2, 2.3 and 2.4 of this thesis. Figure 13 shows the femtoLAB femtosecond micromachining system rendered CAD model view (left) and a photo (right). Figure 14 shows the optical scheme of the femtoLAB. In total, there are 18 different optical paths (marked with different colors), delivering laser generated (or converted) radiation to sample processing area. For safety reasons, the complete optical scheme is covered to eliminate any possible radiation leaking outside the system. The femtoLAB is capable of all FLM techniques described in chapter 1.5.

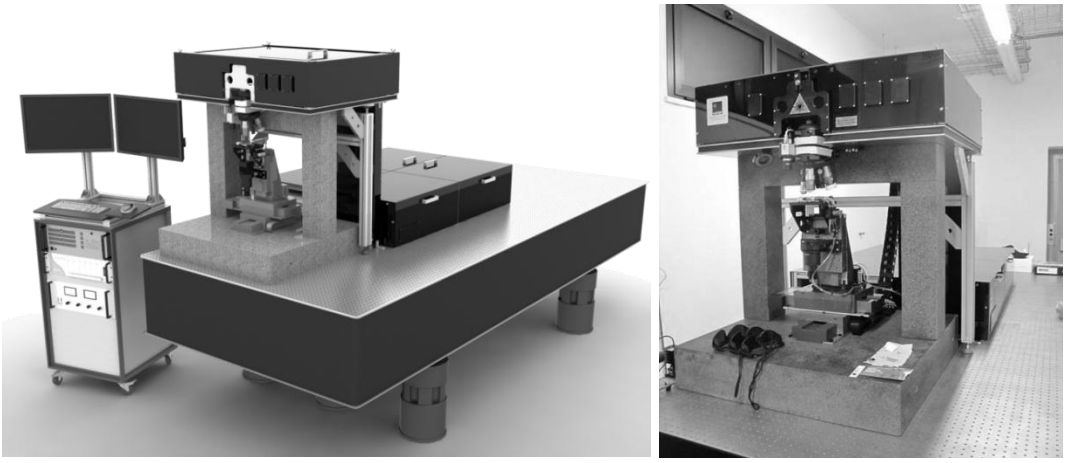

Figure 13 FemtoLAB femtosecond micromachining rendered CAD model view (left) and photo (right)

To increase the stability of the system, it was assembled on a $h = 500$ mm thickness honeycomb optical table, the positioning equipment is mounted on a granite base and has a granite bridge to support the part of the optical setup located above the optical table (Figure 14 left). The system footprint is 260 mm x 1060 mm, height 1080 mm. All system devices are controlled from a custom made software SCA (described in chapter 2.5).

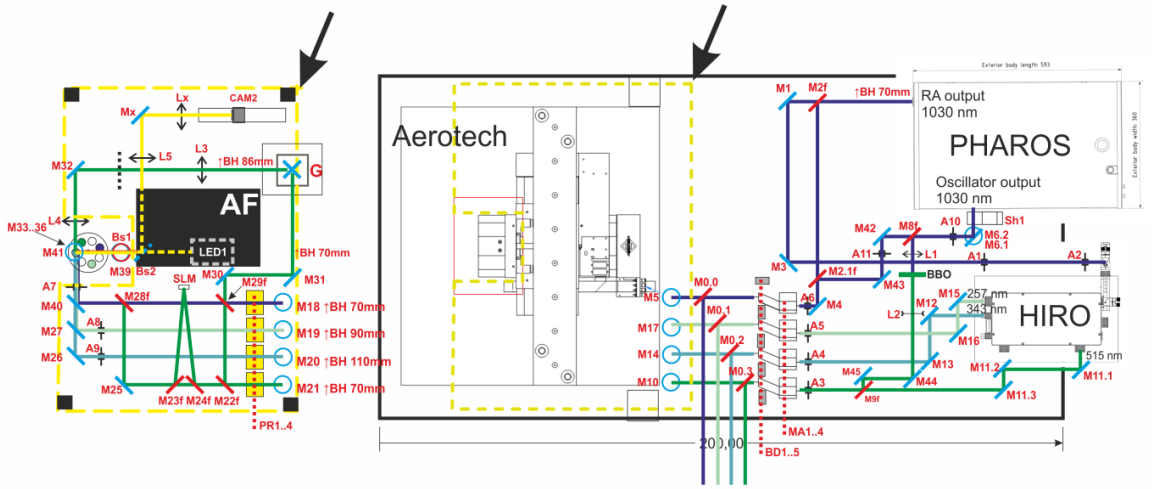

Figure 14 FemtoLAB femtosecond micromachining system scheme. Different optical paths are marked with different colors. Courtesy of Altechna (Lithuania)

The main advantage and uniqueness (in comparing to other commercially available femtosecond micromachining systems) of the femtoLAB system is a combination of market leading high tech opto-mechanical solutions: Yb:KGW femtosecond laser PHAROS, harmonics generator HIRO, air bearing three axis positioning system. Also, the system has custom written software (described in chapter 2.5) and it is equipped with a unique beam scanning system (described in chapter 2.3.1).

The femtoLAB system was developed for the Center of Nano Science and Technology of IIT@polimi (Milan, Italy). The femtoLAB system enables high precision micro-fabrication of 3D optofluidic circuits, waveguides, opto-chips and patterned surfaces for energy and photonics applications [132].

2.1. Main FemtoLAB components parameters overview

Main femtoLAB system components parameters (laser source, harmonics generator, sample positioning system, galvanometer scanners and spatial light modulator) are listed in Table 1.

Table 1 Main femtoLAB system components parameters.

Part	Parameter	Value
Laser	Lasing medium	Yb:KGW
	Max. average power (P)	10 W
	Wavelength (λ)	1028 nm ± 5 nm
	Max. pulse repetition rate (f_{max})	1 MHz
	Max. pulse energy ($E_{\mathrm{P\_max}}$)	200 μJ
	Pulse duration (τ)	300 fs
	Beam quality (M^2)	1,2
	Output pulse stability	<1 %
Oscillator	Oscillator power	2 W
	Oscillator repetition rate	82 MHz
	Pulse duration	80 fs
	Max. pulse energy	24 nJ
Harmonics generator	Second harmonic ($\lambda = 515$ nm) average power (P_{515_max})	6,6 W
	Third harmonic ($\lambda = 343$ nm) average power (P_{343_max})	3,3 W
	Fourth harmonic ($\lambda = 257$ nm) average power (P_{257_max})	0,32 W
	Switching between harmonics	manual
Sample positioning system	Axis	XYZ
	Servo type	air-bearing

	Total travel	150 mm x 100 mm x 50 mm
	Accuracy	±0,5 μm
	Repeatability	±50 nm
	Straightness and flatness	±0,4 μm
	Maximum travel speed	300 mm/s
	Maximum linear acceleration	10 mm/s^2
	Maximum load	15 kg
	Operating pressure	80 psi ±5 psi
Galvanometer Scanners	Axis	XY
	Scan field	Objective dependent
	Scan angles (10% full scale)	±5°
	Step response time (10% full scale)	1 ms
	Step response time (100% full scale)	3 ms
	Repeatability	< 22 μrad
	Long-term drift over 8 hours	< 0,6 mrad
Spatial light modulator	Pixels	1920 x 1080
	Active area	X: 15,36 mm Y: 8,64 mm
	Pixels size	8 μm
	Operating wavelengths	from 420 nm to 700 nm

2.2. Sample positioning systems overview

The femtoLAB system utilizes an ABL1000 series 3 axis, air-bearing positioning stages (Aerotech Inc., US). They are used to precisely translate sample in XYZ coordinates. ABL 1000 stages are driven by a linear brushless servomotor which allows reaching maximum positioning speed $v_{\max} = 300\,\mathrm{mm/s}$. The positioning system accuracy is $\pm 0,5\,\mu\mathrm{m}$, position feedback resolution 0,5 nm, repeatability ± 50 nm. In order to operate the air bearings stage – air supply (pressure 80 psi $\pm$ 5 psi) must be applied. The air consumption for 3 axis system is $42\,\mathrm{l/min}$. Supplied air must be clean, dry to the 0° F dew point, and filtered to 0,25 μm or better (recommend nitrogen at 99,99 % purity) [133].

The main parameters which describe perfection of positioning equipment are: accuracy, repeatability and resolution. ***Accuracy*** — for a specific point of interest in three-dimensional space, accuracy is the difference between the actual position in space and the position as measured by a feedback mechanism, drive mechanism and trueness of bearing ways. ***Repeatability*** — is the range of positions attained when the system is repeatedly commanded to one location under identical conditions. Unidirectional repeatability is measured by approaching the point from one direction, and ignores the effects of backlash or hysteresis within the system. Bi-directional repeatability measures the ability to return to the point from both directions. ***Resolution*** — the smallest possible movement of a system, also known as step size, resolution is determined by the feedback device and capabilities of the motion system [133]. A comparison, of two axis positioning systems with different accuracy and repeatability, is shown in Figure 15.

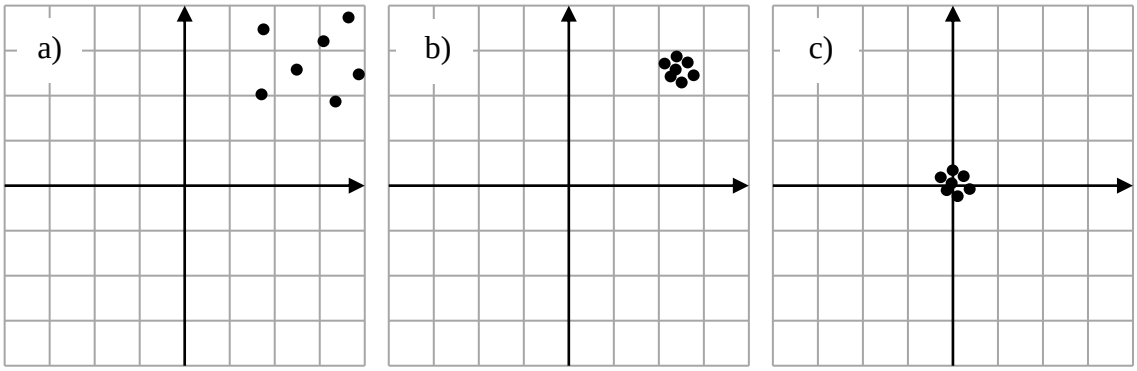

Figure 15 Different two axis positioning systems a) low accuracy and low repeatability, b) low accuracy and high repeatability, c) high accuracy and high repeatability [133]

There are many factors that affect the capabilities of a linear stage to position accurately in 3D space. Abbe errors, straightness, flatness, pitch, roll, yaw, hysteresis, backlash, orthogonal alignment, encoder errors, mounting surface, and cantilevered loading all contribute to positioning errors in 3D space [133].

An important sample positioning system feature is the position synchronized output (PSO). PSO generates output pulses (or sequences of pulses) based on real-time position feedback. It enables even pulse distribution while moving the sample at varying speeds: for example while accelerating or decelerating.

2.3. Laser beam management

The optical scheme of femtoLAB system is shown in Figure 14. It was assembled using $d = 25{,}4$ mm diameter mirrors with high reflectivity dielectric coatings mounted in kinematic mirror mounts. Some mirrors are mounted in flipping mounts, they are used to switch between different optical paths. In total, there are 18 different optical paths possible to guide different harmonics to the focusing optics. Different focusing objectives are mounted in a manual septuple revolving nosepiece. The numerical aperture of the focusing optics varies from $NA = 0{,}4$ for a long working distance X20 (effective focal length $f = 10$ mm) to $NA = 1{,}25$ for oil immersion X100 (effective focal length $f = 2$ mm) magnification objectives.

2.3.1. Laser beam scanning system

Galvanometer scanners are used to scan laser beams ($\lambda = 1030$ nm or $\lambda = 515$ nm) through focusing objective. A special optical scheme (shown in Figure 16) was assembled between galvanometer scanners and focusing objective. Such a 4-*f* scheme allows changing the incident beam angle without changing its position on the focusing lens aperture. The change of incident beam angle onto the objective exit aperture enables a focus shift in the XY plane. The distance *AB* between galvanometer scanner mirrors and focusing objective f_3 is equal to $2(f_1 + f_2)$. If $f_1 = f_2 = f$, it is equal to "$4f$". The beam shift distance on the sample surface can be evaluated by using formula:

$$\Delta x = \frac{f_1}{f_2} f_3 \mathrm{tg}(2\theta_x) \tag{15}$$

If $f_1 = f_2$, then $\Delta x = f_3 \mathrm{tg}(2\theta)$. The maximum scanning field is limited by the diameter and spherical aberrations of the f_1 and f_2 lenses, which increases

while increasing the incident angles. Therefore the f_1 and f_2 lenses should be at least 50 mm in diameter and have a focal length of $f > 200$ mm.

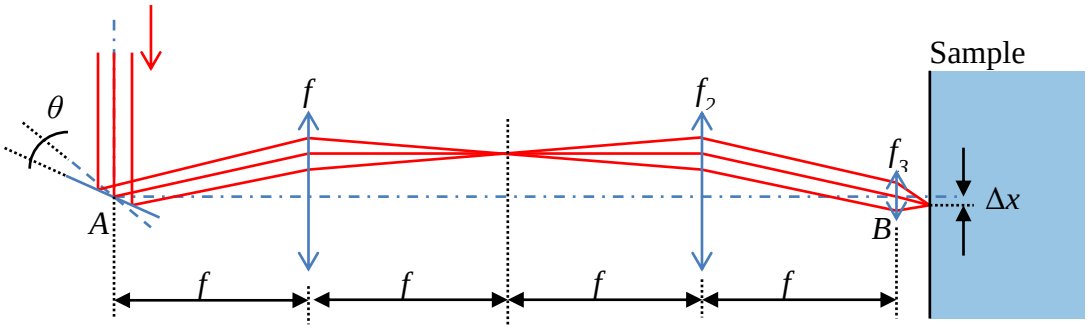

Figure 16 4f optical scheme used to scan laser beam through focusing lens

The fabrication time can be optimized by synchronizing the galvanometer scanners movement with the sample positioning system [134].

2.4. Machine vision

The femtoLAB has two machine vision (MV) cameras: one for an overall sample position detection, the second for micro monitoring. The MV micro monitoring camera is “looking” through the fabrication lens and shows the live fabrication process at 15 frames per second. It utilizes a monochrome charge-coupled device (CCD) camera with $\lambda = 590$ nm coaxial illumination. Both MV camera views are super-positioned with the sample fabrication preview trajectory (Figure 17).

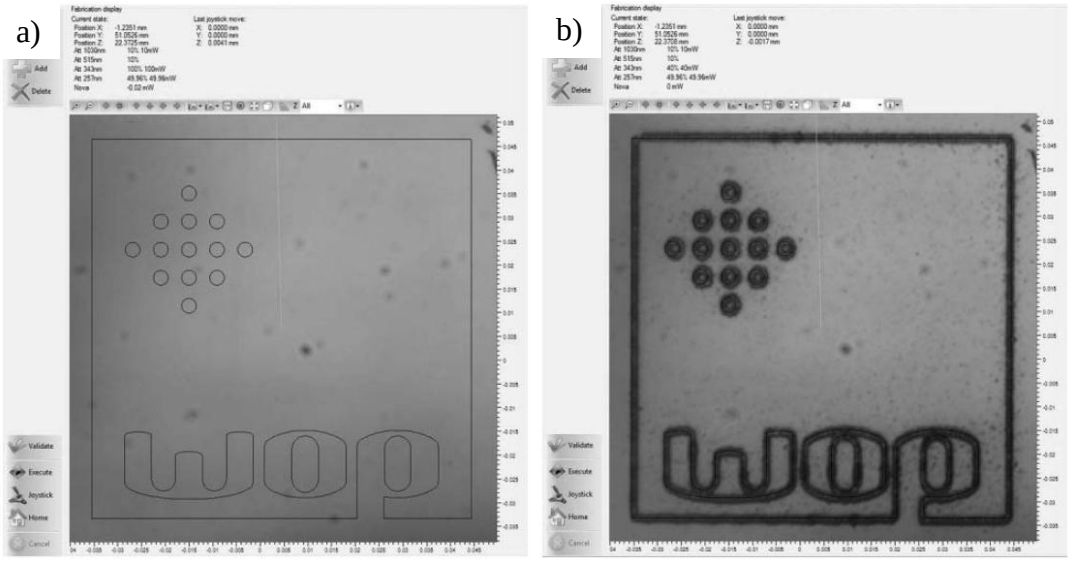

Figure 17 print screens of SCA software fabrication preview window: a) before fabrication, b) after. Fabrication algorithm preview is super positioned with MV sample preview. Courtesy of Altechna (Lithuania) [135]

The MV can detect the focus on the sample surface with < 1 μm accuracy. The focus detection algorithm is based on a highest contrast search by changing the z axis. The MV also has an automated sample tilting detection algorithm. It measures the focus position at three different points and calculates the sample surface plane tilting.

The MV simplifies FLM tasks. It is practically impossible to do FLM without a proper machine vision.

2.5. Software

The SCA software was developed (by Altechna Ltd.) to simplify femtosecond micromachining tasks. The main SCA advantage is the ability to integrate and control various hardware (different manufacturers) by using a unified technological parameter system. It controls all FLM system peripheral devices from a single window. SCA software main window is shown in Figure 18.

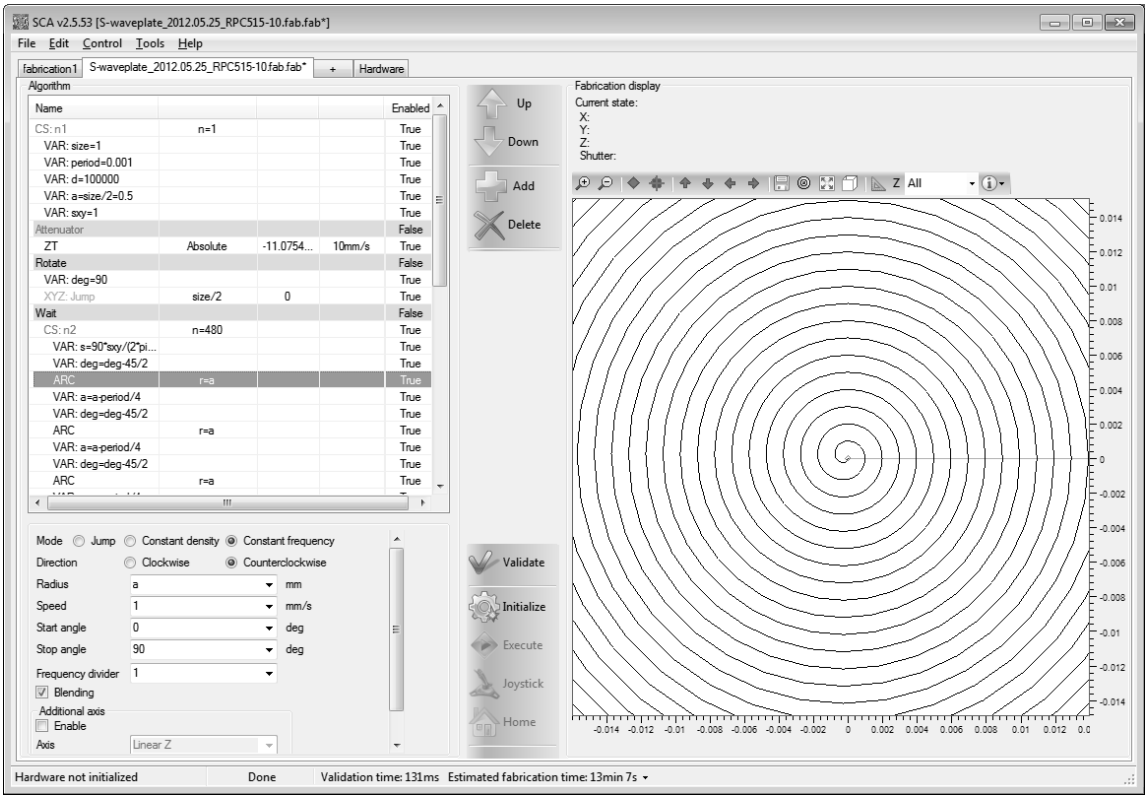

Figure 18 SCA femtosecond micromachining software print screen. Spiral fabrication trajectory can be seen in fabrication preview window

SCA software has a graphical fabrication preview window. Fabrication trajectories can be defined by directly writing move commands or by importing predefined 2D, 3D trajectories from *.bmp, *.stl, *.dxf or *.plt files. SCA enables writing of various FLM task algorithms.

3. Femtosecond laser material processing applications

3.1. Fabricating computer generated holograms for optical vortex generation

Optical vortices are point phase defects, they are also called phase singularities in the distribution of optical wave-fields where both real and imaginary values of the optical fields are equal to zero [136]. OV beam intensity distribution is ring shaped and the wavefront is helical. Light intensity at the center of the ring is always zero (even in the beam waist). The sign of topological charge *m* defines the handedness or helicity of the phase singular beam along the propagation direction of the z-axis. Topological charge m also defines the size of the ring dark core (see Figure 23). Wavefronts phase dislocations were discovered and described by J. F. Nye and M. V. Berry almost 40 years ago [136]. Recently, OV beams were used to fabricate ring shaped structures on glass substrate surface [137], novel shapes polymerization [138] and chiral metal nano-needles fabrication [139]. We use femtosecond OV beams to demonstrate fine hollow micro-tube structure photo-polymerization (see chapter 3.2).

OV beams can be generated by using spiral phase plates [140], phase computer generated holograms [141,142], uniaxial crystal converters [143], liquid crystal cells [144], dielectric wedge [145], higher-order laser beams [146] or using a space variant polarization converter, fabricated by femtosecond laser writing of self-assembled nanostructures in silica glass [147].

An amplitude CGH for the generation of femtosecond OV beams was fabricated in a thin (~ 200 nm thickness) chromium layer on a glass substrate by selective metal layer ablation [P4].

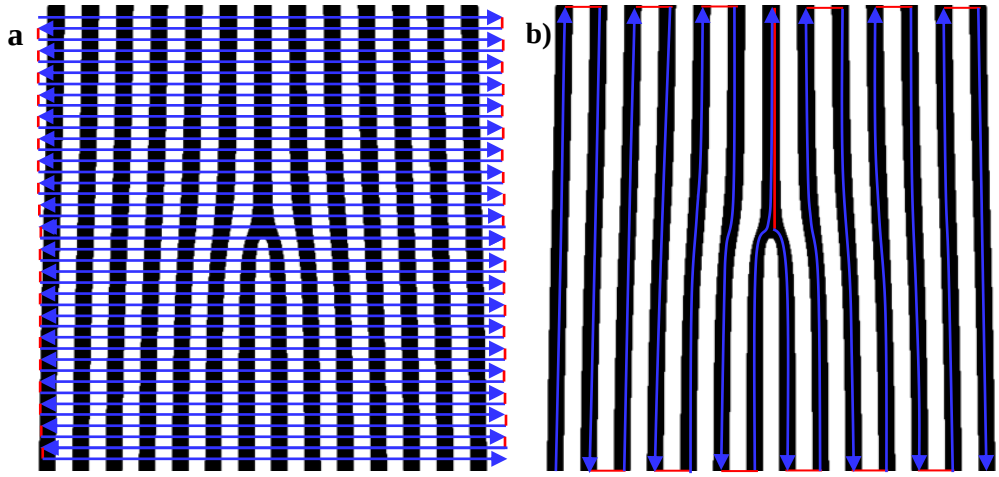

Figure 19 CGH raster (a) and vector (b) fabrication scanning trajectories. Blue lines indicates fabrication, red lines - jumps

A CGH can be fabricated using a raster or vector scan algorithm. Raster scanning takes much more time in comparison to vector scanning, as the trajectory length is much longer. For example, if we want to fabricate a CGH with a period of $\Lambda = 25$ µm, size of $A_x = 10$ mm by $A_y = 10$ mm with a resolution of $a = 1$ µm, the fabrication trajectory length for the raster method is $\frac{A_x A_y}{a} = 100000$ mm and for the vector only $\frac{A_x A_y}{\Lambda} = 4000$ mm. Thus, the raster scanning takes $\frac{\Lambda}{a}$ times longer than vector scanning. Figure 19 shows the fabrication trajectory of raster and vector CGH fabrication trajectories. Both methods result is the same – CGH grating with topological defect.

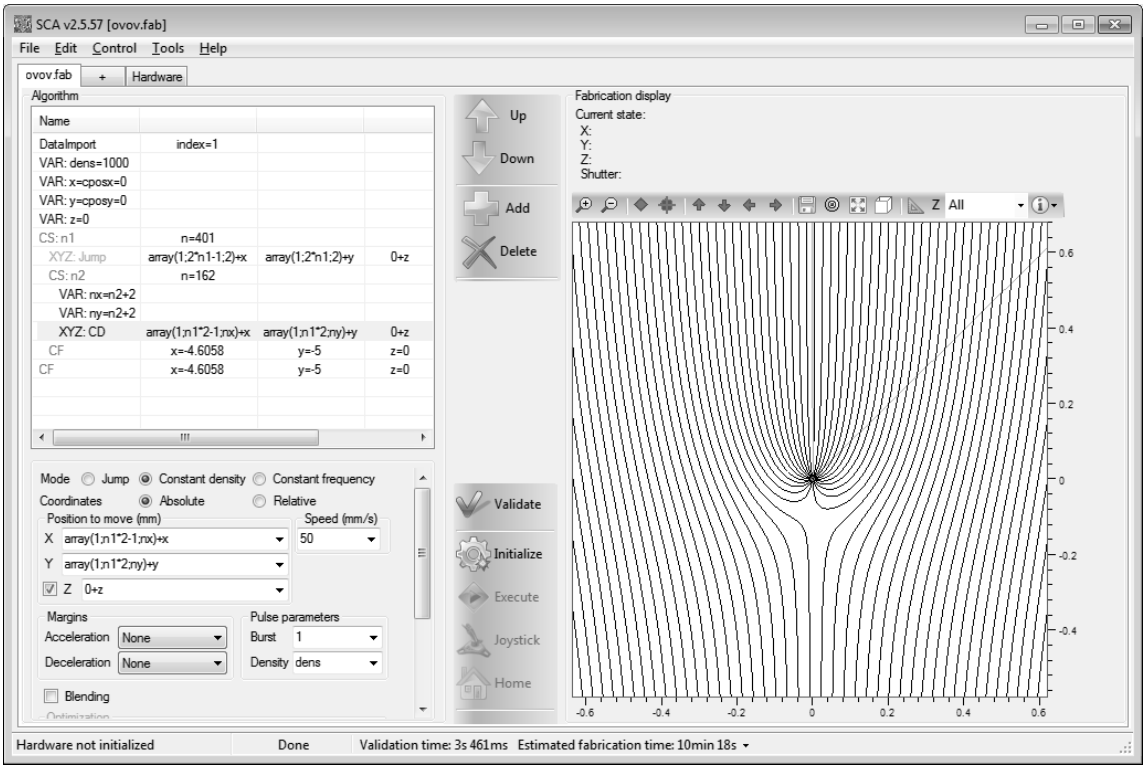

Figure 20 SCA software print screen. In the fabrication preview window center part of $m = 10$ topological charge CGH is shown

To calculate a CGH interferogram two waves, a planar reference wave and an object wave containing the desired OV, must be interfered [148]. The interferogram is given by the intensity of the interfering point vortex and reference wave:

$$I_{z=0}(x,\theta) = |E_0 + E_r|^2_{z=0} = 2C_0(1 + \cos(2\pi x/\Lambda) + \theta) \qquad (16)$$

here C_0 – reference and point vortex wave amplitude, $\Lambda = \lambda/\sin\varphi$ – is the spatial period of the plane wave. The interferogram calculation result is a 2D grating with bifurcation, which is later converted into a binary bitmap file and used for raster fabrication (Figure 19 a).

To calculate vector CGH fabrication trajectories, the skeleton equation described by J. Strohaber [149] was used:

$$y(x) = x \cdot \tan\left(\frac{2\pi}{m}(n + Kx)\right) \qquad (17)$$

here m – topological charge, $K \equiv k_x/2\pi$ is the number of grating lines per unit length, $n = 0, \pm 1, \pm 2, ...$ The periodicity of the tangent function in eq. (17) gives unwanted branches in the solutions. We exclude these branches by setting conditions on the angular argument of the tangent function for three different regions of the grating plane: positive x half-plane, negative x half-plane, and the line x = 0. For the skeleton equations in the regions x > 0 and x < 0 , we impose the following angular conditions (θ - azimuthal angle):

$$\begin{aligned} x > 0 \quad &\Rightarrow \quad -\frac{1}{2}\pi < \theta < \frac{1}{2}\pi \\ x < 0 \quad &\Rightarrow \quad \frac{1}{2}\pi < \theta < \frac{3}{2}\pi \end{aligned} \tag{18}$$

By substituting the argument of the tangent function $\theta = 2\pi(n + Kx)/m$ in the inequalities of eq. (18) the following conditions on the skeleton equations can be found:

$$\begin{aligned} x > 0: \qquad & -\frac{1}{K}\left(\frac{m}{4} + n\right) \le x \le \frac{1}{K}\left(\frac{m}{4} - n\right) \qquad \text{and} \quad n < \frac{m}{4} \\ x < 0: \qquad & \frac{1}{K}\left(\frac{m}{4} - n\right) \le x \le \frac{1}{K}\left(\frac{3m}{4} - n\right) \qquad \text{and} \quad n < \frac{m}{4} \end{aligned} \tag{19}$$

The last set of inequalities ($n < m/4$ and $n > m/4$) give the integer grating line numbers for which the first set of inequalities for x hold. For the equation of the line $x = 0$, the argument of the tangent function is degenerate:

$$n = \begin{cases} \frac{m}{4} & y > 0 \\ \text{undefined} & y = 0 \\ -\frac{m}{4} & y < 0 \end{cases} \tag{20}$$

Figure 20 shows SCA software main screen with the CGH (topological charge $m = 10$) fabrication algorithm loaded. SCA fabrication algorithm is used to import CGH fabrication trajectories generated using the skeleton equation (17).

Figure 21 shows an optical microscope image (front illumination) of selectively ablated thin chromium layer lines from a glass surface. Figure 21 shows the CGH at X100 magnification (shown in Figure 22 a - square). The fabrication parameters: wavelength $\lambda = 1030$ nm, pulse density $P_{\mathrm{D}} = 5000$ pulses/mm, pulse duration $\tau = 300$ fs. The energy density $\phi = 0{,}3\ \mathrm{J/cm^2}$ was chosen above metal film ablation threshold and bellow glass surface damage threshold. Smoothness of ablated lines is ~1 μm.

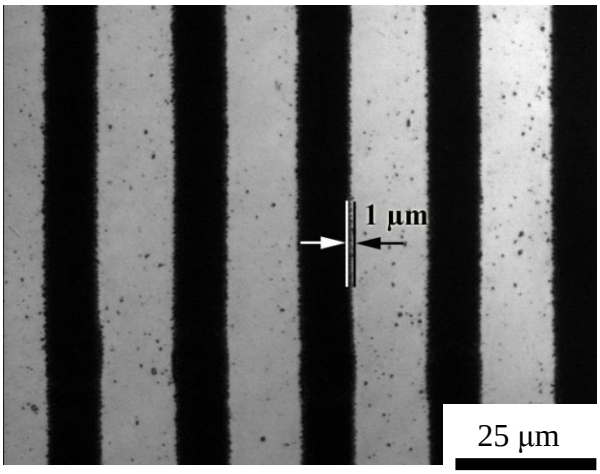

Figure 21 Optical microscope image (front illumination) of selectively ablated thin chromium layer lines from a glass surface. Fabrication parameters: wavelength $\boldsymbol{\lambda = 1030}$ nm, pulse density $\boldsymbol{P_{\mathrm{D}} = 5000\ \mathrm{pulses/mm}}$, pulse duration $\boldsymbol{\tau = 300}$ fs, energy density $\boldsymbol{\phi = 0{,}3\ \mathrm{J/cm^2}}$. Smoothness of ablated lines is ~1 μm

CGH's fabricated (using vector algorithm) in thin chromium layer coated on glass substrate with topological charges of $m = 1$, $m = 2$, $m = 3$, $m = 5$, $m = 10$, $m = 25$ are shown in Figure 22. The fabricated CGH size is $A_{xy} = 10$ mm, period $\Lambda = 25$ μm. The fabrication parameters are: wavelength $\lambda = 1030$ nm, pulse density $P_{\mathrm{D}} = 5000$ pulses/mm, pulse duration $\tau = 300$ fs, energy density $\phi = 0{,}3\ \mathrm{J/cm^2}$.

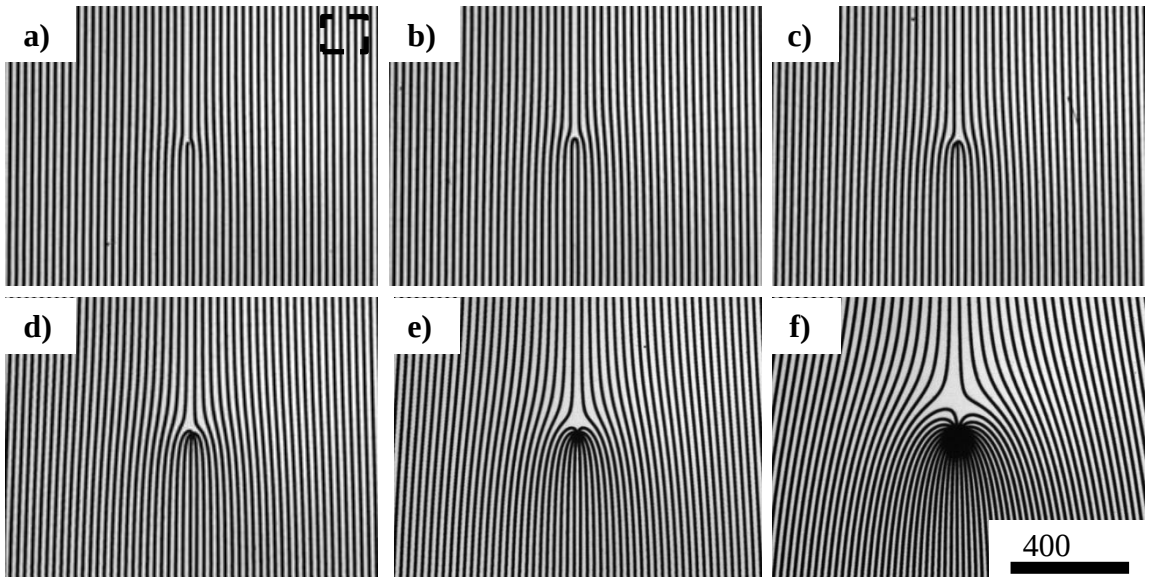

Figure 22 CGH with different topological charge *m* fabricated in thin chromium layer coated on glass substrate a) *m* = 1, b) *m* = 2, c) *m* = 3, d) *m* = 5, e) *m* = 10, f) *m* = 25. Grating period Λ = 25 µm. Photos were taken with optical microscope Olympus BX51. Fabrication parameters: wavelength $\lambda = 1030$ nm, pulse density $P_{\mathrm{D}} = 5000$ pulses/mm, pulse duration $\tau = 300$ fs, energy density $\phi = 0,3$ J/cm^2

The fabricated CGH work in both, transmission and reflection mode – in this research it was used in transmition mode. The CGH operates by means of interference and diffraction. Such amplitude CGHs can withstand incident electromagnetic radiation intensities of $I = 1{,}1 \cdot 10^9$ W/cm^2 (measured at $\lambda = 1030$ nm) and can generate OV beams to the first diffraction order with an efficiency of $\eta = 4{,}63$ %. $P_{OV} = 105$ mW is the maximum average power in femtosecond OV beam achieved with fabricated amplitude CGH (incident laser power was $P = 2{,}2$ W). The maximum femtosecond OV pulse energy at $f = 25$ kHz is $E_p = 4$ µJ. Maximum peak intensity $I = 9{,}9 \cdot 10^7$ W/cm^2 femtosecond OV beams can be generated using the fabricated CGH.

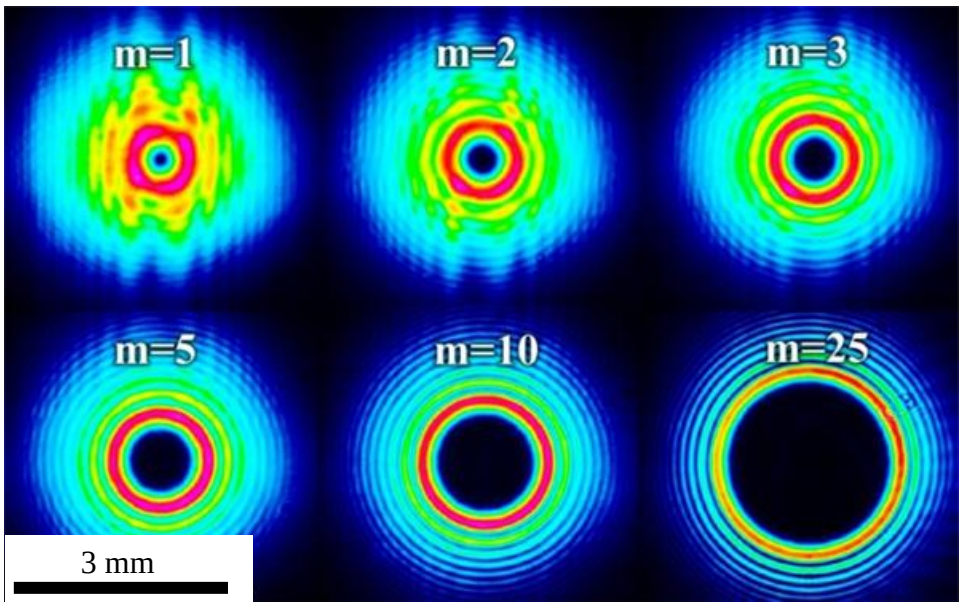

Figure 23 femtosecond OV beams (with different topological charge) intensity distributions measured with WinCamD camera (DataRay Inc.). The distance from camera to CGH was $l = 180$ mm

Different topological charge ($m = 1,\ m = 2,\ m = 3,\ m = 5,\ m = 10,\ m = 25$) femtosecond OV beams generated with CGH measured intensity distributions are shown in Figure 23. The intensity distributions were measured with the WinCamD CCD camera (DataRay Inc.) at same the distance $l = 180$ mm from CGH. Generated femtosecond OV beam ($m = 10$) measured at different distances from CGH intensity distributions are shown in Figure 24.

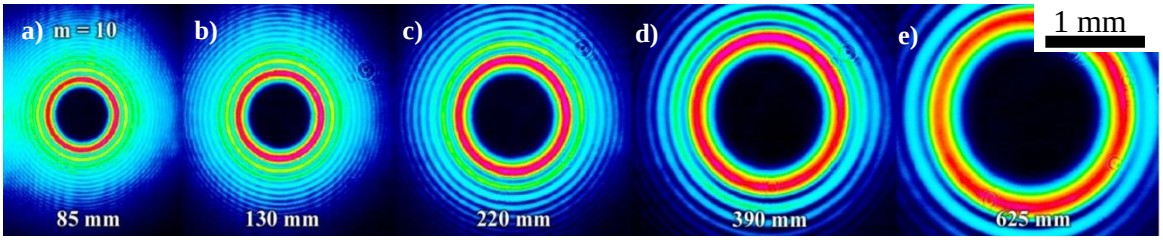

Figure 24 Femtosecond vortex beam (m = 10) measured intensity distributions at different distances from CGH: (a) 85 mm; (b) 130 mm; (c) 220 mm; (d) 390 mm; (e) 625 mm

The calculated (a) [150] and measured (b) femtosecond OV beam intensity distributions with topological charge $m = 10$ are shown in Figure 25. Figure 25 c) shows a cross-section intensity distribution of measured femtosecond OV beam ($m = 10$) (marked with the dashed line in Figure 25 b)).

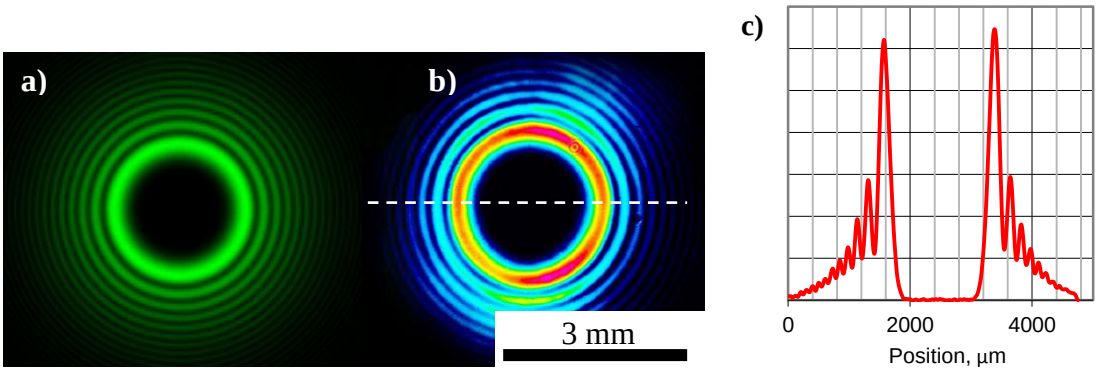

Figure 25 Femtosecond OV beam (m = 10) intensity distribution: calculated (a) [150] and measured (b). c) Cross-section intensity distribution profile of measured femtosecond vertex beam (m = 10) (marked with dashed line in (b))

Structures induced in thin chromium layer using single femtosecond vortex pulses (λ = 1030 nm; $P = 100$ mW; $f = 50$ kHz) with different topological charge ($m = 1; m = 2; m = 3; m = 5; m = 10;$ m = 25) are shown in Figure 26. Figure 26 g shows $m = 25$ single femtosecond vortex pulse induced $d = 23$ µm diameter ring shaped structure with $a = 2$ µm ring width.

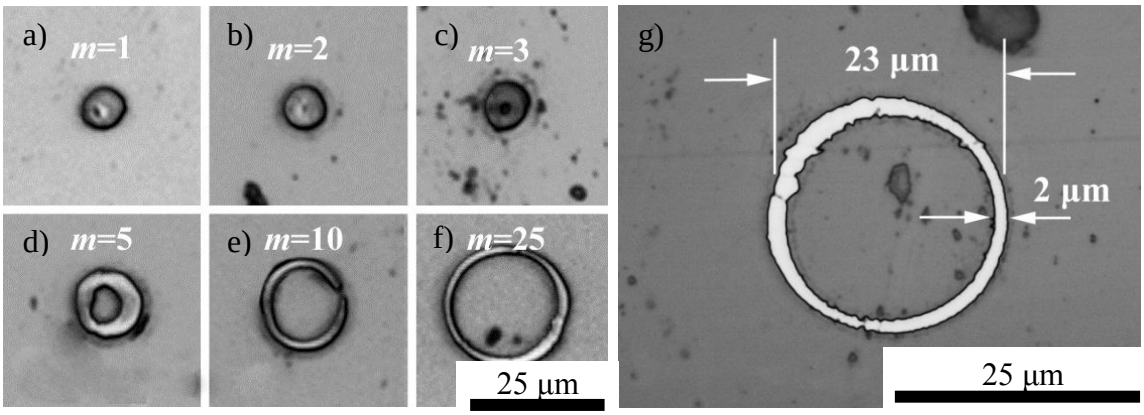

Figure 26 Optical microscope images of ring shaped structures ablated in a thin chromium layer using single femtosecond OV pulses ($\lambda = 1030$ nm; $P = 100$ mW; $f = 50$ kHz) with a different topological charge (a) m = 1; (b) m = 2; (c) m = 3; (d) m = 5; (e) m = 10; (f) m = 25 (g) zoomed m = 25

Structures induced on a borosilicate glass surface using single femtosecond vortex ($m = 1$) pulses with an energy of $E_P = 7$ μJ are shown in Figure 27 (a-i) for different beam waist position. The maximum available pulse energy was $E_P = 7$ μJ. We used an aspheric lens (NA $= 0{,}62$) with $f = 4{,}03$ mm focal length and 5 mm clear aperture. The shape and size of induced structures greatly depend on beam waist shift Δz. Induced structures vary from perfect ring-shaped to multiple rings. When $\Delta z = 43$ μm, induced structure size becomes ≈ 500 nm, which is less than the wavelength $\lambda = 1030$ nm used. When $\Delta z > 45$ μm, no more structures are induced on the surface of borosilicate glass, instead we can detect volume modifications (Figure 28).

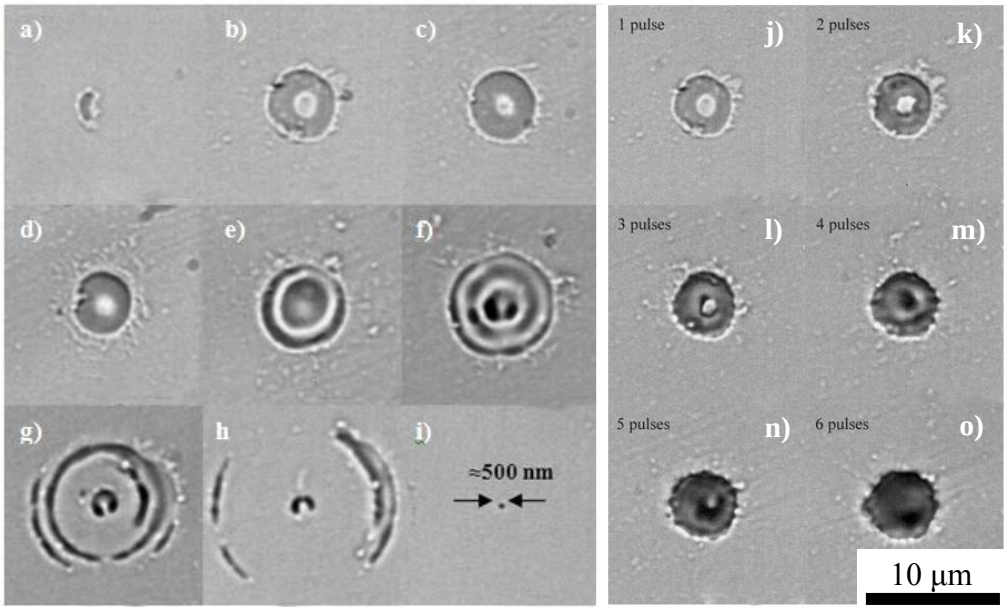

Figure 27 Structures induced on borosilicate glass surface using single femtosecond vortex ($m = 1$) pulses with different beam waist shift a) $\Delta z = 1$ μm, b) $\Delta z = 6$ μm, c) $\Delta z = 11$ μm, d) $\Delta z = 16$ μm, e) $\Delta z = 21$ μm, f) $\Delta z = 26$ μm, g) $\Delta z = 31$ μm, h) $\Delta z = 36$ μm, i) $\Delta z = 43$ μm. Structures induced on borosilicate glass surface using different number of femtosecond vortex ($m = 1$) pulses: j) $N = 1$, k) $N = 2$, l) $N = 3$, m) $N = 4$, n) $N = 5$, o) $N = 6$

Different number of pulses also influences shape of induced structures. Structures induced on a borosilicate glass surface by using a different number of

femtosecond vortex ($m = 1$) pulses are shown in Figure 27 (j-o). Ring shaped structures disappear if several pulses shoot to the same place.

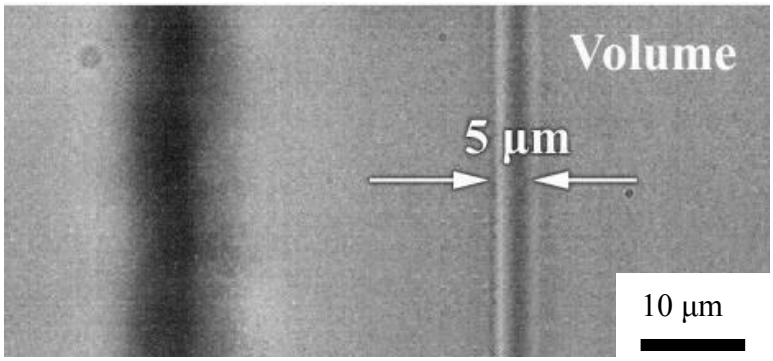

Figure 28 bulk modifications made inside the volume of borosilicate glass using femtosecond vortex beam with topological charge *m* = 2

To conclude, the structures induced on the borosilicate glass surface and in a thin chromium layer using single femtosecond vortex pulses highly depend on the beam waist position, number of pulses, pulse energy and topological charge. The possibility to fabricate nanometer sized structures (≈ 500 nm), as well modify the volume of dielectric material with femtosecond vortex beams was demonstrated. In our experiments we were not able to machine high-quality micron-size ring-shaped structures with less than 100 nm uniform groove thickness as shown in [151]. This is probably because of the lower NA focusing lens, longer pulse duration and amplitude CGH used. Amplitude CGHs are inherently chromatic and therefore require the introduction of correcting elements in order to compensate the topological charge dispersion occurring in femtosecond pulses.

3.2. Fabricating micro-tubes using femtosecond optical vortex beam

Fabrication of micro-tubes by multiphoton polymerization using a femtosecond optical vortex beam was demonstrated [P6]. Femtosecond OV beams were generated by using the CGH described in chapter 3.1. An aspheric lens $f = 6$ mm was used to focus the OV beam into a photopolymer SZ2080. The intensity distribution in the focused OV beam remains ring shaped [P4]. The diameter w_0 of the focused ring size can be evaluated from $w_0 = \frac{r_0}{\sqrt{m/2}}$, here $r_{\max}$ is the maximum radius of the vortex beam, m is the topological charge. Pulse energy was chosen in such a way that only the inner ring had intensity above the photo-polymerization threshold. Figure 29 shows a SEM image of the double sided micro-tube. Micro-tubes outer ring is fabricated because the intensity of OV beam second ring (Figure 25 b) was high enough to initiate the polymerization process.

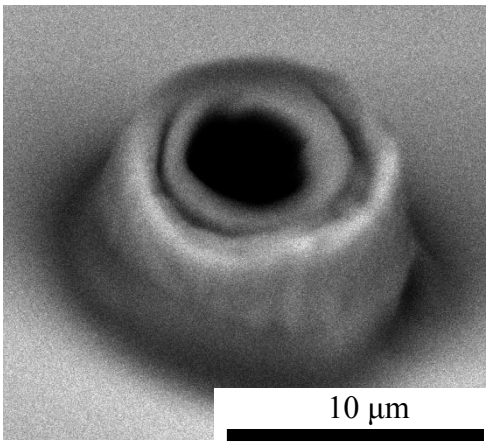

Figure 29 SEM image of micro-tube with double wall. Outer ring is fabricated because intensity of second ring OV beam used (Figure 25 b) is high enough to initiate polymerization process

The OV peak fluence in the focus was calculated using the formula:

$$\phi = \frac{1}{|m|!}\left(\frac{m}{e}\right)^m \frac{2E_{\mathrm{P}}}{\pi w_0^2} \tag{21}$$

here e is the Euler number, E_P is the pulse energy, n is the number of beams, w_0 is the focused beam radius. Peak fluence $\phi = 0{,}04\ \mathrm{J/cm^2}$ was used to fabricate free standing micro-tubes inside the photosensitive material. Micro-tubes were fabricated by only moving the focus plane of the OV with the translation velocity of $v = 1\ \mathrm{mm/s}$ in z direction. The height of the micro-tube depended on the scanning distance along the z axis. Maximum free standing micro-tube height $H = 100\ \mu\mathrm{m}$ was achieved.

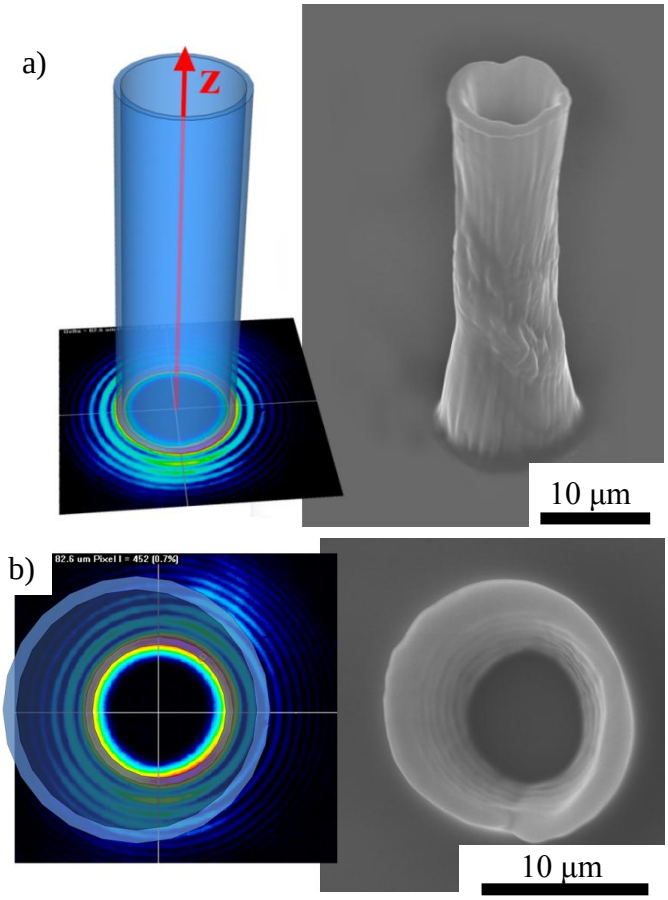

Figure 30 Modeling (left) and SEM images (right) of free standing micro-tubes fabricated using OV beam: (a) 45° tilted and (b) top view. Process parameters: $\lambda = 515\ \mathrm{nm}$, $E_P = 0,03\ \mu\mathrm{J}$, $P_D = 200000\ \mathrm{pulses/mm}$ [P6]

Figure 30 shows the modeling (left) and SEM images (right) of free standing micro-tubes fabricated using the OV: (a) 45° tilted and (b) top view. Surface roughness of the fabricated micro-tubes was affected by the irregularity in

the OV beam intensity distribution and possibly by helical wavefront. Figure 31 shows SEM images of a 20 x 17 micro-tube array fabricated using different energies and z translation distances. Figure 31**a** shows a SEM view from top, Figure 31**b** shows a 45° tilted view (the zoomed in area in **b** is marked with white dash line in **a**). If the micro-tube height exceeds $H > 100\ \mu m$ it can fall over (probably during the photoresist cleaning procedure).

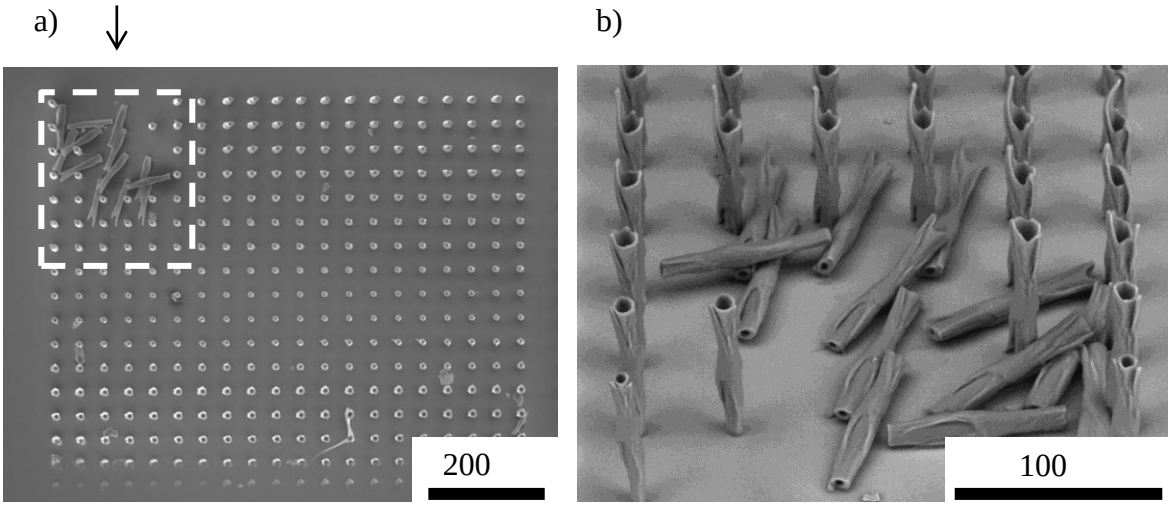

Figure 31 SEM images of micro-tube array fabricated using different energies and z translation distances. a) View from top, b) 45° tilted view (zoomed in area in b is marked with white dash line in a)

To conclude, multi-photon polymerization technique is a versatile tool for the formation of complex structures. We have demonstrated [P6] three different approaches to fabricate arrays of micro-tubes: direct laser writing (DLW), optical vortex (OV) and holographic (HL). The OV method demonstrates a good ratio between productivity and quality of the fabricated micro-tubes but this technique can be applied only for the fabrication of micro-tubes with the fixed size and orientation. The fabrication time of one micro-tube height of $60\ \mu m$ and inner radius of $3\ \mu m$ by using the OV method is 500 times shorter than by the DLW method and $1{,}25$ times shorter than using the holographic method. The fabrication time of the micro-tube array containing 400 micro-tubes with $60\ \mu m$ height and

3 μm inner radius is the shortest by the HL method as HL approach does not take time for sample translation while in the DLW and OV methods the sample translation is inevitable. When period between micro-tubes is $\Lambda = 30$ μm and sample translation velocity in the DLW and OV method is $v = 1$ mm/s, the fabrication time of the micro-tube array mentioned above by the HL method becomes 400 times faster than by the DLW and 1,2 times than by the OV method.

3.3. Fabricating surface acoustic wave transducers

Interdigital transducers (IDT) [152] are the key components of various surface acoustic wave (SAW) devices used for signal processing, communication, and sensing. The conventional technologies of planar microelectronics, such as photolithography and electron-beam lithography, are the main methods of IDT fabrication. However, advances in ultra-short pulse laser micromachining [153] stimulate interest in application of this technique for the IDT fabrication. The employment of FLM [154, 155, 156] allows sharp-edged, clean, and highly reproducible selective metal film ablation (described in chapter 1.5.1.1) with little or no heat affected zone (HAZ) or damages outside the focal spot and with the space resolution comparable to that of standard $\lambda = 248\ \mathrm{nm}$ photolithography.

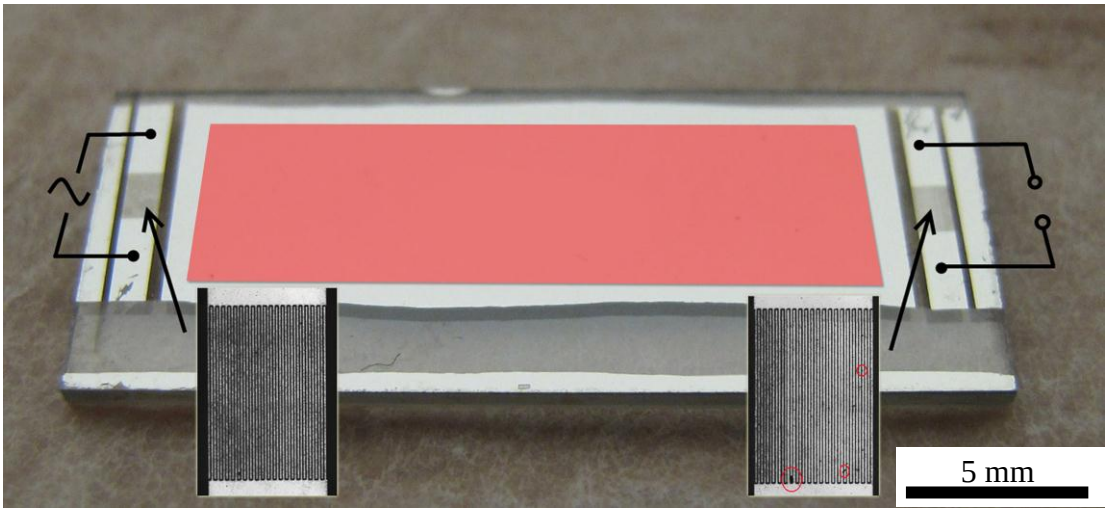

Figure 32 Two port IDT system fabricated by FLM in an aluminum layer deposited on a single-crystal lithium niobate ($LiNbO_3$) substrate

FLM is a one-step procedure and does not require multi-step processing, such as photoresist deposition, exposition, development, and etching, inevitable in lithography technologies. Selective ablation of metallic layers from dielectric surfaces with micrometer resolution has been demonstrated [157], but no reports on the fabrication and performance of laser fabricated SAW devices were available. One of the most widely used SAW materials is single-crystal lithium niobate ($LiNbO_3$). Due to the non-linearity of $LiNbO_3$, the deposition of exact

amount of $\lambda = 1030\,\mathrm{nm}$ radiation which is needed to selectively ablate aluminum layer can be tricky, because of second harmonic generation. Another difficulty arises from the relatively long distances between transmitting and receiving IDTs (22 mm in our work) requiring a very precise sample and focus field alignment over the entire writing area. In paper [P2], we report on the fabrication of the interdigital transducers on $\mathrm{YZ-LiNbO_3}$ by femtosecond pulse ablation and the performance characteristics of the two-port SAW device on their basis.

The two-port interdigital SAW transducers were formed by selectively ablating a thin (300 nm) aluminum layer deposited on a flat Y surface of $\mathrm{LiNbO_3}$ single crystal by thermal aluminum evaporation in a vacuum chamber. The centre-to-centre IDT spacing was 22 mm in the SAW propagation direction along the Z-axis of the crystal. The fabricated IDT SAW device has an insertion loss of 11 dB at $f = 68\,\mathrm{MHz}$. The IDT parameters (Table 2) measurements revealed no degradation in the elastic, piezoelectric, and dielectric properties of the substrate due to laser processing.

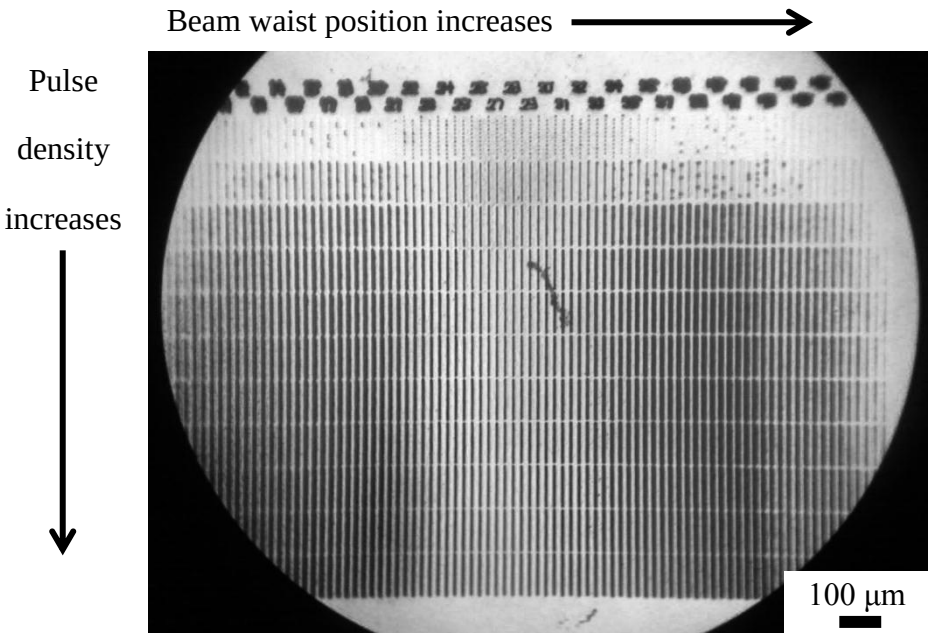

Figure 33 Optical microscope image (front illumination) showing experiment results of selective ablation of thin aluminum layer from $\mathrm{LiNbO_3}$ crystal surface. Variable parameters: pulse density (from $100\ \mathrm{pulses/mm}$ to 200000 pulses/mm) and waist position ($\Delta z = 2\ \mu\mathrm{m}$)

A Yb:KGW laser wavelength of $\lambda = 1030\,\mathrm{nm}$ and pulse duration of $\tau = 300\,\mathrm{fs}$ was used. The aspheric lens with focal length of $f = 11\,\mathrm{mm}$ allowed focusing the laser beam down to a spot size of $2w_0 = 12\,\mu\mathrm{m}$. At $f = 200\,\mathrm{kHz}$ and $P = 100\,\mathrm{mW}$, the energy density at the waist is $\Phi_w = 0{,}88\,\mathrm{J/cm^2}$. Pulse density $P_\mathrm{D} = 1000\,\mathrm{pulses/mm}$ was chosen. Fabrication parameters were selected after performing ablations tests at different energies, pulse densities, and focus positions. Figure 33 shows an optical microscope image (front illumination) of the experiment results – selective thin aluminum layer ablation from $LiNbO_3$ crystal surface. Variable parameters are: pulse density (from $P_\mathrm{D} = 100\,\mathrm{pulses/mm}$ to $P_\mathrm{D} = 200000$ pulses/mm) and waist position ($\Delta z = 2\,\mu\mathrm{m}$).

A fabricated SAW device is depicted in Figure 34. The discontinuous ablation grooves (seen in Figure 34 a)) which occurred during fabrication were repaired by applying additional laser pulses. The zoomed in view in b) reveals debris which occurred during the selective metal layer ablation. Such surface contamination does not affect fabricated IDT functionality however.

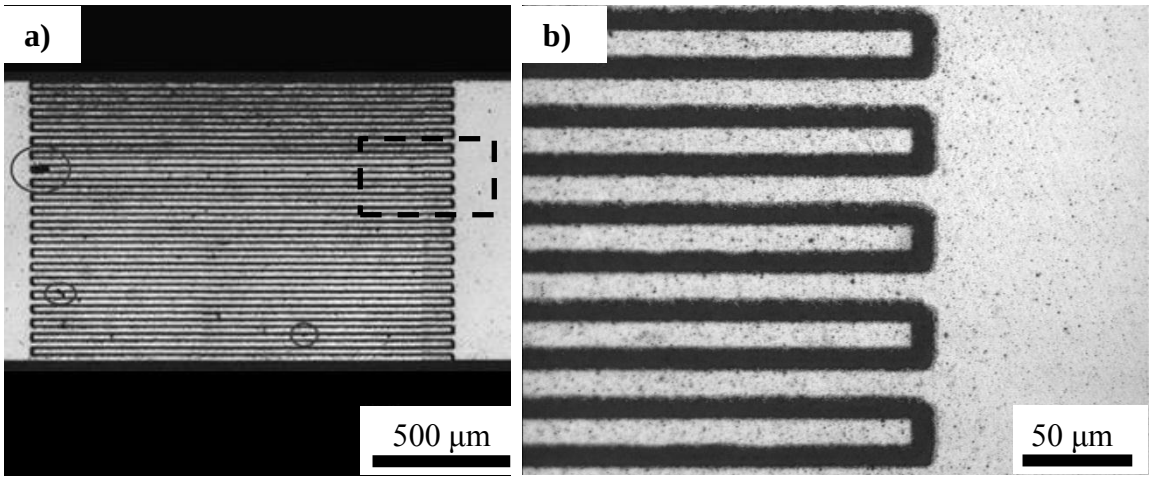

Figure 34 Optical microscope images (different magnifications) of SAW transducer device fabricated in aluminum layer deposited on $LiNbO_3$ surface. In a) circles indicated places which were repaired with additional laser pulses. b) Shows magnified IDT (area marked with square in a)

The width of the IDT strip electrodes and the gap between them was $l = 12{,}5$ μm resulting in the SAW wavelength of $\lambda = 50$ μm. Both IDTs had the same aperture of $A = 1{,}5$ mm, but slightly different numbers of electrode pairs, $N_1 = 20$ and $N_2 = 16$. SAW device parameters were measured with the radio-frequency network analyzer E5062A (Agilent Technologies, USA). The frequency dependencies of real and imaginary parts of IDT admittance extracted from measurements for IDT #1 are shown in Figure 35 a). The corresponding dependencies for IDT #2 are analogue as for IDT #1. The same dependencies were calculated using the crossed-field model expressions for IDT radiation conductance and susceptance, which can be found elsewhere [158]. The calculations parameters are given in Table 2.

Table 2 IDT calculation parameters

Parameter	IDT #1	IDT #2
Centre frequency, f_0	68 MHz	68 MHz
Acoustic wavelength, Λ	50 μm	50 μm
SAW velocity, v	3,40 km/s	3,40 km/s
Electrode pairs, N	20	16
Aperture, W	1,5 mm	1,5 mm
Electromechanical coupling coefficient, K^2	4,6 %	4,6 %
Capacitance, C	15,2 pF	13,4 pF
Parasitic inductance, L	33 nH	33 nH
Parasitic resistance, R	7 Ω	7 Ω

The capacitance per unit-length of the IDT electrode pair was determined from independent AC bridge measurements at 1 MHz frequency. The SAW velocity v and the electromechanical coupling coefficient K^2 in the transducer fabrication area were determined from the best fit of calculated IDT admittance dependencies on frequency with the experimentally obtained ones. The obtained values $v = 3{,}40$ m/s and $K^2 = 4{,}6$ % are in good agreement with literature

data, which are $v_l = 3{,}488\,\mathrm{m/s}$ and $K_l^2 = 4{,}6\,\%$ [158]. This confirms that neither elastic nor piezoelectric and dielectric properties at the crystal surface have been affected by the FLM of the deposited aluminum layer.

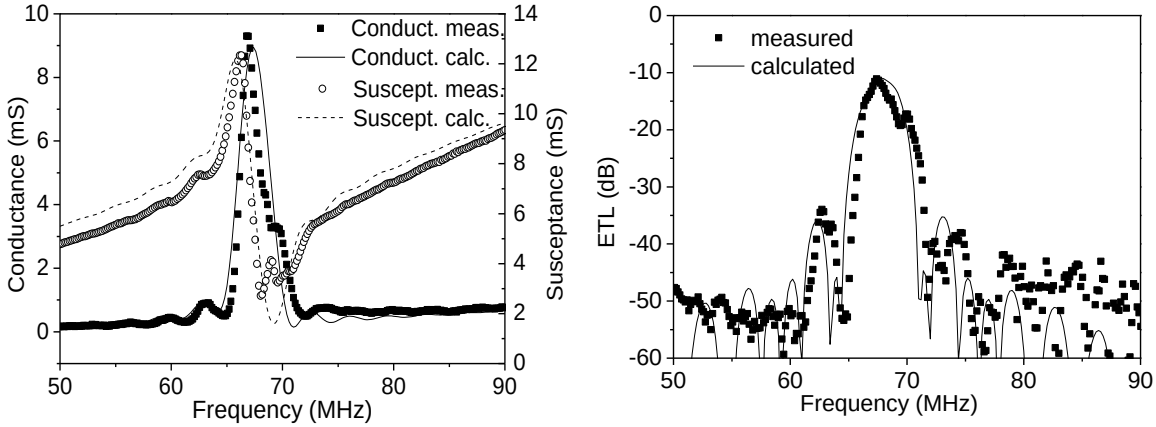

Figure 35 a) Laser-fabricated IDT #1 admittance. b) Effective transmission loss of laser fabricated two-port SAW device

The transmission characteristic of the fabricated two-port SAW device is shown in Figure 35 b). The frequency dependence on the transmission loss was extracted from measurements and calculated from transmission line model as described in [158] using the above determined IDT parameters. Transmission loss at the center frequency of 68 MHz is 11 dB, and an overall good agreement between measured and calculated curves is obtained. Measurements and characterization were done by P. Každailis.

To conclude, interdigital surface acoustic wave transducers were fabricated by FLM in thin-film aluminum layers deposited on a YZ lithium niobate crystal surface. The S-parameter measurements did not reveal any degradation in the dielectric, piezoelectric, and elastic properties of the substrate due to ablation of the metal overlay. FLM may be advantageous for fabrication of IDTs on substrates with fragile pre-deposited sensing structures, which could be damaged during standard photolithography process. Due to the ability of flexible programming of the transducer pattern, the laser technology can be very useful for the fabrication of SAW devices on curved surfaces, such as SAW-ball devices.

3.4. Fabricating surface acoustic wave phononic crystals

To control SAW dispersion we fabricate phononic crystals (PC) [P5]. Two different PC structures, with the same dimensions of 17 mm and 7 mm along the Z and X axes of the $LiNbO_3$ substrate, were formed by selective LA (described in chapter 1.5.1.1) on the SAW propagation path (shown light red in Figure 32). The first one, referred to as 1D structure, consists of $D = 23{,}5$ µm wide strips and $a \approx 1{,}5$ µm gaps between them, perpendicular to the SAW propagation direction. Hence, the structure period in Z direction was $\Lambda = 25$ µm, and the number of periods was 680. The second one, referred to as 2D structure, consists of squares with side dimensions of $D = 23{,}5$ µm, positioned at equal distances of $a \approx 1{,}5$ µm from each other. The structure had the same periodicity of $\Lambda = 25$ µm, and the number of periods in Z and X directions was 680 and 280, respectively. Fabricated 2D PC devices are shown in Figure 36. Second harmonic ($\lambda = 515$ nm) of the Yb:KGW laser was used to fabricate the PC devices [P5].

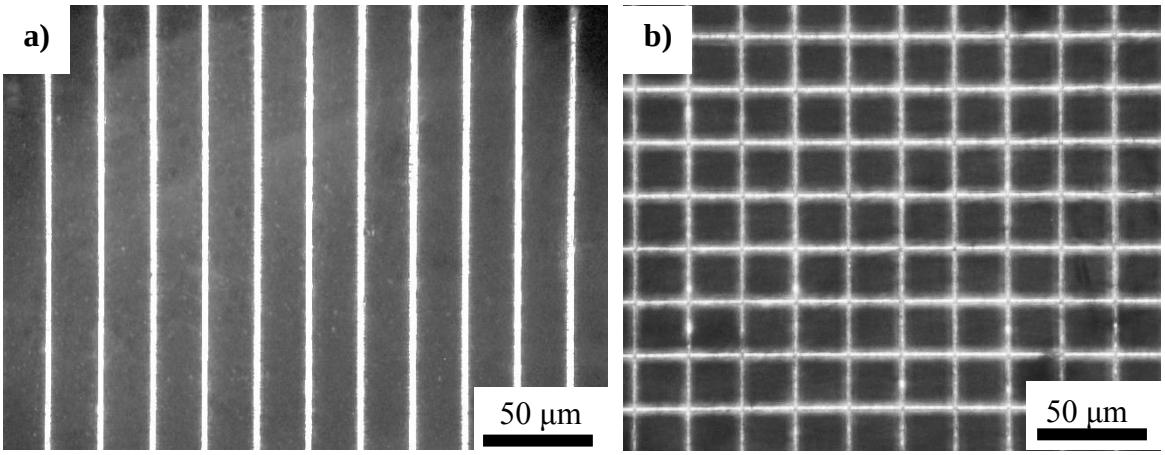

Figure 36 Optical microscope (back illumination) images of a a) 1D and b) 2D PC structures fabricated in thin aluminum film deposited on $YZ - LiNbO_3$ crystal. Structures period is $\Lambda = 25$ µm, line width $a \approx 1{,}5$ µm in both directions

Second harmonic was selected, because it can be focused to a smaller spot (compared to $\lambda = 1030$ nm). An objective with focal length of $f = 4$ mm

(NA $= 0{,}4$) was used to focus the $\lambda = 515$ nm radiation to a $a \approx 1{,}5$ µm spot. Pulse density was $P_D = 2000$ pulses/mm, the sample translation speed $v = 5$ mm/s and the energy density in focus $\phi = 0{,}73$ J/cm^2. Figure 37 shows the fabricated PC lines at X100 magnification: a) illumination from above, b) dark field regime. Dark field image reveals surface contamination – nanometer sized particles, which were generated and deposited on the metal layer surface during the 1D PC structure fabrication.

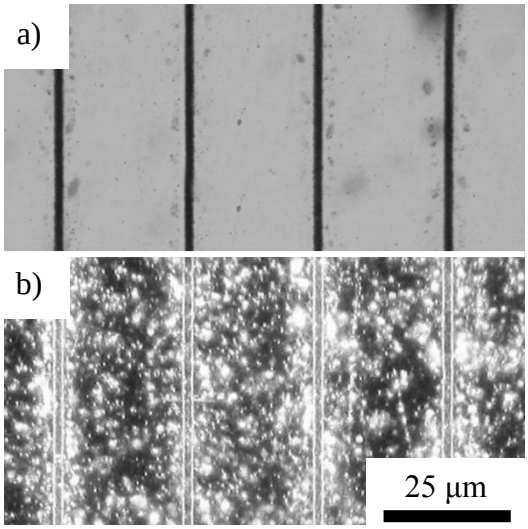

Figure 37 optical microscope images of several lines from a PC structure fabricated in a thin aluminum film deposited on a YZ − $LiNbO_3$ crystal at high magnification: a) lightening from above, b) dark field regime. Fabricated line width is $a = 1,5$ µm

The fabricated two-port SAW devices were tested by P. Každailis. SAW devices transmission characteristics were measured with the radio-frequency network analyzer E5062A (Agilent Technologies). The frequency dependences of transmission losses measured for free surface, 1D and 2D PC structures between the IDTs are shown in Figure 38. In the absence of a PC structure, the transmission loss at the IDT center frequency of $f = 68$ MHz is close to 14 dB. In the presence of the 1D structure, the sharp drop of 8 dB in the SAW transmission at $f = 68{,}2$ MHz is observed. The drop peak frequency is determined by the Bragg reflection condition [159]:

$$f_{\mathrm{B}} = v_{\mathrm{avg}}/2a \tag{22}$$

here v_{avg} is the average SAW velocity, and a is the structure period. The SAW velocity is averaged over the free and metallized surfaces as [159]:

$$v_{\mathrm{avg}}^{(1\mathrm{D})} = \frac{2r}{a} V_{\mathrm{m}} + \left(1 - \frac{2r}{a}\right) V_{\mathrm{f}} \tag{23}$$

here r is the half-width of the aluminum film strip, V_{f} and V_{m} are the SAW velocities on a free and metallized surface of the substrate, respectively. Their difference is caused by screening of the piezoelectric fields by the metal film and can be expressed as [160]:

$$\frac{V_{\mathrm{f}} - V_{\mathrm{m}}}{V_{\mathrm{f}}} = \frac{K^2}{2} \tag{24}$$

here K^2 is the electromechanical coupling constant of the substrate. The mass loading effect on the SAW velocity for a given thickness of aluminum film can be neglected. By substituting the values $V_{\mathrm{f}} = 3488\ \mathrm{m/s}$ and $K^2 = 4{,}6\%$ taken from literature [160] into eqs. (22)-(24) one obtains $f_{\mathrm{B}}^{(1\mathrm{D})} = 68{,}25$ MHz, which is in good agreement with the measured value.

With the 2D structure, a considerably stronger and wider drop was observed in the transmission characteristics. The average increase in transmission loss is about 25 dB in the band from $f = 68{,}25$ MHz up to $f = 68{,}95$ MHz. As seen, this band has a lower boundary coinciding with the frequency of the 1D peak, and its width is about $\Delta f = 0{,}7$ MHz. In the 2D case, the SAW velocity is averaged using the fractions of metallized and free areas as weighting functions [159]:

$$V_{\mathrm{avg}}^{(2D)} = \left(\frac{2r}{a}\right)^2 V_{\mathrm{m}} + \left(1 - \left(\frac{2r}{a}\right)^2\right) V_{\mathrm{f}} \tag{25}$$

Calculation with the same parameters as above yields the slightly higher resonance frequency of $f = 68{,}34$ MHz .It is, however, somewhat lower than the experimentally measured mid-band frequency value $f = 68{,}6$ MHz.

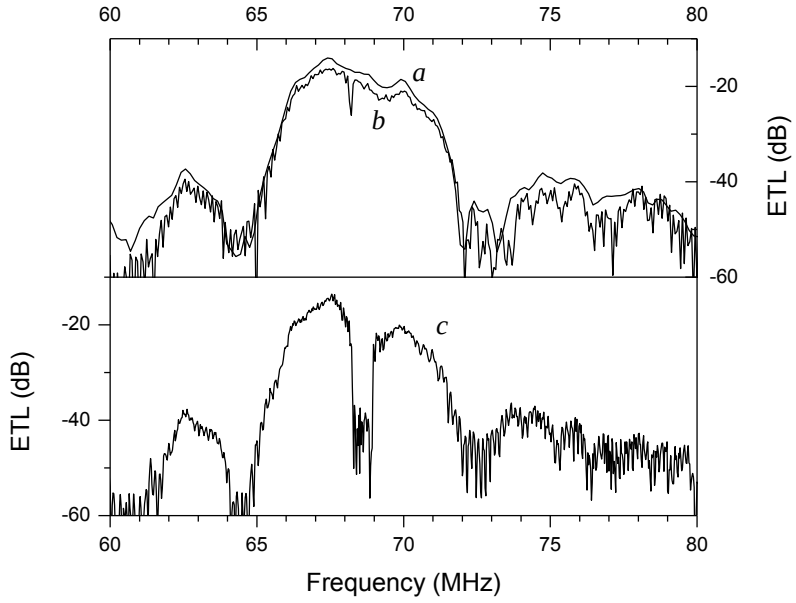

Figure 38 Effective transmission loss of laser fabricated two-port SAW device with free surface (a), 1D (b) and 2D (c) PC structures

To conclude, one-dimensional and two-dimensional SAW phononic crystal structures were fabricated on the YZ − $LiNbO_3$ crystal surface using FLM of a thin aluminum film [P5]. The 1D-structure exhibits a peak in the transmission loss at the frequency well described by the Bragg reflection model. The strong enhancement by 25 dB in the $\Delta f = 0{,}7$ MHz band of the transmission loss was observed in the 2D-structure. The measured frequency characteristics of the SAW transmission in the structures are in good agreement with theoretical estimations based on the SAW velocity averaged over the free and metallized surface of the piezoelectric substrate. The laser technology employed with a maximum resolution of $r = 0{,}5$ μm is shown to be very attractive for fabrication of phononic filters and other complex SAW devices. This technology offers an important advantage of versatile, flexible and multiplex fabrication of sophisticated SAW structures without a photo-lithographical process.

3.5. Fabricating photonic crystals for spatial light filtering

Photonic crystals (PC) are materials in which the refractive index is a periodic function of space. Modulation period is usually in the order of a wavelength [161]. PCs are widely studied mostly due to their peculiar temporal dispersion properties, in particular due to the band-gaps in the frequency domain [162,163]. Thus, we report the first experimental evidences of spatial filtering of light beams by a three-dimensional PC in the configuration displaying no angular bandgaps [164].

PCs for light filtering were fabricated by DLW in a glass bulk by periodically modifying the refraction index. Refractive index modification regime is described in chapter 1.5.2.1. PCs were fabricated by the 2.5D technique: starting the fabrication from the bottom layer and moving up - layer by layer.

The geometry of the PC is illustrated in Figure 39 here $d_{\perp} = 1{,}5$ μm and $d_{\parallel} = 10{,}6$ μm are the transverse and longitudinal periods respectively. Different colors of the ellipsoids indicate odd and even layers of the photonic crystal which are half-period shifted one with respect to another in transverse plane. The total number of the longitudinal modulation periods was 25 (50 fabricated 2D layers) and the matrix size in transverse plane was 500 by 500.

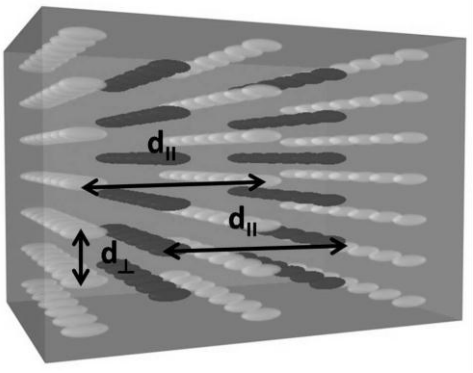

Figure 39 3D photonic crystal model. Parameters: longitudinal period $d_{\perp} = 1,5$ μm, transverse period $d_{\parallel} = 10,6$ μm

Each PC pixel was fabricated with a single femtosecond pulse, therefore 12500000 pulses must be distributed in glass bulk in order to fabricate such a PC . An aspheric lens with a focal length of $f = 4$ mm was used to fabricate the PC structures ~ 100 μm below glass surface. Figure 40 shows a hexagonal (HEX) type PC structure at x100 magnification. The PC fabrication process parameters are: wavelength $\lambda = 1030$ nm, pulse duration $\tau = 300$ fs, pulse repetition rate $f = 100$ kHz, average power $P = 28$ mW. Pulse energy was $E_{\mathrm{P}} = 280$ nJ and the energy density in waist was $\phi \approx 45\ \mathrm{J/cm^2}$. Volume of a modified refractive index region was less than $b = 1{,}5$ μm in transverse and $c = 5$ μm in longitudinal dimension.

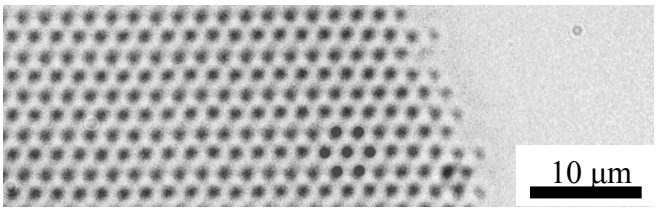

Figure 40 Optical microscope (phase contrast) image of a HEX type PC structure fabricated in glass bulk by FLM. Distance between pixels $a = 2$ μm

Fabricated PC had a circular shape in order to reduce the tensions in the glass bulk which occur during the fabrication of PC. Figure 41 shows glass bulk tensions (optical microscope photos made with crossed linear polarizers) in square and circular shaped PC structures. The square PC has the highest tensions in the edges which can lead to substrate breakdown.

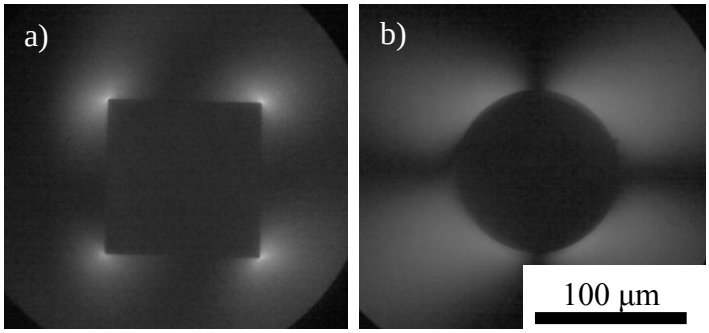

Figure 41 Optical microscope (crossed polarizers) images of PCs (100 μm diameter) fabricated in glass bulk by DLW. a) Shows tensions which occur in corners of square PC, b) in circle PC

By illuminating the fabricated PC with a continuous wave (CW) HeNe ($\lambda = 632$ nm, $P = 2$ mW) laser beam we observe the filtered areas in the angular distributions in the central maximum of the transmitted radiation (Figure 42). We interpret the observations by a theoretical and numerical analysis of the paraxial light propagation model. The experimental measurement shows the presence of the first diffraction maxima (Figure 42 a) as well as the dark line structure in the central maximum. The results are well reproducible and show the signatures of the expected effect of the spatial filtering. The configuration of the crossing dark lines shows the angular components of the spatial spectra which are filtered out. The structure of these dark lines within the central maximum corresponds well with the structure of the bright lines observed in the first diffraction maxima and are in a good correspondence with the theoretical expectations (discussed in [P1]).

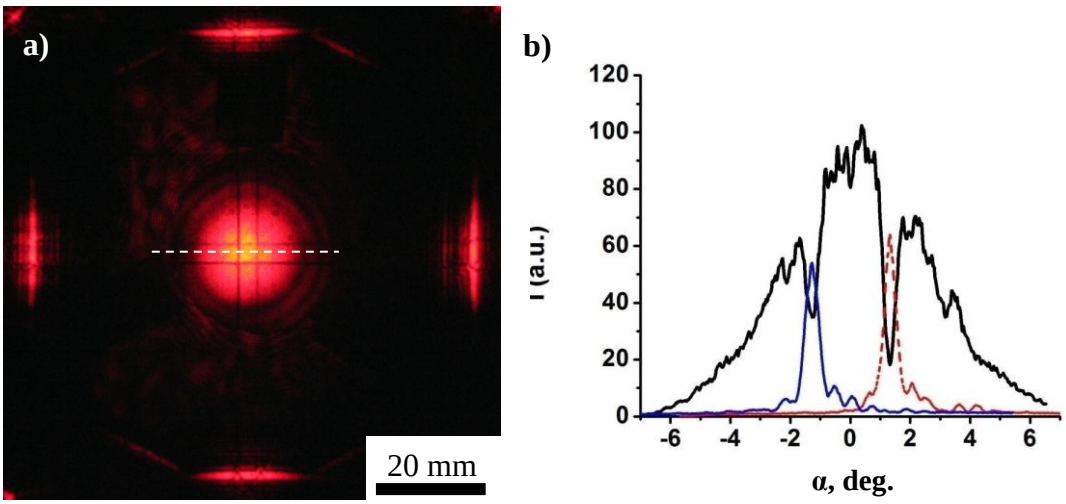

Figure 42 a) HeNe laser ($\lambda = 632$ nm) beam intensity distribution photo after PC in far field. b) Intensity distribution of filtered beam (dash line in a)) – red and blue lines represent filtered first diffraction maxima intensity distributions

In conclusion, we have experimentally proven for the first time the effect of the spatial filtering of light beams by a three-dimensional PC. Those evidences consist in the modification of the angular spectra of the propagating beams in such a way, that the particular angular components are removed from the zero

components, and are deflected into the first diffraction components. The theoretical analysis of Prof. K. Staliūnas and L. Maigytė reproduces well the experimental observations and interprets the observed effect as the spatial filtering in the gapless configuration. The reported effect of spatial filtering is relatively weak as the dark lines are relatively narrow, and carries a demonstrational character only. Just around approximately 5 % of the radiation was filtered out with the particular crystals. In order to obtain a technologically utile spatial filtering PCs with a higher index contrast are necessary, which could be based on new materials and new fabrication technologies. For example to obtain a relevant filtering by selectively removing 50% of intensity from the spatial spectra, the index modulation of order $\Delta n_0 = 3 \cdot 10^{-2}$ would be required for a PC with the same geometry.

3.6. Fabricating radial and azimuthal polarization converter

Axially symmetrical polarization states or cylindrical vector (CV) beams are becoming more and more attractive in various applications [169-177]. Spirally varying retarders based on segmented waveplate can convert linear polarization (high power laser radiation) to radial or azimuthal polarization [165]. The main disadvantage of such converters is segmentation. Devices to obtain CV beams with a continuous pattern were designed and fabricated for incident beams with linear or circular polarization [P3].

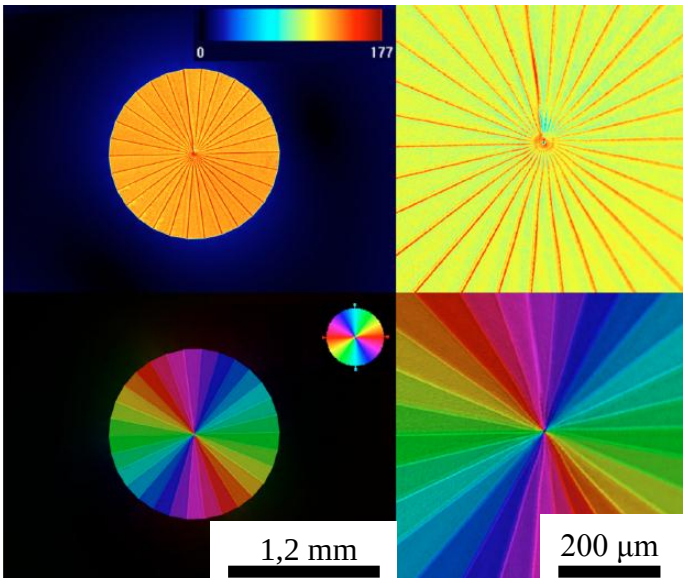

Figure 43 Special optical microscope images of polarization converters. The top images represent the retardance value distribution with 5X (left) and 20X (right) magnification of the structure. The bottom images represent the color-coded distribution of slow axis [P3]

For the incident linearly polarized beam, a half-wave plate with a continuously varying slow axis direction has to be constructed (Figure 46 b), which rotates the incident linear polarization by the angle necessary to produce a radial distribution of the electric field. For the incident circular-polarized beam, the radial or azimuthal polarization can be formed with a space variant quarter-wave plate possessing a radial symmetry (Figure 46 a). The advantage of the

quarter-wave plate based converter over the half-wave plate one is a considerably smaller retardance[3] value, $R = \Delta n d$ for a given induced birefringence Δn and length of structure d, which is needed for the polarization conversion, for example $R \approx 130\ nm$ for $\lambda = 532$ nm wavelength. The theory on induced retardance and self-assembled nanograting formation in fused silica bulk is described in chapter 1.5.2.2.

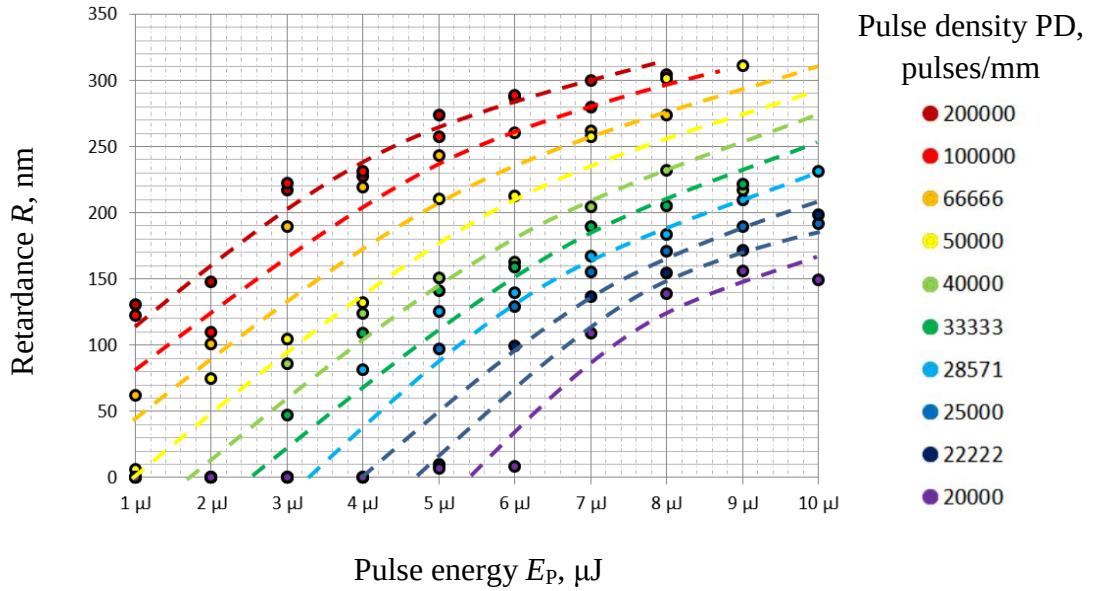

Figure 44. Dependence of induced retardance R on incident pulse density and pulse energy. Fabrication parameters: pulse duration $\tau = 300$ fs, pulse repetition rate $f = 200$ kHz, focusing lens focal length $f = 18$ mm

The experiments were performed using a Yb: KGW femtosecond laser system, operated at a wavelength of $\lambda = 1030$ nm with a pulse duration of $\tau = 270$ fs and repetition rates up to $f = 500$ kHz. A objective with relatively low numerical aperture of $NA = 0{,}35$ was chosen for the fabrication. In the experiments we achieved the retardance as high as $R = 260$ nm, which was sufficient for the fabrication of polarization converters working in the visible and near infrared. The optimum values for the pulse energy, repetition rate, and

[3] Retardance - the difference in phase shift between two characteristic polarizations of light.

writing speed required to achieve the desired quarter-wave retardance at $\lambda = 532$ nm wavelength, were found to be $E_P = 0{,}5$ J, $f = 200$ kHz, and $v = 1$ mm/s, respectively. The laser beam was focused to $z = 200$ µm below the surface of a $l = 2$ mm thick fused silica sample, which was mounted onto the XYZ linear air-bearing translation stage system. The stages were computer controlled via SCA software to move in a spiral trajectory with steps of $\Lambda = 1$ µm, enabling a complete scan to cover uniformly a circular area of $d =$ 1,2 mm diameter in about $t = 1{,}5$ h.

The laser beam polarization was manipulated by an achromatic half-wave plate mounted on a motorized rotation stage. By controlling the angle of the half-wave plate and the XY stage position, we could fabricate a space-variant quarter wave plate with the desired geometry of anisotropic modification distribution. Fabricated birefringent element was analyzed with a quantitative birefringence ABRIO measurement system (Hinds Instruments, Inc.) and Olympus BX51 optical microscope (Figure 43).

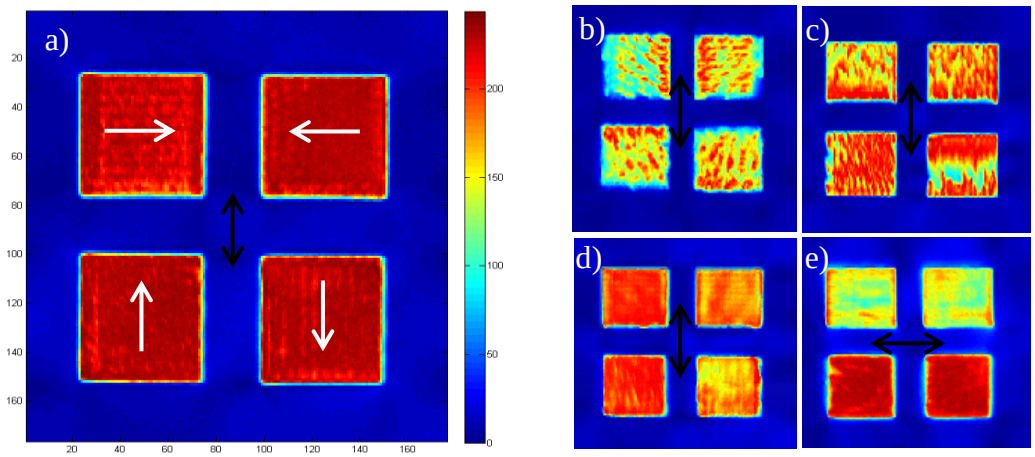

Figure 45 Induced birefringence measurements (ABRIO). a) 3 µJ, 100000 pulses/mm; b) 6 µJ, 100000 pulses/mm; c) 3 µJ, 66666 pulses/mm; d)6 µJ, 66666 p/mm; e)6 µJ, 66666 pulses/mm (polarization rotated by 90°). White arrows indicate fabrication scanning direction. Black arrows indicate incident polarization direction. Square size is 200 µm. Pulse duration $\tau = 300$ fs, repetition rate $f = 200$ kHz

Further experiments were done to check the dependence of the induced retardance on the incident pulse density and energy (Figure 44). The higher the pulse density and pulse energy the higher the retardance value that can be induced. However, the uniformity of the induced nano-grating (as well as retardance uniformity) cannot be achieved in the whole range of listed energies and pulse densities. Uniformity of induced structures depends on writing direction, polarization orientation and pulse duration [166]. Figure 45 shows squares of size $200\ \mu m$ fabricated at different energies with different density. White arrows indicate the fabrication scanning direction. Black arrows indicate incident polarization direction. With a pulse duration of $\tau = 300$ fs and pulse repetition rate $f = 200$ kHz, the highest structure writing uniformity (Figure 45 a) was achieved at $E_P = 3\ \mu J$ and a pulse density of $P_D = 100000$ pulses/mm. A maximum induced retardance of $R = 250$ nm is maintained.

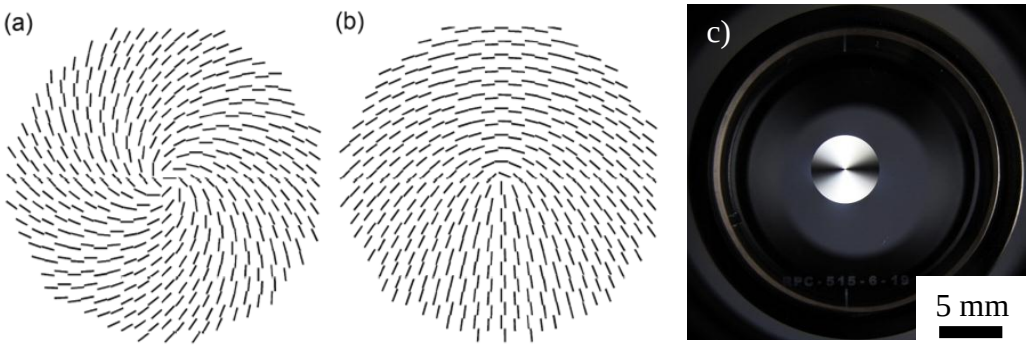

Figure 46 Schematic drawings of nanogratings distribution in quarter- (a) and half-wave (b) polarization converters [125]. c) Optical microscope (with crossed polarizers) photo of radial/azimuthal polarization converter fabricated inside bulk of fused silica glass. Converter diameter $d = 6$ mm, operating wavelength $\lambda = 515$ nm

Figure 46 c shows an optical microscope image (with crossed polarizers) of the radial/azimuthal polarization converter fabricated inside the bulk of a fused silica glass substrate. The converter diameter was $d = 6$ mm, operating wavelength $\lambda = 515$ nm. Such an element has a 100 times higher damage threshold $\phi_{1000-on-1} = 22.80 \pm 2.74\ J/cm^2$ (according to ISO 11254 – 2,

measured at $\lambda = 1064$ nm, $\tau = 3.5$ ns, $f = 10$ Hz), than a nematic liquid crystal polarization converter $\phi = 0{,}2$ J/cm^2 [167].

Figure 47 shows polarization converters array (converters diameter $d = 100$ μm) fabricated at different pulse durations and different pulse energies. Energy changes from $E_\mathrm{P} = 0{,}35$ μJ to $E_\mathrm{P} = 3{,}15$ μJ (in 350 nJ steps) and the pulse duration from $\tau = 350$ fs to $\tau = 1000$ fs (in 70 fs steps). Pulse repetition rate was $f = 200$ kHz and the pulse density $P_\mathrm{D} = 100000$ pulses/mm. It is clearly seen that to induce birefringence it is better to use longer pulses $\tau > 500$ fs. At $\tau \approx 580..720$ fs and pulse energies less than $E_\mathrm{P} < 1{,}8$ μJ the induced grating is most uniform (shown in Figure 47 dashed square). Recently it was reported that at $\tau = 700$ fs the induced grating period in fused silica is the smallest [166].

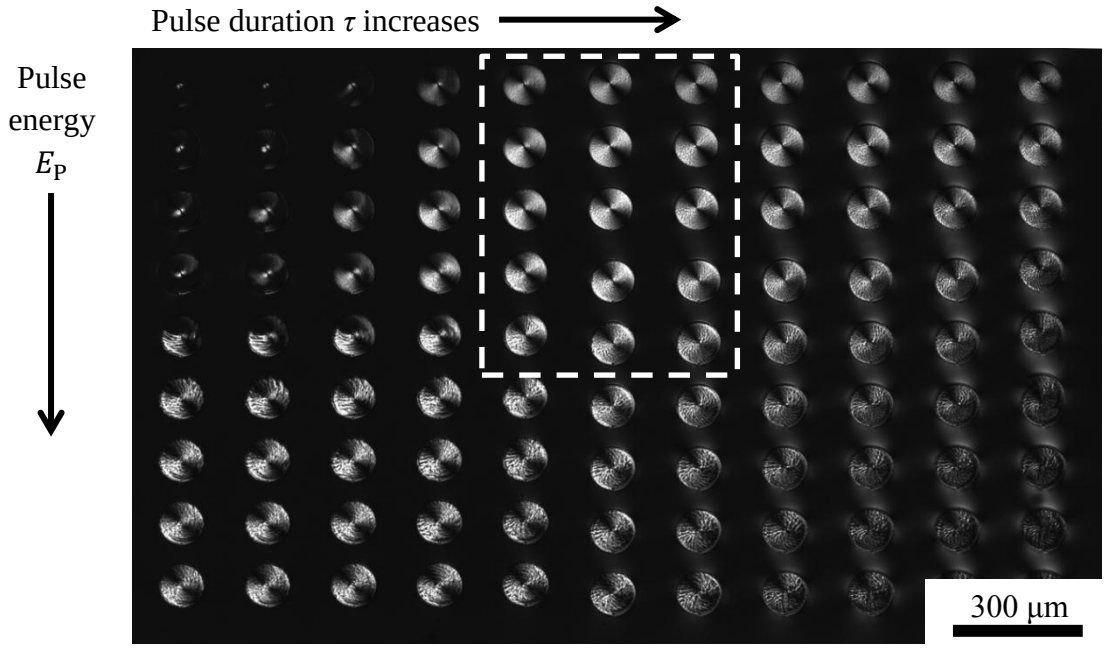

Figure 47 Diameter $d = 100$ μm polarization converters array fabricated at different pulse durations and different pulse energies. Energy changes from $E_\mathrm{P} = 0{,}35$ μJ to $E_\mathrm{P} = 3{,}15$ μJ (in 350 nJ steps) and pulse duration from $\tau = 350$ fs to $\tau = 1000$ fs (in 70 fs steps). Pulse repetition rate was $f = 200$ kHz, pulse density $P_\mathrm{D} = 100000$ pulses/mm. Dashed square shows most uniform structures

Figure 48 a shows a preview of the polarization converters fabrication trajectory (out of scale). Spiral pitch is $\Lambda = 1$ μm. In order to fabricate the pattern shown in Figure 46 b, the polarization rotation of the writing beam must be synchronized with the XY stages while moving in a spiral trajectory. Needed polarization orientation variation is shown in Figure 48 a. Figure 48 b shows the S-waveplate RPC-515-10-20 mounted converter, which has a diameter of $d = 10$ mm. It was fabricated for $\lambda = 515$ nm wavelength. Sample translation speed was $v = 2$ mm/s and the fabrication duration was $t = 11$ h. Fabrication speed is limited to f/P_{D} . Pulse density equal to $P_{\mathrm{D}} = 100000$ kHz is needed to induce an uniform structure with required retardance. The measured transmission of this element was $T = 50\%$ (remaining light is scattered by the structure). There are two orientation marks which indicate the required incident polarization orientation. If the incident polarization, or converter, is rotated by $\alpha = 90°$, the incident linear polarization will be converted to azimuthal polarization.

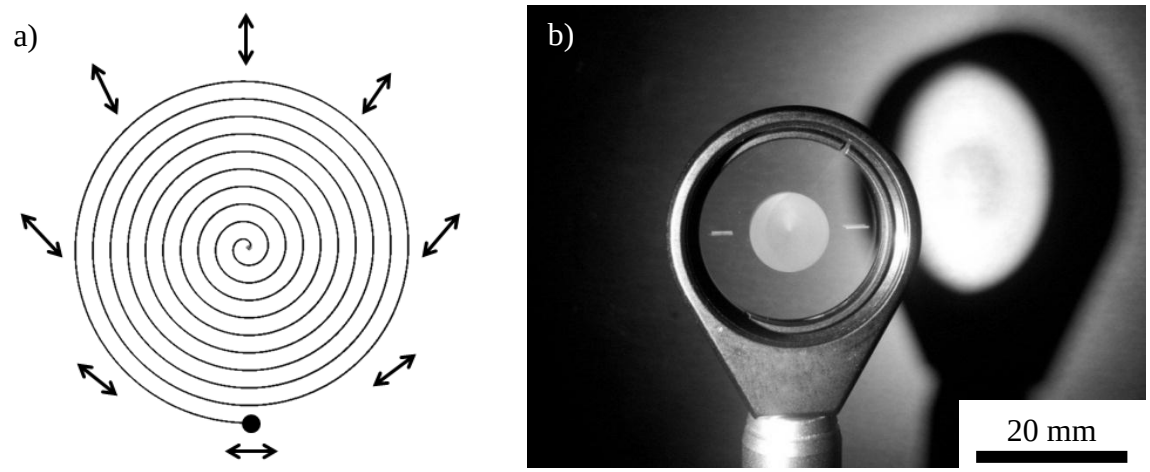

Figure 48 a) polarization converter fabrication trajectory preview (out of scale). Blue line indicates sample positioning trajectory, while black arrows indicate writing beam polarization orientation. b) $d = 10$ mm diameter polarization converter fabricated for $\lambda = 515$ nm wavelength. Sample translation speed $v = 2$ mm/s. Pulse density $P_{\mathrm{D}} = 100000$ pulses/mm

The intensity distributions are shown in Figure 49 for a) radial and d) azimuthal polarized beams at $\lambda = 1030$ nm wavelength measured with the

WinCamD camera (DataRay Inc.). Such a doughnut beam intensity distribution represents the TEM_{01*} mode. Figure 49 b) shows the radial polarization intensity distribution with a polarizer between converter and camera, c) radial with polarizer rotated by 90°, e) azimuthal polarization with polarizer between converter and camera, f) azimuthal polarization with polarizer rotated by 90°. Black arrows indicate the electromagnetic field orientation in the beam. Also, the radial polarization can be treated as $R-TEM_{01*}$ and the azimuthal as $A-TEM_{01*}$. Axially symmetric polarization mode TEM_{01*} results from a superposition of the two linearly polarized modes TEM_{01} and TEM_{10} only if their planes of polarization are perpendicular to each other and phase shift equals zero [168].

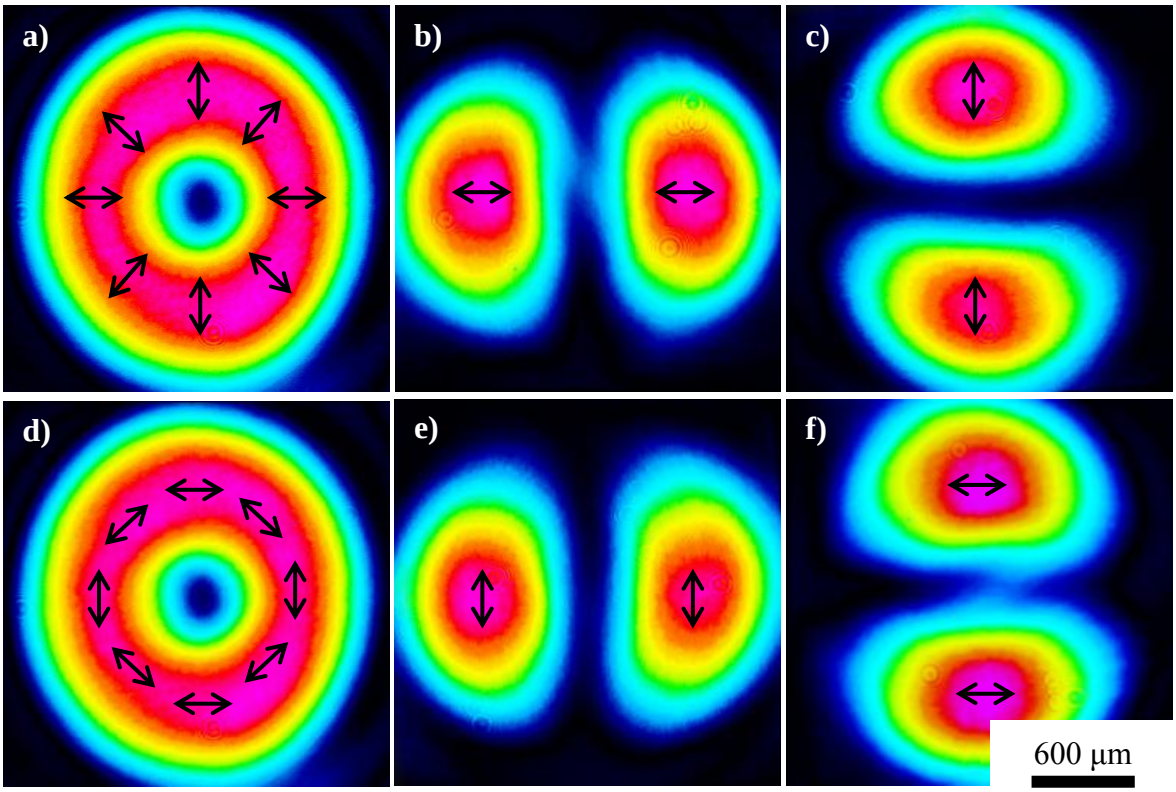

Figure 49 Radial and azimuthal polarization beams $\lambda = 1030$ nm intensity distribution measured with WinCamD camera (DataRay Inc.). a) radial with no polarizer, b) radial with polarizer between converter and camera, c) radial with polarizer rotated by 90°, d) azimuthal with no polarizer, e) azimuthal with polarizer between converter and camera, f) azimuthal with polarizer rotated by 90°. Black arrows indicate electromagnetic field orientation in the beam

Finally, there is an increasing interest in the axially symmetrical polarization modes. Such beams have attracted recently a significant attention largely because of their unique focusing properties under high numerical aperture ($NA > 0{,}8$). Numerical calculations done by Quabis et al. shows that tighter focus spots can be obtained using radial polarization, caused by strong and localized longitudinal field component [169]. This effect has been experimentally confirmed by several groups [170,171] and has already found applications in high resolution imaging such as confocal microscopy, two-photon microscopy, second harmonic generation microscopy [172], third-harmonic generation microscopy [173], and dark field imaging [174]. In tip-enhanced near-field optical microscopy, besides providing high spatial resolution, the radially symmetric field distribution at the tip allows the 3D orientation of the transition dipole moment to be visualized [175]. Radial polarization is also ideally suitable for the surface plasmon excitation with axially symmetric metal/dielectric structures [176], because the plasmon excitation is strongly dependent on the excitation polarization. The large longitudinal electric fields generated with radially polarized beams are also explored for particle acceleration [177]. The discussions of these very interesting topics are beyond the scope of this thesis. Nevertheless, it is safe to conclude that with simple and efficient generation methods becoming more and more accessible, this field will grow further, and the list of applications of CV beams will continue to expand rapidly [178].

Conclusions

- The prototype femtoLAB femtosecond laser micromachining system was created. It integrates a Yb:KGW femtosecond laser, second, third and fourth harmonics generators, four motorized attenuators, four motorized polarization rotators, galvanometer scanners, power meter, spatial light modulator, machine vision, autofocus and precise XYZ object positioning.
- It was shown that selective ablation of thin (~200 nm) chromium layer from a silica glass substrates using $\tau = 300$ fs duration, $\lambda = 1030$ nm wavelength light pulses enables the fabrication of binary holograms which can generate femtosecond optical vortex beams (different topological charge $m = 1,\ m = 2,\ m = 3,\ m = 5,\ m = 10,\ m = 25$) with diffraction efficiency of $\eta = 4{,}63\ \%$ to first diffraction maxima.
- It was shown that selective ablation of thin (~300 nm) aluminum layers from lithium niobate ($LiNbO_3$) crystal surface using $\tau = 300$ fs duration, $\lambda = 1030$ nm wavelength light pulses enables the fabrication of interdigital transducers with a center frequency of $f = 68$ MHz and acoustic wavelength of $\lambda = 50$ μm.
- It was shown that selective ablation of thin (~300 nm) aluminum layers from a lithium niobate ($LiNbO_3$) crystal surface using $\tau = 300$ fs duration, $\lambda = 515$ nm wavelength light pulses enables 1D and 2D phononic crystals fabrication with a period of $\Lambda = 25$ μm. Fabricated 2D PC modifies the transmission loss characteristics of an interdigital transducers system by 25 dB at $f = 68{,}6$ MHz.
- It was shown that induced refractive index change inside glass bulk with light pulse duration of $\tau = 300$ fs and wavelength of $\lambda = 1030$ nm enables the fabrication 3D photonic crystals for spatial beams filtering with 5 % filtering efficiency.

- It was shown that self-assembled nanogratings, induced inside fused silica glass bulk by light pulses of $\tau = 700$ fs duration, $\lambda = 1030$ nm wavelength enables the fabrication of an uniform polarization converter capable of converting $\lambda = 515$ nm linear polarization to radial or azimuthal polarization with an efficiency of $\eta = 50\%$.
- It was shown that vortex beam ($m = 10$) with a pulse duration of $\tau = 300$ fs and $\lambda = 515$ nm wavelength enable the fabrication of hollow micro-tube structures ($d = 10$ μm diameter, $h = 60$ μm height) in SZ2080 photopolymer using multiphoton polymerization technique. The fabrication time of one micro-tube with the 60 μm height and the 3 μm inner radius by using the OV method is 500 times shorter than by the DLW method and 1,25 times shorter than using the holographic method.

Bibliography

1. T .H. Maiman, “Stimulated Optical Radiation in Ruby”, Nature **187**, 493–494 (1960).

2. N. H. Rizvi, “Femtosecond laser micromachining: Current status and applications”, RIKEN REVIEW, ISSU **50**, 107–112 (2003).

3. R. R. Gattass, E. Mazur, “Femtosecond laser micromachining in transparent materials”, Nature Photonics **2**, 219–225 (2008).

4. D. Du, X. Liu, G. Korn, J. Squier, G. Mourou, “ Laser-induced breakdown by impact ionization in SiO2 with pulse widths from 7 ns to 150 fs”, Appl. Phys. Lett. **64**, 3071–3073 (1994).

5. A. P. Joglekar et al. “A study of the deterministic character of optical damage by femtosecond laser pulses and applications to nanomachining”, Appl. Phys. B **77**, 25–30 (2003).

6. B. C. Stuart, M.D. Feit, A. M. Rubenchik, B. W. Shore, and M. D. Perry, “Laser-induced damage in dielectrics with nanosecond to subpicosecond pulses,” Phys. Rev. Lett. **74**, 2248 (1995).

7. F.X. Kartner, U. Morgner, R. Ell, E. P. Ippen, J. G. Fujimoto, V. Scheuer, G. Angelow, T. Tschudi, “Few-cycle-pulse generation and its applications”, The 4th Pacific Rim Conference on Lasers and Electro-Optics **1**, 606–607 (2001).

8. S. Backus, C. G. Durfee, M. M. Murnane, H. C. Kapteyn, “High power ultrafast lasers”, Rev. Sci. Instrum. **69**, 1207 (1998).

9. K. Venkatakrishnan, B. Tan, P. Stanley, L. E. N. Lim, B. K. A. Ngoi, "Femtosecond pulsed laser direct writing system", Opt. Eng. **41**, 1441 (2002).

10. A. Zoubir, M. Richardson, C. Lopez, L. Petit, K. A. Richardson, C. Rivero and A. Schulte, "Femtosecond direct-writing of waveguide in non-oxide glasses", Proc. SPIE **5339**, 175 (2004).

11. D. Bäuerle, “Laser Processing and Chemistry”, Springer: D. Media 3rd Rev.E, 788 (2011).

12. P. P. Pronko, S. K. Dutta, J. Squier, J. V. Rudd, D. Du, and G. Mourou, “Machining of sub-micron holes using femtosecond laser at 800 nm”, Opt. Commun. **114**, 106–110 (1995).

13. S. Nolte, B. N. Chichkov, H. Welling, Y. Shani, K. Lieberman, and H. Terkel, “Nanostructuring with spatially localized femtosecond laser pulses”, Opt. Lett., **24**, 914–916 (1999).

14. P. Kazansky, "Ultrafast Laser Writing in Transparent Materials: From Physics to Applications," CLEO, Optical Society of America, CTU1J.1 (2012).

15. D. N. Wang, “Micro-engineered Optical Fiber Sensors Fabricated by Femtosecond Laser Micromachining”, Optical Sensors, OSA Technical Digest, Optical Society of America, STu4F.1 (2012).

16. J. E. Carey III, “Femtosecond-laser Microstructuring of Silicon for Novel Optoelectronic Devices”, PhD Thesis, Harvard University, Cambridge, Massachusetts (2004).

17. M. Stubenrauch, M. Fischer, C. Kremin, S. Stoebenau, A. Albrecht and O. Nagel, “ Black silicon—new functionalities in microsystems”, J. Micromech. Microeng.**16**, 82–87 (2006).

18. R. Buividas, L. Rosa, S. Juodkazis, “Gold coated ripple-patterned SiC substrates for SERS”, Engineering **96** (5), 57404–57404 (2006).

19. K. Lieberman, Y. Shani, I. Melnik, S. Yoffe, Y. Sharon, “Near-field optical photomask repair with a femtosecond laser”, J. Microsc. **194**, 537–541 (1999).

20. H. W. Choi, D. F. Farson, J. Bovatsek, A. Arai, and D. Ashkenasi, “Direct-write patterning of indium-tin-oxide film by high pulse repetition frequency femtosecond laser ablation”, Appl. Opt. **46** (23), 5792–5799 (2007).

21. M. Xia, Y. Tu, "An Investigation of Femtosecond Laser Micromachining", MEMS, NANO and Smart Systems, ICMENS’05 Proc. 296–300 (2005).

22. H. Y. Zheng, A. R. Zareena and H. Huang, “Femtosecond Laser Processing of Nitinol”, STR/03/028/MT (2004).

23. Thick-Walled Nitinol. Available at: http://www.raydiance.com/resource-center/material-library/ [Accessed 2012.06.17].

24. K. M. Davis, K. Miura, N. Sugimoto, K. Hirao, "Writing waveguides in glass with a femtosecond laser," Opt. Lett. **21**, 1729–1731 (1996).

25. Ph. Bado, A. A. Said, M. Dugan, T. S. Sosnowski, S. Wright, “Dramatic improvements in waveguide manufacturing with femtosecond lasers”, technical proc., NFOEC, 1153–1158 (2002).

26. I. Sohn, M. Lee, J. Woo, S. Lee, and J. Chung, "Fabrication of photonic devices directly written within glass using a femtosecond laser," Opt. Express **13**, 4224–4229 (2005).

27. I. Sohn, M. Lee, J. Chung , "Fabrication of optical splitter and passive alignment technique with a femtosecond laser," Photonics Technology Letters, IEEE **17**(11), 2349–2351 (2005).

28. A. M. Streltsov, N. F. Borrelli, “Fabrication and analysis of a directional coupler written in glass by nanojoule femtosecond laser pulses”, opt. Lett. **26**, 42–43, (2001).

29. C. Zhan, J. Lee, S. Yin, P. Ruffin, J. Grant, "Photoenhanced polarization mode separated fiber Bragg gratings inscribed by femtosecond laser", Journal of Appl. Phys. **101** (5), 053110–053110-7 (2007).

30. A. Stefani, M. Stecher, G. E. Town, O. Bang, "Direct Writing of Fiber Bragg Grating in Microstructured Polymer Optical Fiber," Photonics Technology Letters, IEEE **24 (**13), 1148–1150 (2012).

31. Y. Sikorski et al., “Optical waveguide amplifier in Nd-doped glass written with near-IR femtosecond laser pulses” Electron. Lett. **36**, 226–227 (2000).

32. G. Cohoon, R. Norwood, K. Tada, K. Kieu, and M. Mansuripur, "Fabrication of High-Q Microresonators using Femtosecond Laser Micromachining," in CLEO: Science and Innovations, Optical Society of America, CM1M.6 (2012).

33. M. Gecevičius, M. Beresna and P. G. Kazansky “5-dimentional optical recording with ultrashort light pulses”, 54th Scientific conference for young students of physics and natural sciences, Open Readings 2011, Vilnius, Lithuania, (2011).

34. M. Ventura, M. Straub and M. Gu. “Void-channel microstructures in resin solids as an efficient way to photonic crystals”, App. Phys. Lett., **82**, 1649–1651 (2003).

35. A. D. Goater, J. P. H. Burt, D. J. Morris, A.Menachery, N. H. Rizvi, D. R. Matthews, H. D. Summers, “Laser micromachining of optical biochips”, Proc. SPIE **6459**, 645909 (2007).

36. R. Daw and J. Finkelstein, “Introduction lab on a chip", Nature **442**, 367 (2006).

37. H.-B. Sun and S. Kawata, “Two-photon laser precision microfabrication and its applications to micro-nano devices and systems," J. Lightwave Technol. **21** (3), 624–633 (2003).

38. M. Malinauskas, A. Zukauskas, K. Belazaras, K.Tikuisis, V. Purlys, R. Gadonas and A. Piskarskas, “Laser fabrication of various polymer micro-optical components”, The Eur. Phys. J Appl. phys. **58**, 20501 (2011).

39. Y. Bellouard, A. Said, M. Dugan, P. Bado, “Fabrication of high-aspect ratio, micro-fluidic channels and tunnels using femtosecond laser pulses and chemical etching”, opt. Express **12**, 2120–2129 (2004).

40. Y. Kondo, J. Qiu, T. Mitsuyu, K. Hirao, T. Yoko, “Three-dimensional microdrilling of glass by multiphoton process and chemical etching”, Jpn J. Appl. Phys. **38**, 1146–1148 (1999).

41. M. Vengris, E. Gabryte, A. Aleknavicius, M. Barkauskas, O. Ruksenas, A. Vaiceliunaite, R. Danielius, “Corneal shaping and ablation of transparent media by femtosecond pulses in deep ultraviolet range”, J of cataract and refractive surgery **36 (**9), 1579–1587 (2010).

42. M. Malinauskas, P. Danilevicius, D. Baltriukiene, M. Rutkauskas, A. Žukauskas, Ž. Kairytė, G. Bičkauskaitė, V. Purlys, D. Paipulas, V. Bukelskienė, R. Gadonas, 3D artificial polymeric scaffolds for stem cell growth fabricated by femtosecond laser. Lith. J. Phys. **50**(1), 75–82 (2010).

43. R. Osellame, "Biophotonic chips fabricated by femtosecond laser micromachining," IEEE Photonics Society, 2010 23rd Annual Meeting, 536–537 (2010).

44. S. Siewert, C. Schultze, W. Schmidt, U. Hinze, B. Chichkov, A. Wree, K. Sternberg, R. Allemann, R. Guthoff and K. P.Schmitz, “Development of a micro-mechanical valve in a novel glaucoma implant”, Biomedical Microdevices, 1–14 (2012).

45. J.C.Maxwell, “A dynamical theory of the electromagnetic field”, Philosophical Transactions of the Royal Society of London, **155**, 459–512 (1865).

46. R. Gattass, “Femtosecond-laser interactions with transparent materials: applications in micromachining and supercontinuum generation”, PhD Thesis, Harvard University, Cambridge, Massachusetts (2006).

47. R. Osellame, G.Cerullo and R.Ramponi, “Femtosecond Laser Micromachining Photonic and Microfluidic Devices in Transparent Materials”, ISBN 978-3-642-23365-4, 4–5 (2012).

48. L.V. Keldysh, “Ionization in the field of a strong electromagnetic wave”, Soviet Physics JETP **20**, 1307 (1965).

49. S.Chris, N.Nozomi, G.Eli, K.Albert, and M.Eric, “Dynamics of femtosecond laser-induced breakdown in water from femtoseconds to microseconds”, Opt. Express **10**, 196–203 (2002).

50. M. Ams, G. D. Marshall, P. Dekker, M. Dubov, V. K. Mezentsev, I. Bennion, M. J. Withford, “Investigation of Ultrafast Laser-Photonic Material Interactions: Challenges for Directly Written Glass Photonics”, Selected Topics in Quantum Electronics, IEEE Journal of **14** (5), 1370–1381 (2008).

51. M. S. Giridhar, K. Seong, A. Schülzgen, P. Khulbe, N. Peyghambarian, M. Mansuripur, “Femtosecond Pulsed Laser Micromachining of Glass Substrates with Application to Microfluidic Devices”, Appl. Opt. **43** (23), 4584–4589 (2004).

52. C. B. Schaffer, "Interaction of femtosecond laser pulses with transparent materials," PhD Thesis, Harvard University (2001).

53. G. Gamaly, A. V. Rode, B. Luther-Davies, V. T. Tikhonchuk, “Ablation of solids by femtosecond lasers: Ablation mechanism and ablation thresholds for metals and dielectrics”, Phys. Plasmas **9**, 949 (2002).

54. L. Cerami, E. Mazur, S. Nolte, C. B. Schaffer, “Femtosecond laser micromachining”, in Ultrafast Optics, 3 (2007).

55. N. M. Bulgakova, V. P. Zhukov, A. Y. Vorobyev and C.Guo, “Modeling of residual thermal effect in femtosecond laser ablation of metals: role of a gas environment”, Appl. Phys. A **92** (4), 883–889 (2008).

56. S. E. Black, “Laser ablation: Effects and applications”. Hauppauge, N.Y: Nova Science Publishers, 8 (2011).

57. An-C. Tien, S. Backus, H. Kapteyn, M. Murnane, G. Mourou, ”Short-Pulse Laser Damage in Transparent Materials as a Function of Pulse Duration”, Phys. Rev. Lett. **82** (19), 3883–3886 (1999).

58. B. N. Chichkov, C. Momma, S. Nolte, F. von Alvensleben and A. Tünnermann, “Femtosecond, picosecond and nanosecond laser ablation of solids”, Appl.Phys. A: Materials Science & Processing **63 (**2), 109–115 (1996).

59. B. C. Stuart, M. D. Feit, A. M. Rubenchik, B. W. Shore, and M. D. Perry, “Laser-Induced Damage in Dielectrics with Nanosecond to Subpicosecond Pulses”, Phys. Rev. Lett. **74**, 2248–2251 (1995).

60. Y. Kozawa, S. Sato, “Generation of a radially polarized laser beam by use of a conical Brewster prism”, Opt. Lett. **30** (22), 3063–3065 (2005).

61. R. Hongwen, L. Yi-Hsin, W. Shin-Tson, “Linear to axial or radial polarization conversion using a liquid crystal gel”, Appl. Phys. Lett. **89 (**5), 051114–051114-3 (2006).

62. M. Stalder, M. Schadt, "Linearly polarized light with axial symmetry generated by liquid-crystal polarization converters," Opt. Lett. **21**, 1948 (1996).

63. P. B. Phua, W. J. Lai, Y. L. Lim, B. S. Tan, R. F. Wu, K. S. Lai, H.W.Tan, “High power radial polarization conversion using photonic crystal segmented half-wave-plate”, Lasers and Electro-Optics, CLEO/QELS (2008).

64. R. Oron, S. Blit, N. Davidson, A. Friesem, Z. Bomzon, E. Hasman, “The formation of laser beams with pure azimuthal or radial polarization”, Appl. Phys. Lett. **77** (21), 3322–3324 (2000).

65. D. J. Armstrong, M. C. Phillips, A. V. Smith, “Generation of Radially Polarized Beams with an Image-Rotating Resonator”, Appl. Optics, **42** (18), 3550–3554 (2003).

66. O. J. Allegre, W. Perrie, K. Bauchert, D. Liu, S. P. Edwardson, G. Dearden and K. G. Watkins, “Real-time control of polarisation in ultra-short-pulse laser micro-machining”, Appl. Phys. A: Materials Science & Processing **107 (**2), 445–454 (2012).

67. J. B. Ashcom, “The role of focusing in the interaction of femtosecond laser”, PhD thesis, Harvard University, Cambridge, Massachusetts, 3 (2003).

68. A. E. Siegman, “Lasers”, University Science Books, 664–669 (1986).

69. S. E. Black, “Laser ablation: Effects and applications”. Hauppauge, N.Y: Nova Science Publishers (2011).

70. B. Wolff-Rottke, J. Ihlemann, H. Schmidt, and A. Scholl, “Influence of the laser-spot diameter on photo-ablation rates”, Appl. Phys. A **60** (1), 13–17 (1995).

71. S. Maruo, O. Nakamura, and S. Kawata, "Three-dimensional microfabrication with two-photon-absorbed photopolymerization," Opt. Lett. **22**, 132–134 (1997).

72. J. Fischer and M. Wegener, "Three-dimensional direct laser writing inspired by stimulated-emission-depletion microscopy," Opt. Mater. Expr. **1**, 614–624 (2011).

73. K. M. Davis, K. Miura, N. Sugimoto, and K. Hirao, “Writing waveguides in glass with a femtosecond laser,” Opt. Lett. **21**(21), 1729–1731 (1996).

74. E. Glezer, M. Milosavljevic, L. Huang, R. Finlay, T. Her, J. Callan, and E. Mazur, "Three-dimensional optical storage inside transparent materials," Opt. Lett. **21**, 2023–2025 (1996).

75. J. Wang, H. Niino and A. Yabe, “One-step microfabrication of fused silica by laser ablation of an organic solution”, Appl. Phys. A **68** (1), 111–113 (1999).

76. K. Zimmer, R. Bohme, D. Hirsch and B. Rauschenbach, “Backside etching of fused silica with UV laser pulses using mercury”, J. Phys. D: Appl. Phys. **39**, 4651–4655 (2006).

77. R. Bohme, S. Pissadakis, M. Ehrhardt, D. Ruthe and K. Zimmer, “Ultra-short laser processing of transparent material at the interface to liquid”, J. Phys. D **39**, 1398–1404 (2006).

78. J. J. J. Kaakkunen, M. Silvennoinen, K. Paivasaari, P. Vahimaa, “Water-Assisted Femtosecond Laser Pulse Ablation of High Aspect Ratio Holes”, Phys. Proc. **12** (B), 89–93 (2011).

79. I. B. Sohn, Y. Kim, and Y. C. Noh, “Microstructuring of Optical Fibers Using a Femtosecond Laser”, J. Opt. Soc. of Korea, **13** (1), 33–36 (2009).

80. D. J. Hwang, T. Y. Choi, C.P. Grigoropoulos, “Liquid-assisted femtosecond laser drilling of straight and three-dimensional microchannels in glass”, Appl. Phys. A **79** (3), 605–612 (2004).

81. Laser Induced Backside Wet Etching (LIBWE): project completed. Available at: http://materials.web.psi.ch/Research/Structuring/LIBWE.htm [Accessed 2012.06.06].

82. B. Hopp, Cs. Vass , T. Smausz, "Laser induced backside dry etching of transparent materials", Appl. Surf. Sci. **253**, 7922–7925 (2007).

83. I. Zergioti, S. Mailis, N.A. Vainos, P. Papakonstantinou, C. Kalpouzos, C.P. Grigoropoulos and C. Fotakis, "Microdeposition of metal and oxide structures using ultrashort laser pulses", Appl. Phys. A **66** (5), 579–582 (1998).

84. I. Zergioti, D. G. Papazoglou, A. Karaiskou, N. A. Vainos, C. Fotakis, "Laser microprinting of InOx active optical structures and time resolved imaging of the transfer process", Appl. Surf. Sci., **197**, 868–872 (2002).

85. D. P. Banks, C. Grivas, J. D. Mills, R. W. Eason, I. Zergioti, "Nanodroplets deposited in microarrays by femtosecond Ti:sapphire laser-induced forward transfer", Appl. Phys. Lett. **89** (19), 193107–193107-3 (2006).

86. D. Banks, C. Grivas, J. Mills, I. Zergioti, R. Eason, "Nanodroplets de posited in microarrays by ferntosecond Ti:sapphire laser induced forward transfer", Appl. Phys. Lett. **89**, 193107–1 (2006).

87. A. Karaiskou, I. Zergioti, C. Fotakis, M. Kapsetaki, D. Kafetzopoulos, "Microfabrication of hiornaterials by the sub-ps laser-induced forward transfer process" Appl. Surf. Sci. **208**–**209,** 245–249 (2003).

88. D. Banks, C. Orivas, I. Zergioti, R. Eason, Ballistic "Laser-assisted solid transfer (blast) from a thin film precursor", Opt. Exp. **16**, 3249–3254.1 (2008).

89. D. Papazoglou, A. Karaiskou, I. Zergioti, C. Fotakis, "Shadowgraphic imaging of the sub-ps laser-induced forward transfer process", Appl. Phys. Lett. **81**(9), 1594–1596 (2002).

90. D. P. Banks, K. S. Kaur, C. Grivas, R. W. Eason, "Femtosecond laser-induced solid etching (LISE) of silicon and silic", EMRS Spring Meeting, Strasbourg, France (2009).

91. D. P. Banks, K. S. Kaur, C. Grivas, and R. W. Eason, "Femtosecond laser-induced solid etching (LISE) of silicon and silica" EMRS Spring Meeting (2009).

92. K. Venkatakrishnan, P. Stanley and L. E. N. Lim, “Femtosecond laser ablation of thin films for the fabrication of binary photomasks”, J. Micromech. Microeng. **12**, 775 (2002).

93. M. H. Liang, Y. J. Yi, L. Bo, M. G. Hong, “Phase transformation and nanograting structure on TiO2 rutile single crystal induced by infrared femtosecond laser”, Chinese Phys. **16**, 3328 (2007).

94. H. L. Ma, Y. Guo, M. J. Zhong and R. X. Li, “Femtosecond pulse laser-induced self-organized nanogratings on the surface of a ZnSe crystal”, Appl. Phys. A **89** (3), 707–709 (2007).

95. Z. Min-Jian “Femtosecond pulse laser-induced self-organized nanostructures on the surface of ZnO crystal”, Chinese Phys. B **17**, 1223 (2008).

96. E. M. Hsu, T. H. R. Crawford, C. Maunders, G. A. Botton, and H. K. Haugen, “Cross-sectional study of periodic surface structures on gallium phosphide induced by ultrashort laser pulse irradiation”, Appl. Phys. Lett. **92**, 221112, (2008).

97. G. Seifert, M. Kaempfe, F. Syrowatka, C. Harnagea, D. Hesse and H. Graener, “Self-organized structure formation on the bottom of femtosecond laser ablation craters in glass”, Appl. Phys. A **81**(4), 799–803, (2005).

98.Y. Han, S. Qu, “Uniform self-organized grating fabricated by single femtosecond laser on dense flint (ZF6) glass”, Appl. Phys. A. **98** (1), 167–170 (2010).

99. Y. Han, X. Zhao, and S. Qu, “Polarization dependent ripples induced by femtosecond laser on dense flint (ZF_6) glass”, Optics Express **19** (20), 19150–19155 (2011).

100. T. Tomita, K. Kinoshita, S. Matsuo and S. Hashimoto, “Effect of surface roughening on femtosecond laser-induced ripple Structures”, Appl. Phys. Lett. **90**, 153115, (2007).

101. R. A. Ganeev, M . Baba, T . Ozaki and H . Kuroda, “Long- and short-period nanostructure formation on semiconductor surfaces at different ambient conditions”, J. Opt. Soc. Am. B **27**, 1077–82 (2010).

102. C .Wang, H .Huo, M .Johnson, M .Shen and E. Mazur, “The thresholds of surface nano-/micro-morphology modifications with femtosecond laser pulse irradiations”, Nanotech. **21**, 75304 (2010).

103. V. R. Bhardwaj, E. Simova, P. P. Rajeev, C. Hnatovsky, R. S. Taylor, D. M. Rayner, and P. B. Corkum1, “Optically Produced Arrays of Planar Nanostructures inside Fused Silica”, Phys. Rev. Lett. **96**, 057404 (2006).

104. R. Buividas, L. Rosa, R. Šliupas, T. Kudrius, G. Šlekys, V. Datsyuk, and S. Juodkazis,” Mechanism of fine ripple formation on surfaces of (semi)transparent materials via a half-wavelength cavity feedback”, Nanotech. **22**, 055304, (2011).

105. G. Miyaji, K. Miyazaki, K. Zhang, T. Yoshifuji, and J. Fujita, "Mechanism of femtosecond-laser-induced periodic nanostructure formation on crystalline silicon surface immersed in water," Opt. Express **20**, 14848–14856 (2012).

106. X.D. Guo, R.X. Li, Y. Hang, Z.Z. Xu, B.K. Yu, H.L. Ma, B. Lu, X.W. Sun, “Femtosecond laser-induced periodic surface structure on ZnO”, Mat. Lett. **62 (**12–13), 1769–1771 (2008).

107. B. Dusser, Z. Sagan, A. Foucou, M. Jourlin, E. Audouard, “News applications in authentication and traceability using ultrafast laser marking”, Proc. SPIE **7201**, 72010V–72010V-8 (2009).

108. H. L. Chen, K. T. Huang, C. H. Lin, W. Y. Wang, and W. Fan, “Fabrication of sub-wavelength antireflective structures in solar cells by utilizing modified illumination and defocus techniques in optical lithography,” Microelectron. Eng. **84**(5-8), 750–754 (2007).

109. L. P. Ramirez, M. Heinrich, S. Richter, F. Dreisow, R. Keil, A. V. Korovin, U. Peschel, S. Nolte, and A. Tünnermann, “Tuning the structural properties of femtosecond-laser-induced nanogratings,” Appl. Phys., A Mater. Sci. Process. **100**(1), 1–6 (2010).

110. V. R. Bhardwaj, E. Simova, P. B.Corkum, D. M. Rayner, C. Hnatovsky, R. S. Taylor, B.Schreder, M.Kluge, J.Zimmer , “Femtosecond laser-induced refractive index modification in multicomponent glasses”, J of Appl. Phys. **97** (8),083102–083102-9 (2005).

111. Y. Shimotsuma, P. G. Kazansky, J. Qiu, K. Hirao, “Self-Organized Nanogratings in Glass Irradiated by Ultrashort Light Pulses”, Phys. Rev. Lett. **91**, 247405 (2003).

112. S. Juodkazis, K. Nishimura, S. Tanaka, H. Misawa, E. G. Gamaly, B. Luther-Davies, L. Hallo, P. Nicolai and V. T. Tikhonchuk, “Laser-Induced Microexplosion Confined in the Bulk of a Sapphire Crystal: Evidence of Multimegabar Pressures”, Phys. Rev. Lett. **96**, 166101 (2006).

113. L. Shah, J. Tawney, M. Richardson, K. Richardson, "Self-focusing during femtosecond micromachining of silicate glasses", IEEE J of Quant. Elect., **40** (1), 57–68 (2004).

114. B. P. Cumming, A. Jesacher, M. J. Booth, T. Wilson, and M. Gu, “Adaptive aberration compensation for three-dimensional micro-fabrication of photonic crystals in lithium niobate”, Opt. Express **19 (**10), 9419 (2011).

115. T. Tadamasa, F. Yoshio, W. Wataru, I. Kazuyoshi, N. Junji and H. Kenichi, “Estimation of the Refractive Index Change in Glass Induced by Femtosecond Laser Pulses”, Opt. Rev. **7** (1) , 14–17 (2000).

116. D. Wortmann, J. Gottmann, N. Brandt, H. Horn-Solle, “Micro- and nanostructures inside sapphire by fs-laser irradiation and selective etching”, Opt. Exp. **16** (3), 1517–1522 (2008).

117. P. G. Kazansky, J. Mills, E. Bricchi, J. J. Baumberg, J. Qui, K. Hirao, ”Self-organized form birefringence in glass irradiated by intense ultrashort light pulse”, CLEO/QELS 2003 Conference on Lasers and Electro-Optics / Quantum Electronics and Laser Science Conference, Baltimore, USA (2003).

118. Y. Shimotsuma, J. Qiu, P. G. Kazansky and K. Hirao “Nano-modification inside transparent materials by femtosecond laser single beam”. Modern Physics Letters B **19** (5), 225–238 (2005).

119. P. Yang, G. R. Burns, J. Guo, T. S. Luk, G. A. Vawter, “Femtosecond laser-pulse-induced birefringence in optically isotropic glass”, J. Appl. Phys. **95**, 5280 (2004).

120. C. Hnatovsky, R. S. Taylor, P. P. Rajeev, E. Simova, V. R. Bhardwaj, D. M. Rayner and P. B. Corkum, “Pulse duration dependence of femtosecond-laser-fabricated nanogratings in fused silica”, Appl. Phys. Lett. **87**, 014104 (2005).

121. S. Richter, M. Heinrich, S. Döring, A. Tünnermann, S. Nolte, “Formation of femtosecond laser-induced nanogratings at high repetition rates”, Appl. Phys. A. **104**, 503–507 (2011).

122. H. Kikuta, Y. Ohira, K. Iwata, “Achromatic quarter-wave plates using the dispersion of form birefringence”, Appl. Opt. **36** (7), 1566–1572 (1997).

123. Birefringent Materials. Available at: http://hyperphysics.phy-astr.gsu.edu/hbase/phyopt/biref.html [Accessed 2012.06.06].

124. S. K. Shevell, “The Science of Color”, Optical Society of America. Published 2003. ISBN 0-444-51251-9, 297 (2003).

125. M.Beresna, M.Gecevičius, P.G. Kazansky, “Polarization sensitive elements fabricated by femtosecond laser nanostructuring of glass”, Opt. Materials Express **1** (4), 783–795 (2011).

126. W.Cai, A. R. Libertun, R. Piestun, “Polarization selective computer-generated holograms realized in glass by femtosecond laser induced nanogratings”, Optics Express **14** (9), 3785–3791 (2006).

127. R. Taylor, C. Hnatovsky, E. Simova, “Applications of femtosecond laser induced self-organized planar nanocracks inside fused silica glass”, Laser & Photonics Rev. **2** (1-2), 26–46 (2008).

128. D. Wortmann, J. Gottmann, N. Brandt, and H. Horn-Solle, "Micro- and nanostructures inside sapphire byfs-laser irradiation and selective etching," Opt. Express **16**, 1517–1522 (2008).

129. R. Osellame, "Biophotonic chips fabricated by femtosecond laser micromachining," IEEE Photonics Society, 23rd Annual Meeting, 536–537 (2010).

130. A. Mermillod-Blondin, A. Rosenfeld, R. Stoian, E. Audouard, “Formation dynamics of femtosecond laser-induced phase objects in transparent materials”, Proc. of the SPIE **8247**, 82470Q–82470Q-7 (2012).

131. M. J. Ventura, M. Straub, and M. Gu,"Void channel microstructures in resin solids as an efficient way to infrared photonic crystals", Appl. Phys. Lett. **82**, 1649 (2003).

132. Center for Nanoscience and Technology Labs description. Available at: http://cnst.iit.it/ [Accessed 2012.06.10].

133. Aerotech engineering reference. Available at: www.aerotech.com [Accessed 2012.05.20].

134. K. Kim, K. Yoon, J. Suh, J. Lee, „Laser Scanner-Stage Synchronization Method for High-Speed And Wide-Area Fabrication", J. of Laser Micro/Nanoengineering **7** (2), 231–235 (2012).

135. T. Kildušis, T. Kazakevičius, „Laser micromachining software attains research-friendly status", J Laser Focus World, 29–36 (2012).

136. J. F. Nye, M. V. Berry. „Dislocations in wave trains", Proc .R. Soc. Lond. A.**336**, 165–190 (1974).

137. K . Toyoda, K . Miyamoto, N. Aoki, R . Morita, T.Omatsu , "Using optical vortex to control the chirality of twisted metal nanostructures", Nano Lett. 12 (7), 3645–9 (2012).

138. C.F. Phelan, R.J. Winfield, D.P. O'Dwyer, Y.P. Rakovich, J.F. Donegan, J.G. Lunney, "Two-photon polymerisation of novel shapes using a conically diffracted femtosecond laser beam", Opt. Comm. 284 (14), 3571–3574 (2011).

139. K . Toyoda, K . Miyamoto, N. Aoki, R . Morita, T.Omatsu , "Using optical vortex to control the chirality of twisted metal nanostructures", Nano Lett. 12 (7), 3645–9 (2012).

140. K. J. Moh, X.-C. Yuan, W. C. Cheong et al., "High-power efficient multiple optical vortices in a single beam generated by a kinoform–type spiral phase plate," Appl. Opt., 45 (6), 1153–1161 (2006).

141. I. G. Mariyenko, J. Strohaber, C. J. G. J.. Uiterwaal, "Creation of optical vortices in femtosecond pulses," Opt. Express **13**, 7599–7608 (2005).

142. K. Bezuhanov, A. Dreischuh, G. Paulus, M. G. Schätzel, H. Walther, D. Neshev, W. Królikowski, Y. Kivshar, "Spatial phase dislocations in femtosecond laser pulses," J. Opt. Soc. Am. B **23**, 26–35 (2006).

143. V. G. Shvedov, C. Hnatovsky, W. Krolikowski, A. V. Rode, “Efficient Beam Converter for the Generation of Femtosecond Vortices”, Opt. Lett. **35** (15), 2660–2662 (2010).

144. D. Ganic, X. Gan, M. Gu et al., “Generation of doughnut laser beams by use of a liquid-crystal cell with a conversion efficiency near 100%”, Opt. Lett. **27 (**15), 1351–1353 (2002).

145. Y. Izdebskaya, V. Shvedov, A. Volyar, “Generation of higher-order optical vortices by a dielectric wedge”, Opt. Lett. **30** (18), 2472–2474 (2005).

146. C. Tamm and C. O. Weiss, “Bistability and optical switching of spatial patterns in a laser,” Journal of the Optical Society of America B **7**, 1034–1038 (1990).

147. M. Beresna, M. Gecevičius, P.G. Kazansky, T.Gertus, “Radially polarized optical vortex converter created by femtosecond laser nanostructuring of glass”, Appl. Phys. Lett. **98**, 201101 (2011).

148. Z. Guo, S. Qu, S. Liu, “Generating optical vortex with computer-generated hologram fabricated inside glass by femtosecond laser pulses”, Opt. Comm. **273** (1), 286–289 (2007).

149. J. Strohaber, T.D. Scarborough, and C. J. Uiterwaal, “Ultrashort intense-field optical vortices produced with laser-etched mirrors”, APPL. OPT. **46** (36), 20 (2007).

150. D. Rozas, C. Law, and Jr. G. Swartzlander, "Propagation dynamics of optical vortices," JOSA B **14** (11), 3054–3065 (1997).

151. C. Hnatovsky, V. G. Shvedov, W. Krolikowski, and A. V. Rode, "Materials processing with a tightly focused femtosecond laser vortex pulse," Opt. Lett. **35**, 3417–3419 (2010).

152. R. M. White, F. W. Voltmer, “Direct piezoelectric coupling to surface elastic waves”, Appl. Phys. Lett., **7**, 314–316 (1965).

153. X. Liu, D. Du, and G. Mouru,”Laser ablation and micromachining with ultra-short laser pulses,” IEEE J of Quantum Electronics **33 (**10), 1706–1716 (1997).

154 . D. B. Wolfe, J. B. Ashcom, J. C. Hwang, C. B. Schaffer, E. Mazur and G. Whitesides, “Customization of poly(dimethyl siloxane) stamps by

micromachining using a femtosecond-pulsed laser," Adv. Mater. **15**, 62–65 (2003).

155. M. S. Giridhar, K. Seong, A. Shulzgen, P. Khulbe, N. Peyghambarian and M. Mansuripur, "Femtosecond pulsed laser micromachining of glass substrates with applications to microfluidic devices", Appl. Opt. **43**, 4584–4589 (2004).

156. F. Korte, J. Serbin, J. Koch, A. Egbert, C. Fallnich, A. Ostendorf, and B. N. Chichkov, "Mechanisms of decomposition of metal during femtosecond laser ablation", Appl. Phys. A: Mater. Sci. Process. **A 77**, 229 (2003).

157. D. Day, M. Gu, "Femtosecond fabricated photomasks for fabrication of micro fluidic devices", Optics Express **14** (22), 10753–10758 (2006).

158. C. K. Campbell, "Surface Acoustic Wave Devices for Mobile and Wireless Communications", Boston: Academic Press, ISBN-10: 0121573400, 620 (1998).

159. R. H. Olsson III and I. El-Kady, "Microfabricated phononic crystal devices and applications", Meas. Sci. Technol., **20**, 012002–1–13 (2009).

160. C. K. Campbell, "Surface Acoustic Wave Devices for Mobile and Wireless Communications", Academic Press, 620 (1998).

161. J. T. Devreese, "Photonic Crystals and Optical Lattices", Encyclopedia of Condensed Matter Physics **6**, 408–409 (2005).

162. S. Noda, M. Imada, M. Okano, S. Ogawa, M. Mochizuki, A. Chutinan, "Semiconductor three-dimensional and two-dimensional photonic crystals and devices," Quantum Electronics, IEEE **38** (7), 726–735 (2002).

163. E. Yablonovitch, "Photonic band-gap structures", JOSA B, **10** (2), 283–295 (1993).

164. L. Maigyte, T. Gertus, M. Peckus, J. Trull, C. Cojocaru, V. Sirutkaitis, K. Staliunas "Signatures of light beam spatial filtering in three-dimensional photonic crystal", Phys. Rev. A **82**, 043819 (2010).

165. W. J. Lai, K. S. Tiaw, B. C. Lim, H. H. Teo, M. H. Hong, P. B. Phua, "Radially polarized light generation using segmented spirally varying retarder," PhotonicsGlobal at Singapore, IPGC 2008, 1–3 (2008).

166. C. Mauclair, M. Zamfirescu, J. P. Colombier, G. Cheng, K. Mishchik, E. Audouard, R. Stoian, “Control of ultrafast laser-induced bulk nanogratings in fused silica via pulse time envelopes”, Opt. Express **20**, 12997–13005 (2012).

167. M. Stalder and M. Schadt, "Linearly polarized light with axial symmetry generated by liquid-crystal polarization converters," Opt. Lett. **21**, 948 (1996).

168. R. J. Pressley, “Handbook of Laser with Selected Data on Optical Technology”, Cleveland: Chemical Rubber Company (1971).

169. S. Quabis, R. Dorn, M. Eberler, O. Glockl, and G. Leuchs, “Focusing light to a tighter spot”, Opt. Commun. **179**, 1–7 (2000).

170. R. Dorn, S. Quabis, G. Leuchs, “Sharper focus for a radially polarized light beam,” Phys. Rev. Lett. **91**(23), 233901 (2003).

171. B. Hao, J. Leger, “Experimental measurement of longitudinal component in the vicinity of focused radially polarized beam,” Opt. Express **15**(6), 3550–3556 (2007).

172. D. P. Biss, T. G. Brown, “Polarization-vortex-driven second-harmonic generation,” Opt. Lett. **28**(11), 923–925 (2003).

173. S. Carrasco, B. E. A. Saleh, M. C. Teich, and J. T. Fourkas, “Second- and third-harmonic generation with vector Gaussian beams,” J. Opt. Soc. Am. B **23**(10), 2134–2141 (2006).

174. D. P. Biss, K. S. Youngworth, T. G. Brown, “Dark-field imaging with cylindrical-vector beams,” Appl. Opt. **45**(3), 470–479 (2006).

175. A. Hartschuh, “Tip-Enhanced Near-Field Optical Microscopy”, Angew. Chem. Int. Ed., **47**, 8178–8191 (2008).

176. Q. W. Zhan, “Evanescent Bessel beam generation via surface plasmon resonance excitation by a radially polarized beam,” Opt. Lett. **31**(11), 1726–1728 (2006).

177. Y. Liu, D. Cline, and P. He, “Vacuum laser acceleration using a radially polarized CO2 laser beam,” Nucl. Instrum. Methods Phys. Res. Sect. A **424**, 296–303 (1999).

178. Q. Zhan, "Cylindrical vector beams: from mathematical concepts to applications," Adv. Opt. Photon. **1**, 1–57 (2009).